

UC Berkeley

UC Berkeley Electronic Theses and Dissertations

Title

Characterization of Deuteron-Deuteron Neutron Generators

Permalink

<https://escholarship.org/uc/item/6z74x57b>

Author

Waltz, Cory Scott

Publication Date

2016

Peer reviewed|Thesis/dissertation

Characterization of Deuteron-Deuteron Neutron Generators

by

Cory Scott Waltz

A dissertation submitted in partial satisfaction of the

requirements for the degree of

Doctor of Philosophy

in

Engineering - Nuclear Engineering

in the

Graduate Division

of the

University of California, Berkeley

Committee in charge:

Professor Karl Van Bibber, Chair

Professor Lee Bernstein

Professor Peter Hosemann

Professor Chris Dames

Spring 2016

Characterization of Deuteron-Deuteron Neutron Generators

Copyright 2016
by
Cory Scott Waltz

Abstract

Characterization of Deuteron-Deuteron Neutron Generators

by

Cory Scott Waltz

Doctor of Philosophy in Engineering - Nuclear Engineering

University of California, Berkeley

Professor Karl Van Bibber, Chair

A facility based on a next-generation, high-flux D-D neutron generator (HFNG) was commissioned at the University of California Berkeley. The characterization of the HFNG is presented in the following study. The current generator design produces near mono-energetic 2.45 MeV neutrons at outputs of 10^8 n/s. Calculations provided show that future conditioning at higher currents and voltages will allow for a production rate over 10^{10} n/s.

Characteristics that effect the operational stability include the suppression of the target-emitted back streaming electrons, target sputtering and cooling, and ion beam optics. Suppression of secondary electrons resulting from the deuterium beam striking the target was achieved via the implementation of an electrostatic shroud with a voltage offset of greater than -400 V relative to the target. Ion beam optics analysis resulted in the creation of a defocussing extraction nozzle, allowing for cooler target temperatures and a more compact design. To calculate the target temperatures, a finite difference method (FDM) solver incorporating the additional heat removal effects of subcooled boiling was developed. Validation of the energy balance results from the finite difference method calculations showed the iterative solver converged to heat removal results within about 3% of the expected value. Testing of the extraction nozzle at 1.43 mA and 100 kV determined that overheating of the target did not occur as the measured neutron flux of the generator was near predicted values.

Many factors, including the target stopping power, deuterium atomic species, and target loading ratio, affect the flux distribution of the HFNG neutron generator. A detailed analysis to understand these factors effects is presented. Comparison of the calculated flux of the neutron generator using deuteron depth implantation data, neutron flux distribution data, and deuterium atomic species data matched the experimentally calculated flux determined from indium foil irradiations. An overview of experiments using the HFNG, including medical isotope cross section measurements, geochronology, delayed gamma measurements from uranium fission, and single event upset of cpu's is discussed. Future work should focus on the reduction of beam induced arcing between the shroud and the vacuum chamber. Investigation of insulator charge build-up, as well as electrical flash-over of insulators should

be explored. The reduction of beam induced arcing will allow for larger beam currents and acceleration voltages, therefore increasing the neutron flux.

To my grandparents, thank you for all your support and love

Contents

Contents	ii
List of Figures	iv
List of Tables	vii
1 Introduction	1
1.1 D-D and D-T Neutron Generators	1
1.2 Neutron Generator Applications	4
1.3 HFNG Design Overview	8
1.4 Facility	12
2 Electron Suppression	15
2.1 Secondary Electron Production	15
2.2 Magnetic Fields	15
2.3 Electrostatic Shroud	19
3 Target Analysis	22
3.1 Titanium Sputtering	22
3.2 Target Heat Analysis: Subcooled Boiling Overview	24
3.3 Finite Differences Method Including Subcooled Boiling Heat Transfer	26
3.4 HFNG Target Temperatures: Calculated Results	32
4 Deuterium Beam Analysis	35
4.1 Plasma Meniscus and Ion Beam Simulation Overview	35
4.2 Extraction Design and Ion Beam Optics Results	37
5 Neutron Flux and Distribution	42
5.1 Neutron Flux Analysis	42
5.2 CR-39 Measurements of Flux Distribution in Target Slot	48
5.3 Indium Foil Fast Flux Measurements	51

6	Overview of HFNG Experiments	58
6.1	Medical Isotope Cross Sections	58
6.2	Geochronology	60
6.3	Delayed Gammas from Uranium Fission	60
6.4	Single Event Upset of CPUs	61
7	Conclusions and Future Work	63
7.1	Conclusions	63
7.2	Future Work	64
	Bibliography	66
	Appendix A Finite Difference Equations	69
	Appendix B Temperature Maps	71
	Appendix C Neutron Flux and Energy Distribution Codes	74
	C.1 Matlab Flux Code	74
	C.2 MCNP Flux Code	83
	Appendix D CR39 and Predicted Neutron Flux Outputs	92
	Appendix E Indium Foil Experimental Data	94

List of Figures

1.1	Laboratory reference frame cross section for the DD and DT fusion reactions with a neutron in the exit channel	2
1.2	Neutron energy at different lab emission angles for 100 and 200 keV deuteron energies for (a) D-D and (b) D-T fusion reactions in the lab reference frame. . .	3
1.3	Angular distribution of neutrons for 50, 100, and 200 keV deuteron energies. for (a) D-D and (b) D-T fusion reactions in the lab reference frame.	4
1.4	HFNG design. (a) Components (b) Cross section exposing target, shroud, and ion sources. For scale, ion source is approximately 19 cm in diameter.	9
1.5	RF assembly: (a) impedance matching network, (b) ion source assembly with quartz window and external RF antenna, (c) CAD view exposing neodymium magnets	10
1.6	HFNG targets: (a) angled target with interior neodymium magnets, (b) flat target. Targets are approximately 9 cm wide by 9 cm tall and 2 cm thick. . . .	11
1.7	Electrostatic shroud: (a) assembled, (b) exploded view	12
1.8	(a) HFNG on sliding stand, (b) polyethylene shielding for production of thermal neutrons	13
1.9	Neutron beam port experimental cage	14
2.1	Neodymium magnet holders. (a) Photo of the magnet holders clamped to target cooling tubes. (b) CAD drawing, top view, showing neodymium magnets.	16
2.2	Simulations of (a) magnetic fields and (b) electric field	17
2.3	Comsol electron path simulation	18
2.4	Electric field simulation outside shroud with target potential at -100 kV and shroud potential at -102 kV	19
2.5	Electric field direction near shroud window at (a) 400 V, (b) 800 V, (c) and 1400 V voltage differential. Red indicates field along the direction of the deuteron beam (shown by arrow), blue indicates direction opposite the deuteron beam. T and S denote the target and shroud, respectively.	20
2.6	Cutaway view of secondary electron trajectories with shroud differential voltages of (a) 400 V and (b) 800 V at 100 kV target potential	21

3.1	Deuteron energy loss in titanium target due to ionization for (a) 67.5 deg. and (b) 0 deg. particle entrance. Energy loss to recoils with titanium target atoms for (c) 67.5 deg. and (d) 0 deg. particle entrance angles.	23
3.2	Boiling regimes corresponding to wall superheat (Ref. [20])	25
3.3	FDM nodal grid cross section. Nodes are at center of each square. (a) Cross section along center of target, blue shaded regions are water channels. (b) Nodal grid of water channels	27
3.4	Finite differences grid setup for various heat transfer modes and boundary conditions: (a) heat conduction, (b) adiabatic wall, (c) surface heat flux, (d) single phase convection, (e) subcooled boiling	29
3.5	Inputs and calculated water properties for the HFNG FDM temperature calculator	31
3.6	Surface temperatures along the target for uniform heat flux ion beams of (a) 5 mm and (b) 10 mm diameter	33
3.7	Ratio of maximum heat flux along a cooling channel wall to the critical heat flux	34
4.1	Plasma meniscus shape: (a) flat, (b) concave, and (c) convex plasma meniscus from Ref. [13]	35
4.2	Comsol simulation of electric field and deuteron beam trajectory at 100 kV and 1.43 mA	37
4.1	(a) Flat extraction geometry (b) electric potential shaping with an extraction nozzle (c) 10 mA at 125 kV threaded nozzle insert for the HFNG	38
4.2	Beam Power on target for (a) 1.43 mA, 100 kV flat plate extraction; (b) 1.43 mA, 100 kV nozzle defocussing extraction; (c) 10 mA, 125 kV flat plate extraction; (d) 10 mA, 125 kV nozzle defocussing extraction	40
4.3	Electric potential shaping with an extraction nozzle. Convex equipotential lines result in a diverging electric field.	41
5.1	Deuterated target stopping power for deuteron ions for target with D/Ti loading ratio of 1	43
5.2	Ion species in multi-cusp ion source (Ref. [30])	44
5.3	MCNP simulation of neutron flux along center-line of target slot as a distance of 8.38 mm away from target surface.	45
5.4	Total calculated flux for various atomic species fractions	47
5.5	Total calculated flux for various atomic species fractions	48
5.6	HFNG cross section showing CR-39 placement	49
5.7	100 kV, 1.33 mA predicted flux and maximum neutron energy maps in HFNG target slot	50
5.8	CR-39 detector counts vs. normalized predicted results	51
5.9	$^{115}\text{In}(n,n')^{115m}\text{In}$ experimental cross section values from ENDF database. Lower graph depicts the region between 2-3 MeV.	52
5.10	Foil locations compared to beam center. Flux map is Matlab predicted flux with 65% D+, 25% D ₂ ⁺ , and 10% D ₃ ⁺ atomic ratio	53

5.11	Comsol simulated current density at target for 1.43 mA, 100 kV deuterium beam	54
5.12	MCNP calculation of neutron energy spectrum in each foil. Lower graph depicts the 2.5-2.8 MeV region.	55
6.1	Gamma ray spectrum post irradiation of a titanium foil using the HFNG . . .	59
6.2	Delayed gamma spectrum from the fission of ^{238}U using the HFNG. Measured lifetimes of the 847 and 884 keV gamma decays were confirmed with that of ^{134}I .	61
6.3	Experimental setup of SEU testing of electronic components	62
B.0	Target temperature maps for uniform beam flux with beam diameters of (a and b) 5 mm, (c and d) 10 mm, (e) 15 mm, and (f) 20 mm.	72
B.1	Target surface temperatures for uniform beam heat flux for (a) 5 mm, (b) 10 mm, (c) 15 mm, and (d) 20 mm ion beam diameters.	73
D.1	Smoothed interpolated CR-39 detector count distribution	92
D.2	(a) 100 kV, 1.43 mA and (b) 125 kV, 10 mA predicted flux maps in HFNG target slot	93
D.3	Neutron energy spread in target sample slot for deuterium beams of (a) 100 keV, 1.43 mA and (b) 125 keV, 10 mA	93

List of Tables

1.1	Coefficients for Equation 1.5 [3]	3
1.2	Coefficients for Equation 1.6 [3]	4
1.3	Neutron capture reaction data relevant to argon isotope production from various target isotopes (Ref. [10])	7
3.1	SRIM analysis: 100 keV, 1.3 mA deuteron beam	22
3.2	Energy Balance Validation for 5 mm Beam Diameter	31
5.1	Differences in Matlab and MCNP codes	46
5.2	Percent Difference Compared to Experimental Results	51
5.3	Experimental vs. Calculated Flux	57
6.1	Proposed Medical Isotope (n,p) Cross Section Measurement Experiments	59
E.1	Indium Foil Properties	94
E.2	Indium Foil Location 1 Properties	95
E.3	Indium Foil Location 2 Properties	95
E.4	Indium Foil Location 3 Properties	96
E.5	Indium Foil Location 4 Properties	96
E.6	Indium Foil Location 5 Properties	97
E.7	Indium Foil Location 6 Properties	97
E.8	Indium Foil Location 7 Properties	98
E.9	Indium Foil Location 8 Properties	98
E.10	Indium Foil Location 9 Properties	99

Acknowledgments

I would like to thank Professor Karl Van Bibber for his mentorship throughout this difficult and exciting project, as well as the help received from the collaborators at the Berkeley Geochronology center, Tim Becker and Paul Renne. I would also like to thank Lee Bernstein for not only taking over the managerial aspects of the project, but for providing insight into the physics of the machine.

I would also like to thank all the people who put work into the initial design of the generator, including Ka-Ngo Leung, Allen Chen, and Glenn Jones. I would like to thank Peter Hoseman and Chris Dames for serving on my thesis committee. I would like to thank Jay James and Rick Firestone for their insights on the physics and engineering aspects of the device. I would also like to thank Darren Bluel and Joe Bauer for their MCNP skills that have been put to great use on the HFNG. I would like to thank Andrew Rogers, Leo Kirsch, Austin Lo, Joseph Labrum, Keeton Ross, Will Kable, Joseph Lee, Kevin Cherng, Meiji Nguyen, Yao Xu, and Nicole Rahal for their help working beside me in the lab. I would like to thank Mauricio Unzueta for taking over the project, I wish you luck! I would like to thank all of the collaborators that used the HFNG, including members of the Bay Area Neutron Group, Bethany Goldblum, Eric Mathews, Isaac Meyer, and Chad Ummel.

I would also like to thank all the roommates and close friends I have had over the years in Berkeley. David Weisshaar, Nick Adams, Kyler Lugo, Maria Simanovskaia, Joey Kabel, Nick Brickner, and Austin Lo, I couldn't have asked for better roommates and friends. Lastly, I would like to thank my parents, I couldn't have done any of this without you.

Chapter 1

Introduction

1.1 D-D and D-T Neutron Generators

The creation of neutrons are important for many applications across a broad range of industries including, among others, the medical field, oil well drilling, and geochronology. With an increased demand in neutron production applications, development of compact mono-energetic deuteron-deuteron (D-D) and deuteron-triton (D-T) neutron sources has progressed. Characterizing these neutron sources is important in improving functionality of the source. An in-depth analysis of the electron suppression techniques, target cooling and sputtering characteristics, and ion beam optics are necessary to fully understand not only how the machine behaves at steady state, but are also important in determining the characteristics of the neutron output, from the neutron energy spread to the total flux.

Small accelerator based D-D and D-T neutron generators take advantage of fusions reactions shown in equations 1.1 and 1.2 to produce nearly mono-energetic neutrons.



A competing reaction to reaction 1.1 includes a triton and a proton in the exit channel, shown below in reaction 1.3.



Reactions 1.1 and 1.3 have nearly equal probabilities of occurring at deuteron energies below 2 MeV. The Q-value of the D-D reaction is equal to 3.3 MeV, in which the neutron carries off around 2.45 MeV, while the Q-value for the D-T reaction is 17.6 MeV, with about 14 MeV carried away by the neutron.

In D-D and D-T neutron generators, positively charged deuteron ions are extracted from an ion source via an electric field created by a negative potential on a target or extraction electrode. The target can be deuterated, tritiated, or self-loading. In the latter case, a getter material, like titanium, is used on the surface of the target to absorb bombarding deuteron

ions from the extracted beam. The reaction rate can be determined by using the following equation from Ref. [1]

$$R = IN\sigma(E) \quad (1.4)$$

where I is the deuterium beam flux ($\#/cm^2/s$), N is the target atomic density ($\#/cm^3$), and $\sigma(E)$ is the nuclear cross section (cm^2). The differential cross section for the release of a neutron at 90° in the lab frame (deuteron bombarding a stationary target) is shown in Fig. 1.1 for both the D-D and D-T fusion reactions. A neutron release angle of 0° is incident to the deuteron beam direction (noted hereon as the forward direction), while 90° is perpendicular to the incident beam direction. The cross section data shown in Fig. 1.1

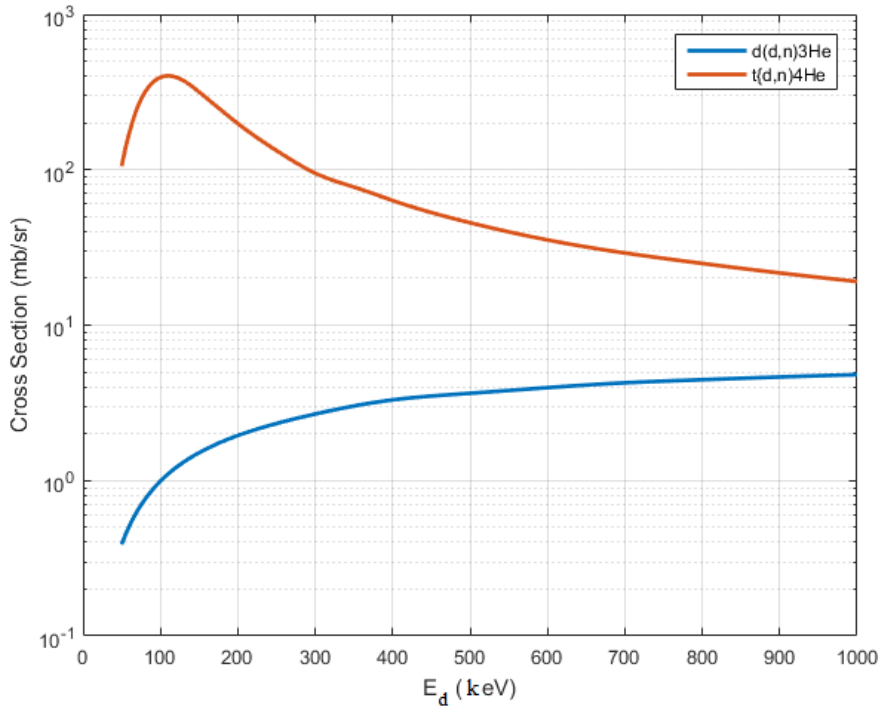


Figure 1.1: Laboratory reference frame cross section for the DD and DT fusion reactions with a neutron in the exit channel

comes from an extensive study by Liskien and Paulsen in reference [2]. It can be seen at deuteron energies below 200 keV, the D-T cross section is over 100 times larger than that of the D-D reaction.

As the deuteron energy increases in the lab reference frame, the neutron energy varies as a function of emission angle from the target. For a thick target, the neutron energy can be determined by the fit shown in equation 1.5 [3].

$$E_n = A_0 + \sum_{n=1}^n A_n \cos^n(\theta) \quad (1.5)$$

Table 1.1: Coefficients for Equation 1.5 [3]

Coefficient	DD	DD	DT	DT
	100 keV	200 keV	100 keV	200 keV
A0	2.46674	2.47685	14.06732	14.10711
A1	0.30083	0.39111	0.67488	0.95596
A2	0.01368	0.04098	0.01719	0.03320
A3	—	0.02957	—	—

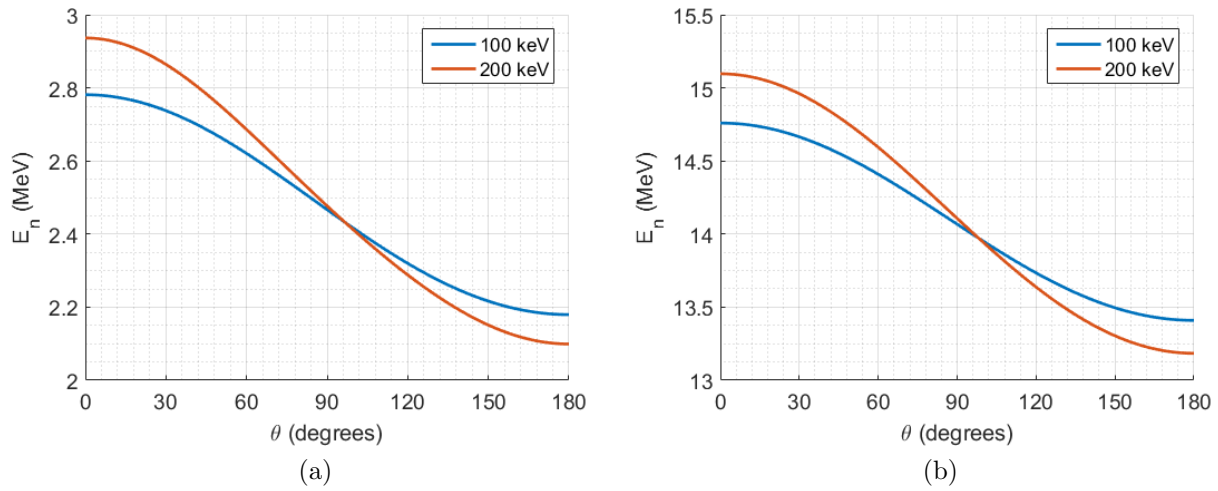


Figure 1.2: Neutron energy at different lab emission angles for 100 and 200 keV deuteron energies for (a) D-D and (b) D-T fusion reactions in the lab reference frame.

E_n is the neutron energy in MeV, and the coefficients for the equation can be seen in table 1.1. The peak energies of the released neutrons by emission angle for deuteron energies of 100 and 200 keV using equation 1.5 are shown in Fig. 1.2. It can be seen that for both D-D and D-T reactions, the neutron energy is largest in the forward direction. As the energy of the deuteron increases, the neutron energy spread between 0° and 180° increases. Data from reference [4] shows that for a thick target, at 100° , the neutron energy distribution is sharp and as the release angle deviates from 100° the neutron energy distribution at a given angle increasingly spreads.

The neutrons released from the D-D and D-T fusion reaction are anisotropic in the lab frame. A fit of the angular distribution to experimental data for a thin target is shown in equation 1.6 [3].

$$\frac{R(\theta)}{R(90)} = 1 + \sum_{n=1}^n A_n \cos^n(\theta) \quad (1.6)$$

Equation 1.6 is normalized to the neutron yield at 90° , with the coefficients shown in

Table 1.2: Coefficients for Equation 1.6 [3]

Coefficient	DD 50 keV	DD 100 keV	DD 200 keV	DT 50 keV	DT 100 keV	DT 200 keV
A0	1	1	1	1	1	1
A1	0.11787	0.01741	-0.03149	0.0344	0.0482	0.0678
A2	0.58355	0.88746	1.11225	0.0010	0.0011	0.0005
A3	-0.11353	0.22497	0.38659	—	—	—
A4	0.04222	0.08183	0.26676	—	—	—
A5	0.16359	0.37225	0.11518	—	—	—

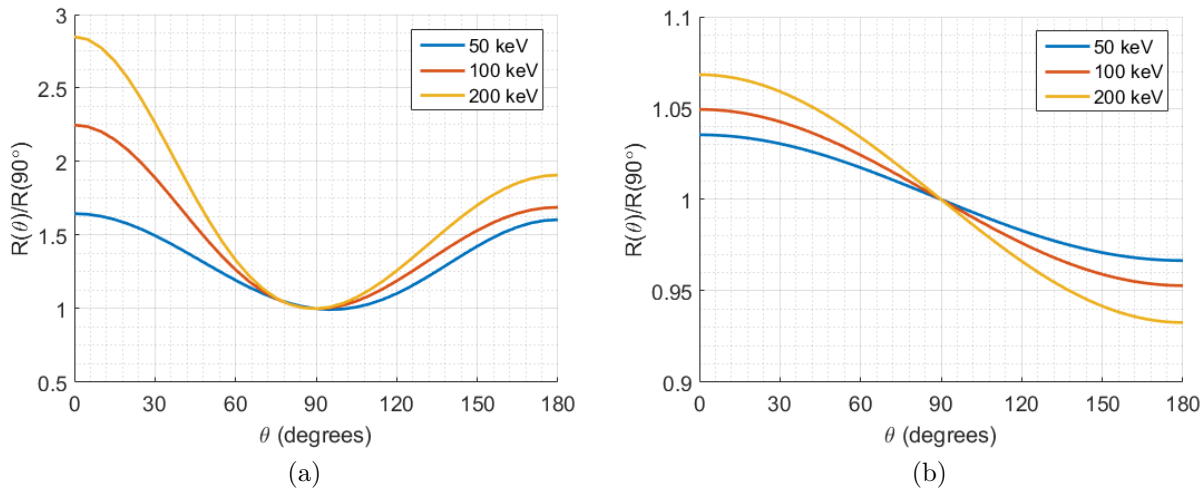


Figure 1.3: Angular distribution of neutrons for 50, 100, and 200 keV deuteron energies. for (a) D-D and (b) D-T fusion reactions in the lab reference frame.

table 1.2. The normalized angular distributions for 50, 100, and 200 keV using equation 1.5 are shown in Fig. 1.3. As the deuteron energy increases in the lab frame, the neutron distribution increasingly favors the 0° and 180° directions in the D-D reaction. For the D-T reaction, release in the forward direction increases as the deuteron energy increases, while release at 180° decreases. The normalized distribution of equation 1.6 can be multiplied by the differential cross section data at 90° shown in Fig. 1.1 to determine the differential cross sections at various release angles.

1.2 Neutron Generator Applications

Although the neutron flux of D-D and D-T neutron generators is lower than that of a research reactor, D-D and D-T generators have the advantages of posing less of a proliferation risk, being compact, less expensive, and have the capability of producing near

mono-energetic neutrons. Neutron generators can also be used in pulsed modes, and can be turned off instantly. Because of these benefits, D-D and D-T neutron generators have many applications. D-D and D-T generators can be used for nuclear data experiments, including measuring neutron reaction cross sections and analyzing neutron induced fission reactions. A brief overview of other applications will be given including: oil well logging, medical isotope production, and geochronology.

Oil Well Logging

Well logging is the practice of measuring the geologic properties surrounding a drilled well. A basic overview of well logging is explained in reference [5]. The goal is to determine where there are regions of high hydrocarbon content in which oil can be extracted.

One common method to determine this is through the use of a D-T neutron generator along with a gamma ray detector installed near the drilling tip, as described in reference [6]. The neutrons emitted from the neutron generator are absorbed in the surrounding materials, which in turn emit gamma rays of characteristic energies. This allows one to determine the elemental composition of the surroundings by looking at the energy of the gamma rays from the detector response.

The method described previously can determine the elemental composition surrounding the neutron source, however many compositions contain the same elements, for example oil and water both contain large amounts of hydrogen. In the 1960's, a new technique of determining the composition of the surrounding geological materials in an oil well was developed, as described in reference [7]. The technique contains a similar setup as previous described, and involves the use of a pulsed D-T neutron generator along side a scintillator detector to measure the average neutron lifetime. Material compositions with high neutron absorption cross sections result in a lower neutron lifetime compared to compositions containing materials with low neutron absorption cross section. Common neutron lifetimes in rock salt is about $5 \mu\text{s}$, compared to approximately $900 \mu\text{s}$ in quartzite. Chlorine has a rather high cross section for neutron absorption compared to the constituents of oil (carbon and hydrogen). Since chlorine is usually found in high concentrations within water, measuring the neutron lifetime allows one to distinguish water from oil. The method involves pulsing the neutron generator, allowing for intervals where no neutrons are emitted. During this time it takes around $10\text{-}50 \mu\text{s}$ for the neutrons to thermalize, at which they become more likely to be absorbed by surrounding materials. During this time most of the neutrons are still within a few inches from the source. The detector is then gated to record data at certain time intervals, recording the rate of gammas detected from neutron absorption at times near and distant from the pulse. allowing for the comparison of the neutron lifetimes.

Detailed designs for neutron generators used in oil well logging are rarely available to the public, as many private companies create these neutron generators and their techniques are proprietary. The neutron generators usually consist of a high voltage power supply, insulators, ion source, and target all within the drilling assembly. These generators must be able to withstand high temperatures as well as large amounts of vibration.

Medical Isotope Production

Radioisotopes are used in medicine to treat tumors and for imaging of organs such as the thyroid or heart. ^{99m}Tc , a metastable isotope of technetium, is used in approximately 80% of all medical imaging procedures worldwide [8]. In 2007, a ^{99m}Tc production facility in Canada shut down, resulting in a reduction of isotope stock by 80% in the United States. This caused over 50,000 medical procedures to be canceled in a time span of 5 weeks [8].

^{99m}Tc is produced by the gamma decay of Molybdenum-99 (^{99}Mo). ^{99}Mo can be produced from fission of uranium-235 (^{235}U). As fission reactors create unwanted waste, research into using D-T neutron generators to create ^{99m}Tc has been proposed by Pagdon et al. in reference [9]. DT neutron generators can be used in two ways to produce ^{99}Mo : by neutron capture on ^{98}Mo , or by interaction of ^{100}Mo with high energy gamma rays. In the second method, high energy gamma rays can be produced by irradiating ^{16}O , which can be found in water, with neutrons. Although the specific activity of ^{99}Mo created using a DT generator is lower than that of fission due to lower reaction cross sections, using a D-T generator benefits from not producing the unwanted waste from ^{235}U fission. Future increases in neutron fluxes of D-T generators could provide a favored way of producing ^{99m}Tc .

Neutron induced reaction cross sections for the production of many medical isotopes, especially for (n,p) reactions, are either unknown or have little data. The use of D-D and D-T neutron generators can be used to experimentally determine the cross sections of these reactions at discrete energies. Initial experimental measurement of the (n,p) reaction cross section on zinc-64 and zinc-67 to create copper-64 and copper-67, two isotopes used in radiotherapy, has been achieved at the HFNG facility. These results will be described in further detail in chapter 6.

Geochronology: $^{40}\text{Ar}/^{39}\text{Ar}$ dating

$^{40}\text{Ar}/^{39}\text{Ar}$ dating is a geochronology technique capable of measuring geologic time to billions of years ago. The method, described in reference [10], is based on the decay of ^{40}K to ^{40}Ar by electron capture. The ability of the dating technique to date samples billions of years old is due to the long half life of the ^{40}K electron capture, which is about 1.27 billion years [11]. Through neutron irradiation, ^{39}Ar is produced from ^{39}K through an (n,p) reaction. As long as the a sample is irradiated with another sample of known age, the ratio of $^{40}\text{Ar}/^{39}\text{Ar}$ can be used to determine the age of the unknown sample. An issue with the $^{40}\text{Ar}/^{39}\text{K}$ method is that being chemically dissimilar two different techniques are needed to measure the $^{40}\text{Ar}/^{39}\text{K}$ ratio, introducing large systematic errors.

Neutron irradiating of $^{40}\text{Ar}/^{39}\text{Ar}$ dating normally is done in a ^{235}U reactor due to the large fluxes. It has been determined that the neutron energy spectrum of a ^{235}U nuclear reactor creates undesirable reactions in a sample. A summary of the interfering reactions taken from Ref. [10] can be seen in Tab. 1.3. At high neutron energies (greater than 3 MeV), many reactions in K, Ca, and Cl necessitate corrections to the dating calculation. The recoil caused by reactions from high energy neutrons from reactors can eject ^{39}Ar from

a sample. At thermal neutron energies, the $^{40}\text{K}(\text{n,p})^{40}\text{Ar}$ reaction has a large cross section. This reaction causes samples to appear older.

Reaction	Reaction Q -value (MeV)	Reaction threshold (MeV)	Average cross section	Average $(1/E)$ -weighted cross section	2.45-MeV cross section
$^{40}\text{K}(\text{n,n}\alpha)^{36}\text{Cl}$	-10.5969 (3)	10.8861 (3)	9.01×10^{-2}	6.71×10^{-2}	
$^{39}\text{K}(\text{n},\alpha)^{36}\text{Cl}$	1.3615 (3)	0.0	2.12×10^{-1}	2.11×10^{-2}	1.53×10^{-2}
$^{35}\text{Cl}(\text{n},\gamma)^{36}\text{Cl}$	8.57970 (7)	0.0	5.88×10^{-4}	$1.56 \times 10^{+2}$	9.32×10^{-4}
$^{40}\text{Ca}(\text{n,n}\alpha)^{36}\text{Ar}$	-6.9912 (5)	7.1821 (5)	3.89×10^{-2}	2.86×10^{-2}	
$^{36}\text{Ar}(\text{n},\gamma)^{37}\text{Ar}$	8.7889 (4)	0.0	1.27×10^{-3}	$1.94 \times 10^{+1}$	2.43×10^{-3}
$^{40}\text{Ca}(\text{n},\alpha)^{37}\text{Ar}$	1.7483 (5)	0.0	1.25×10^{-1}	1.18×10^{-2}	5.57×10^{-2}
$^{37}\text{Cl}(\text{n},\gamma)^{38}\text{Cl}$	6.10778 (10)	0.0	3.87×10^{-4}	1.54×10^0	5.76×10^{-4}
$^{41}\text{K}(\text{n},\alpha)^{38}\text{Cl}$	-0.1145 (3)	0.1176 (3)	1.87×10^{-2}	5.97×10^{-3}	1.65×10^{-5}
$^{40}\text{Ar}(\text{n,t})^{38}\text{Cl}$	-12.12039 (11)	12.45117 (12)	1.23×10^{-4}	1.06×10^{-4}	
$^{39}\text{K}(\text{n,d})^{38}\text{Ar}$	-4.1565 (5)	4.2699 (5)	1.60×10^{-1}	1.47×10^{-1}	
$^{42}\text{Ca}(\text{n,n}\alpha)^{38}\text{Ar}$	-10.3668 (4)	10.6352 (4)	1.43×10^{-1}	1.11×10^{-1}	
$^{40}\text{Ar}(\text{n,d})^{39}\text{Cl}$	-10.3036 (18)	10.5774 (18)	1.44×10^{-3}	1.29×10^{-3}	
$^{38}\text{Ar}(\text{n},\gamma)^{39}\text{Ar}$	6.598 (5)	0.0	4.61×10^{-4}	3.15×10^0	7.93×10^{-4}
$^{42}\text{Ca}(\text{n},\alpha)^{39}\text{Ar}$	0.341 (5)	0.0	3.07×10^{-2}	2.17×10^{-3}	2.32×10^{-4}
$^{43}\text{Ca}(\text{n,n}\alpha)^{39}\text{Ar}$	-12.2011 (8)	12.5091 (8)	5.28×10^{-2}	3.96×10^{-2}	
$^{40}\text{K}(\text{n,d})^{39}\text{Ar}$	-5.358 (5)	5.500 (6)	1.08×10^{-1}	1.01×10^{-1}	
$^{39}\text{K}(\text{n,p})^{39}\text{Ar}$	0.217 (5)	0.0	3.21×10^{-1}	2.68×10^{-2}	1.80×10^{-1}
$^{44}\text{Ca}(\text{n,n}\alpha)^{40}\text{Ar}$	-13.91 (4)	14.25 (4)	7.70×10^{-3}	5.86×10^{-3}	
$^{40}\text{K}(\text{n,p})^{40}\text{Ar}$	2.2872 (3)	0.0	7.99×10^{-2}	$2.31 \times 10^{+1}$	3.80×10^{-2}
$^{41}\text{K}(\text{n,np})^{40}\text{Ar}$	-5.5834 (3)	5.7280 (3)	3.87×10^{-2}	3.68×10^{-2}	
$^{43}\text{Ca}(\text{n},\alpha)^{40}\text{Ar}$	2.2779 (5)	0.0	2.18×10^{-2}	2.05×10^{-3}	1.59×10^{-2}

Relevant reactor-induced reactions resulting in production of argon isotopes. The cross-section data were taken from the JENDL-3 and JEF-2 300 K libraries; they were retrieved using the Evaluated Nuclear Data Files on-line database. The Q -values were calculated with the program QCALC produced by the National Nuclear Data Center of the Brookhaven National Laboratory; the uncertainty in the last figure is shown in parentheses. The average cross sections and the average $(1/E)$ -weighted cross sections are specific to a ^{235}U fission spectrum; the latter (average $(1/E)$ -weighted cross section) is most relevant for a first-order comparison of the relative production probabilities.

Table 1.3: Neutron capture reaction data relevant to argon isotope production from various target isotopes (Ref. [10])

A proposed replacement for ^{235}U nuclear reactors are D-D neutron generators. The near mono-energetic 2.45 MeV neutrons produced are at a lower energy than many of the K, Ca, and Cl reactions that necessitate corrections. The ratio of fast-to-thermal neutrons in a typical D-D neutron generator is large, and surrounding a sample in cadmium can further reduce the flux of thermal neutrons. Previously, most neutron generators produce fluxes of less than 10^8 n/s, which is about 4 orders of magnitude lower than that of a typical ^{235}U reactor. Recent advancements in the analysis and design of D-D generators, as to be described in this work, show fluxes over 10^{10} n/s are achievable, making D-D neutron generators an attractive choice for dating of samples using the $^{40}\text{Ar}/^{39}\text{Ar}$ method.

1.3 HFNG Design Overview

The following overview describes each component of the HFNG that can be seen in Figure 1.4a, with further detailed analysis of the shroud, target, and deuteron beam optics covered in chapters 2, 3, and 4 respectively.

The HFNG is designed around two radio frequency-driven multi-cusp ion sources that straddle a titanium-coated copper target, as shown in Fig. 1.4b. Positively charged deuteron ions are accelerated up to 125 keV from the ion sources and self-load into the target. Upon target saturation, neutron generation occurs through the $d(d,n)^3\text{He}$ fusion reaction. The neutron energy and spacial distribution follows that of equations 1.5 and 1.6. The highest flux is that in the forward direction to the beam. To take advantage of this, a sample holder slot is located in the center of the target, at a distance of 6 mm from the locations where the deuterium strikes the target and generates neutrons.

Vacuum chamber and Turbomolecular Pump

An Adixen turbo-molecular pump was selected for use in the HFNG vacuum system. During testing, ultimate pressures of $2 \cdot 10^{-6}$ torr have been reached in the vacuum chamber while the ion sources are off. With the ion sources operational, source pressures are varied between 5.5-10 mtorr, resulting in main chamber pressures near $5 \cdot 10^{-6}$ torr. A residual gas analyzer is also used in the vacuum system to assure that water vapor has been thoroughly pumped out of the vacuum chamber prior to operation.

Most of the vacuum chamber is made of 6061 alloy aluminum. Aluminum was chosen since it does not create any lasting radioactivity from neutron irradiations, and is an electrical conductor, allowing the chamber to be electrically grounded. High density polyethylene (HDPE) was used to insulate the high voltage and target connection feedthroughs from the grounded vacuum chamber.

RF Generators, Matching Networks, and Ion Source

To provide RF power to each ion source, two 13.56 MHz RF power generators capable of producing up to 2000 W were used. In order to maximize the energy transfer between the RF generator and the load (plasma), the impedance of the supply should match that of the load. The impedance of the RF transfer line can be determined by

$$Z = \sqrt{\frac{L}{C}} \quad (1.7)$$

where Z is the characteristic impedance, L is the inductance, and C is the capacitance. It can be seen that varying the capacitance within the RF circuit allows for impedance matching. Impedance matching networks for each source were custom made, shown in Fig. 1.5a, each consisting of an inductor and a variable capacitor.

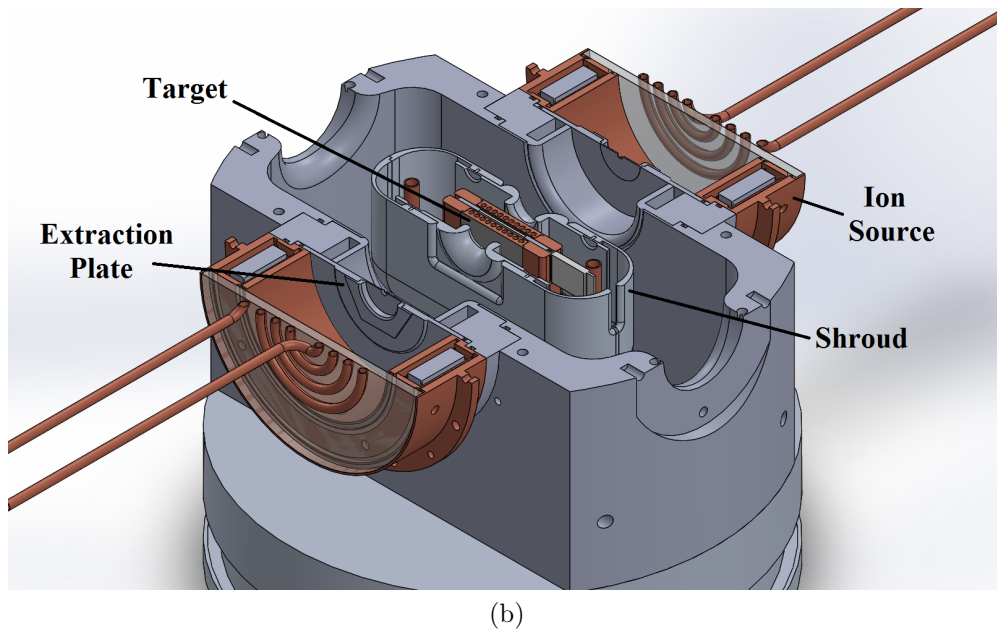
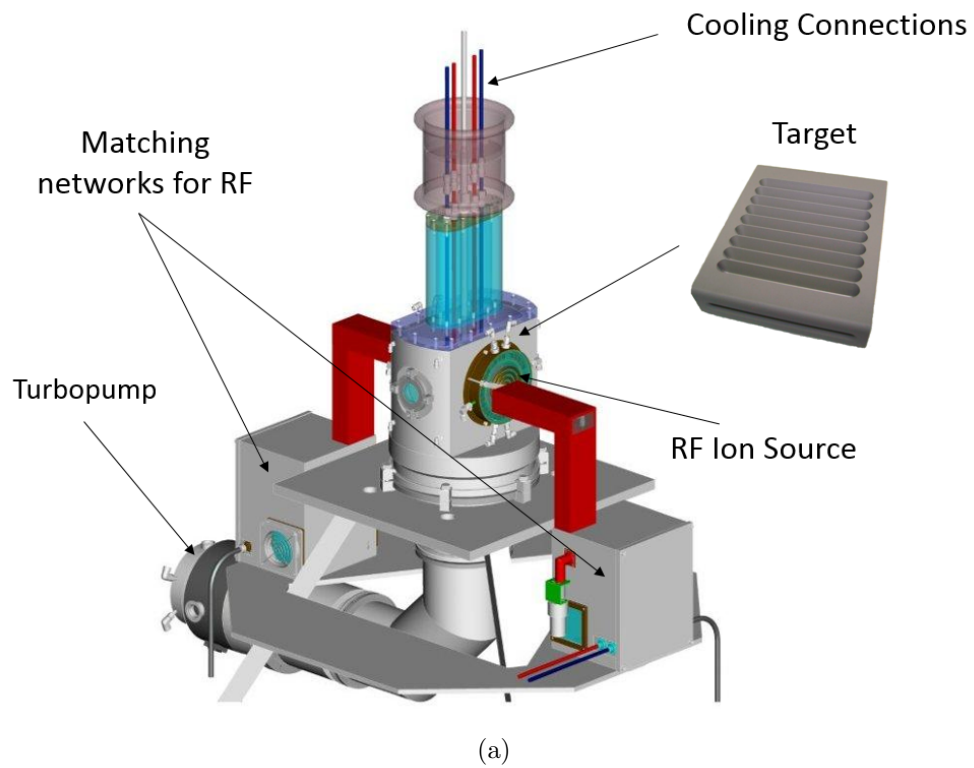


Figure 1.4: HFNG design. (a) Components (b) Cross section exposing target, shroud, and ion sources. For scale, ion source is approximately 19 cm in diameter.

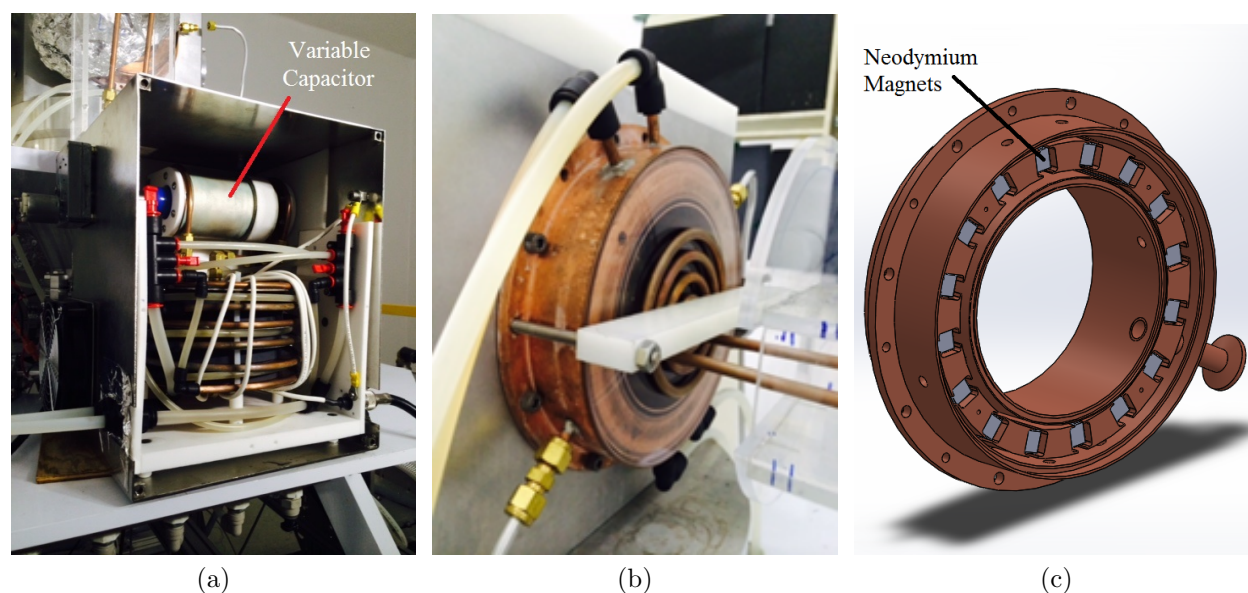


Figure 1.5: RF assembly: (a) impedance matching network, (b) ion source assembly with quartz window and external RF antenna, (c) CAD view exposing neodymium magnets

The multi-cusp radio-frequency (RF) ion source implemented on the HFNG is shown in Fig. 1.5b. The ion source is based on a similar LBNL design shown in Ref. [12]. An external RF antenna flush with a quartz window is used to transmit the RF power to the plasma. An impedance matching network, consisting of an inductor and a variable capacitor allows adjustment of the RF impedance to match that of the deuterium in the chamber to obtain maximum energy transfer. A hexadecapole magnetic field is formed by neodymium magnets in a circular array near the ion source walls, as can be seen in Fig. 1.5c. The magnetic field confines the mobile electrons, increasing the path length of an electron before it can reach a wall. This increase in confinement results in a larger electron density for a given source current, which allows for operation at lower pressures. More information on multicusp ion sources can be found in Ref. [13].

Self-Loading Targets

Two different target designs have been created for the HFNG, both are shown in Fig. 1.6. Both targets include a sample holder slot inside the target volume, allowing the samples to receive the highest neutron flux possible from the generator. The angled target design was focused on maximizing the heat removal, while the flat design focused on creating a more uniform neutron flux within the target slot.

Both targets are made of oxygen free high purity copper for its great thermal and electrical conductivity. The targets contain a layer of titanium on the surface for getting of deuterium. The angled target contains a 20 micron layer of titanium sputter coated on the surface, while

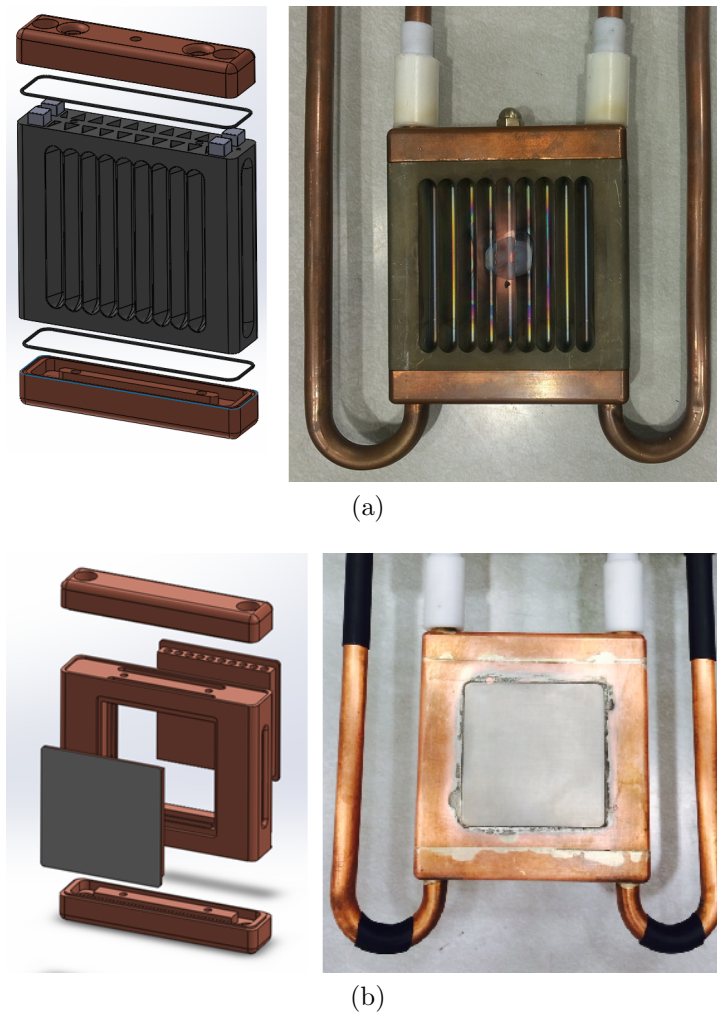


Figure 1.6: HFNG targets: (a) angled target with interior neodymium magnets, (b) flat target. Targets are approximately 9 cm wide by 9 cm tall and 2 cm thick.

the flat target has a 125 micron explosion bonded layer. The flat target contains replaceable inserts that are soldered to the target for easy replacement. Further analysis of the target is displayed in Chapter 3, including heat transfer and ion sputtering.

Electrostatic Shroud

A shroud is a device used to suppress back-streaming electrons created by the ionization of the target surface due to the bombarding deuterium beam. The shroud surrounds the target, and is placed at a larger negative potential than that of the target. When an electron is liberated from the target due to deuteron implantation, it will return to the target due to the electric field produced between the shroud and target. More electromagnetic analysis

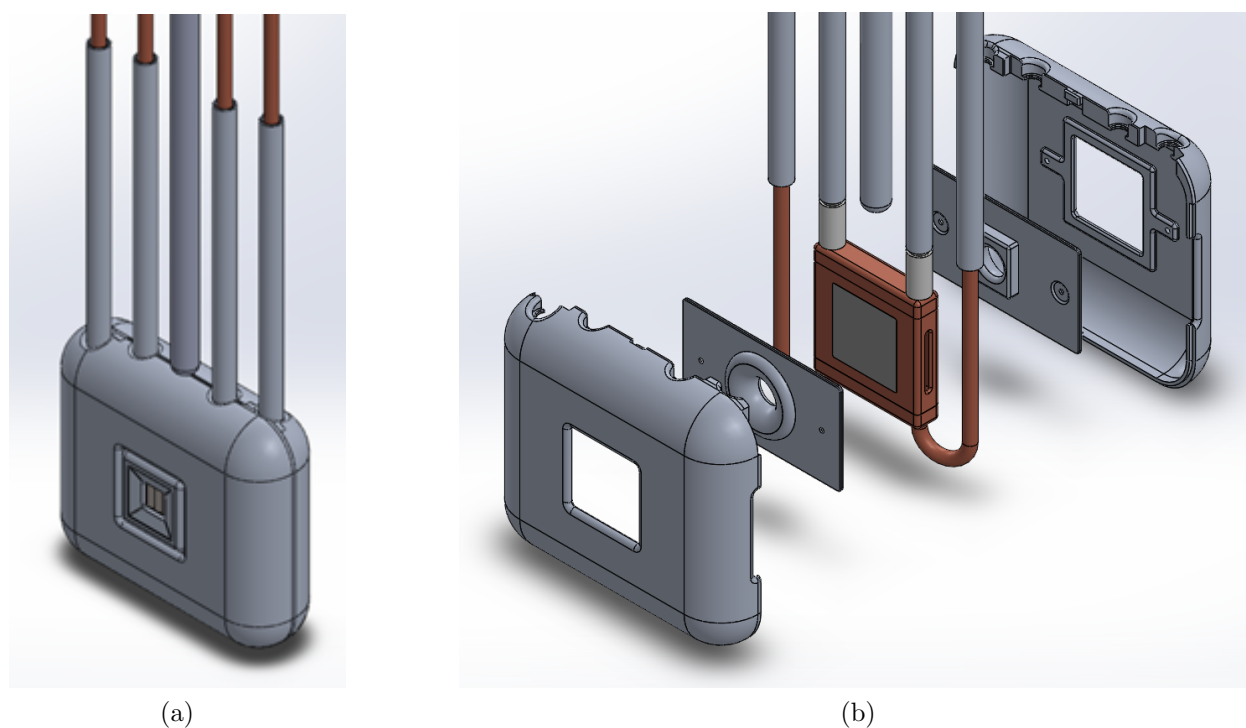


Figure 1.7: Electrostatic shroud: (a) assembled, (b) exploded view

and details of the shroud are discussed in chapter 2.

The shroud design used for the HFNG is shown in Fig. 1.7. The clamshell design allows for easy removal. Exchangeable face-plates allow for the ability to easily change the beam entrance window geometry. The voltage difference between the shroud and target is created through the use of multiple zener diodes in series. The total breakdown voltage of the zener diode chain is up to 2400 V.

1.4 Facility

The HFNG resides inside a high density concrete vault with walls at a minimum of 5 feet thick to provide shielding from neutron and gamma radiation. The facility offers multiple experimental setups for neutron irradiation. The highest flux sample location is in the target, as previously noted. A polyethylene shield, shown in Fig. 1.8b, can be used to increase the thermal neutron flux. The generator sits on a sliding stand, as shown in Fig. 1.8a, which allows it to be placed in front of a collimated port in the cement wall. An experimental cage with a boronated polyethylene beam dump is located outside the hole, shown in Fig. 1.9. Samples can be irradiated at the end of the collimated beam port, and prompt gamma rays can be detected without interference of background radiation produced by the HFNG.

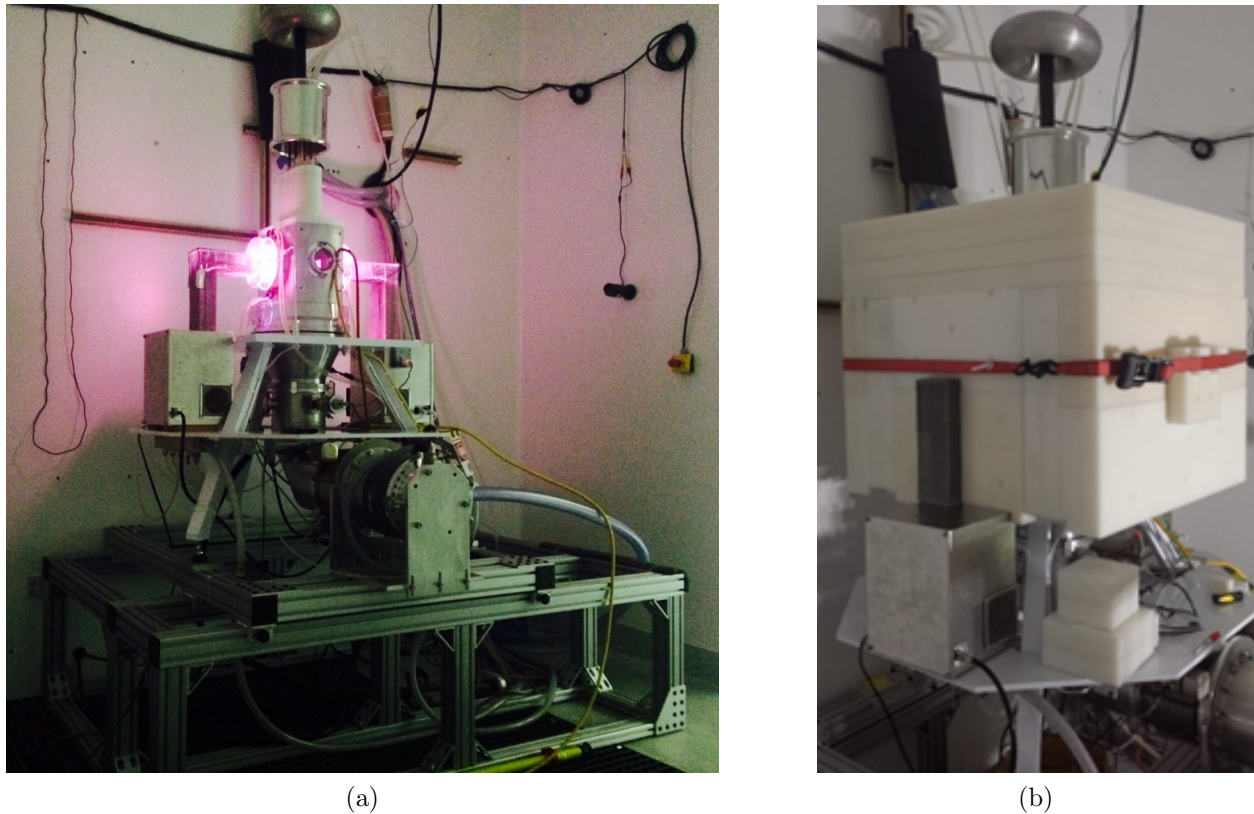


Figure 1.8: (a) HFNG on sliding stand, (b) polyethylene shielding for production of thermal neutrons

A cooling system was designed to provide up to 100 kW of cooling with deionized water. A separate cooling loop provides up to 10 kW of cooling for the RF power supplies, turbomolecular pump, and various auxiliary equipment. Multiple high voltage power supplies are installed capable of producing up to 120 mA of current at -125 kV. Water temperatures, flow, and pressures in the system are monitored.

A safety interlock system provides monitoring of the water and electrical equipment, a loss of water pressure or flow results in the automatic shutdown of the high voltage power supply. Water sensing tape is mounted on floors as a secondary backup to assure water does not leak onto electrical equipment. A radiation use authorization process allows for users to receive proper training in radiation safety before working with radioactive materials at the HFNG facility. The amount of radioactive materials created by the HFNG, whether from a sample irradiation or from components of the machine itself, is also documented. Efforts to mitigate unnecessary activation, such as removing unnecessary materials from the experimental vault or using low activation materials when possible, are practiced as well.

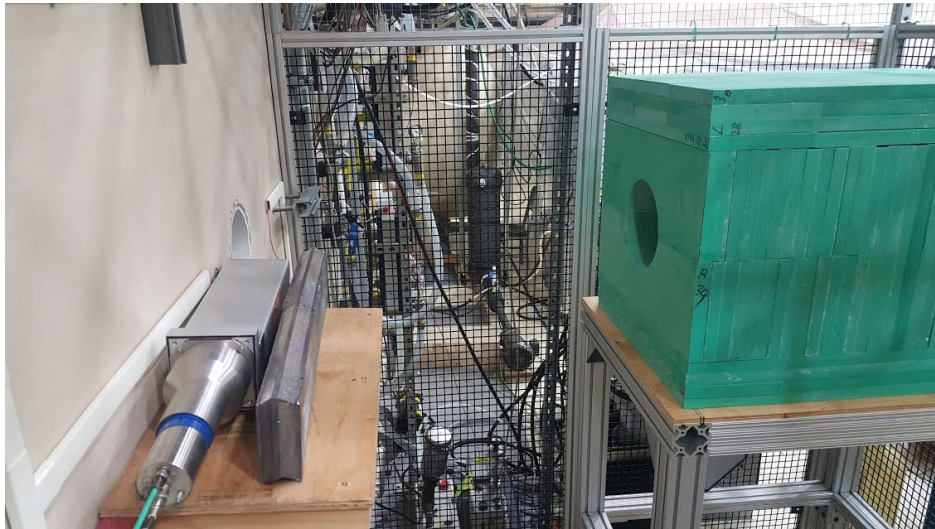


Figure 1.9: Neutron beam port experimental cage

Chapter 2

Electron Suppression

2.1 Secondary Electron Production

As deuterium ions extracted from the ion source strike the target, ionization occurs at the surface, releasing secondary electrons. According to a study done in Ref. [14], approximately 1.2 electrons are emitted per hydrogen atom for a deuteron striking a titanium target at 100 keV. Secondary electrons emitted from metal surfaces have energies around 10 eV, and typically not more than 30 eV (see Ref. [15]). Secondary electrons accelerate away from the target due to the negative electric potential, resulting in an electron beam that strikes the extraction plate. The collision of the secondary electron beam, especially with a high Z material such as the extraction plate, results in the emission of bremsstrahlung x-rays, and if the current density is large enough the melting can occur. Collision of electrons with any insulators inside the vacuum chamber will result in charge build-up, which over time will discharge in the form of an arc. If arcing is frequent, damage to the high voltage power supply can occur. Lastly, the secondary electrons are a leakage current to the high voltage power supply, making it difficult to accurately determine the contribution of current from deuterons compared to secondary electrons. Suppression of these electrons is vital for continuous operation of a neutron generator. Two methods of suppressing electrons were tested on the HFNG: using magnetic fields produced by permanent magnets and using an electric field created by installing an electrostatic shroud.

2.2 Magnetic Fields

One method of electron suppression involves the use of magnetic fields. Fig. 2.1 shows the implementation of large neodymium magnets on the HFNG target. The magnets are aligned with opposite poles facing each other, creating magnetic field lines parallel with the target surface. This causes ejected electrons to spiral around the field lines and back toward the target surface. It should be remembered that the electron does not only feel the force due to the magnetic field, but it also feels the force of the electric field used to accelerate the

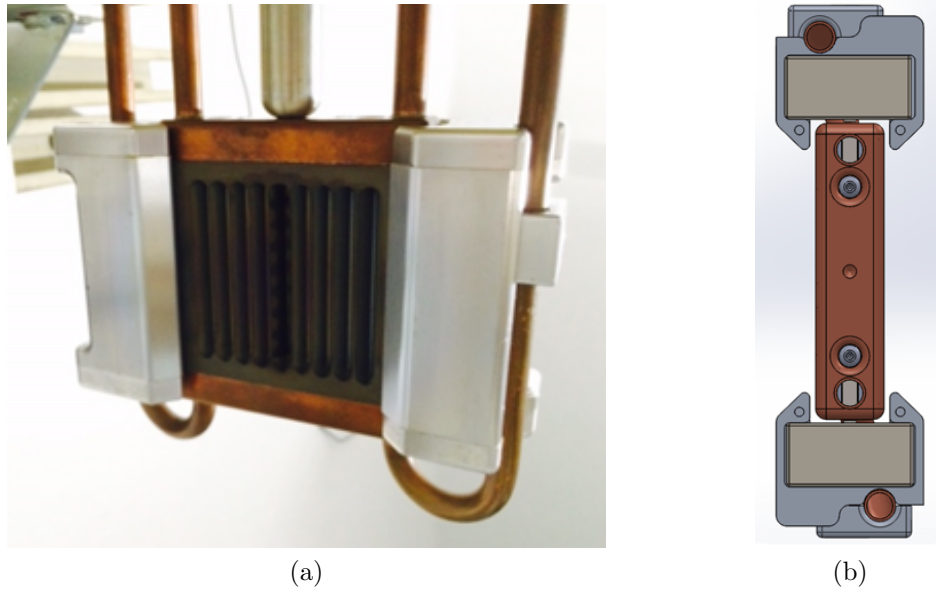


Figure 2.1: Neodymium magnet holders. (a) Photo of the magnet holders clamped to target cooling tubes. (b) CAD drawing, top view, showing neodymium magnets.

deuteron ions. This net force results in an $E \times B$ drift, which causes an orthogonal drift of the electron with respect to the magnetic and electric fields.

Cosmol Multiphysics was used to determine the electrical and magnetic fields within the HFNG vacuum chamber (see Ref. [16]). Cosmol uses the following macroscopic Maxwell's equations to determine the magnetic and electric fields:

$$\nabla \cdot D = \rho \quad (2.1)$$

$$\nabla \cdot B = 0 \quad (2.2)$$

$$\nabla \times E = -\partial_t B \quad (2.3)$$

$$\nabla \times H = J + \partial_t D \quad (2.4)$$

where

D = electric displacement field (C/m^2)

ρ = electric charge density (C/m^3)

E = electric field (V/m)

B = magnetic field (T)

H = magnetizing field (A/m)

J = current (A)

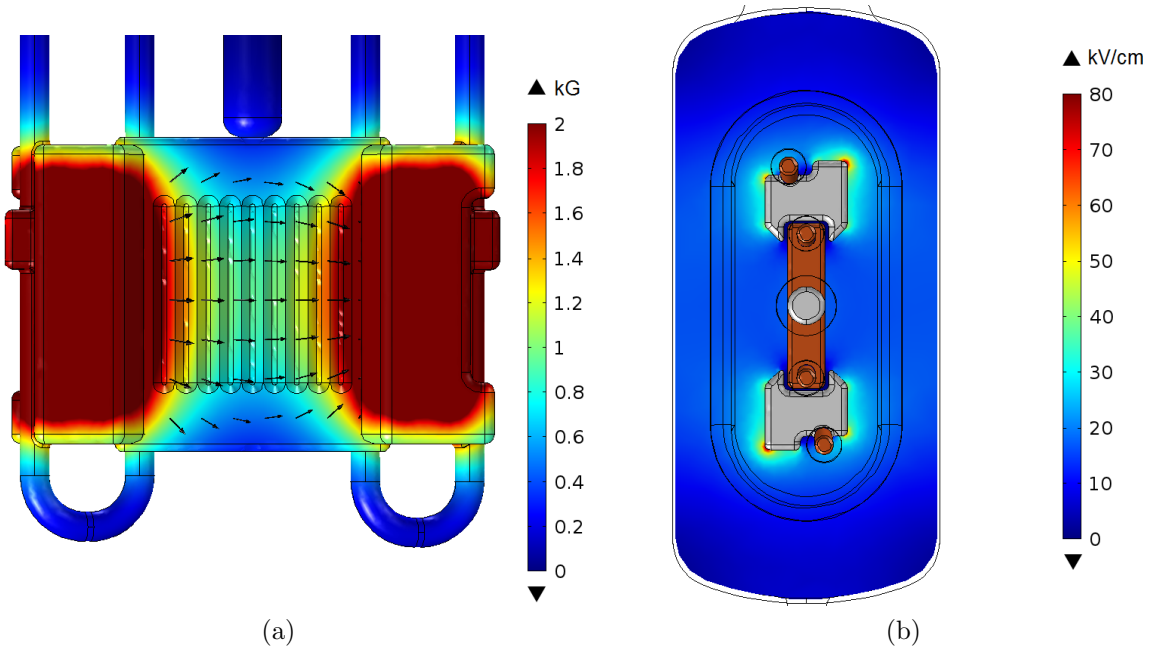


Figure 2.2: Simulations of (a) magnetic fields and (b) electric field

Equations 2.1 - 2.4 are in MKS units. Electric and magnetic fields can be derived from Faraday's law and Gauss' Law, respectively, and are as follows:

$$E = -\nabla V - \frac{\partial \vec{A}}{\partial t} \quad (2.5)$$

$$B = -\nabla \times \vec{A} \quad (2.6)$$

where V is the electric scalar potential and A is the magnetic vector potential. The fields are computed by using a finite element analysis over a meshed geometry. User entered boundary conditions include the electric potentials at the surface of a material, which materials have zero charge (insulators), and the remnant flux density (B_r) of magnets. For insulators, the zero charge boundary condition becomes:

$$n \cdot D = 0 \quad (2.7)$$

where $n \cdot D$ is the electric displacement field normal to the surface. This creates perpendicular equipotential lines and parallel electric field lines relative to the insulating surface. Charged particle trajectories can then be computed by Comsol by applying the forces on the particles due to the calculated magnetic and electric fields.

A Comsol simulation shows the strength of the magnetic field across the surface of the target in Fig. 2.2a. The neodymium magnets were grade N50, giving them a B_r between 14.1-14.5 kG. The black arrows represent the direction of the magnetic field lines in the respective

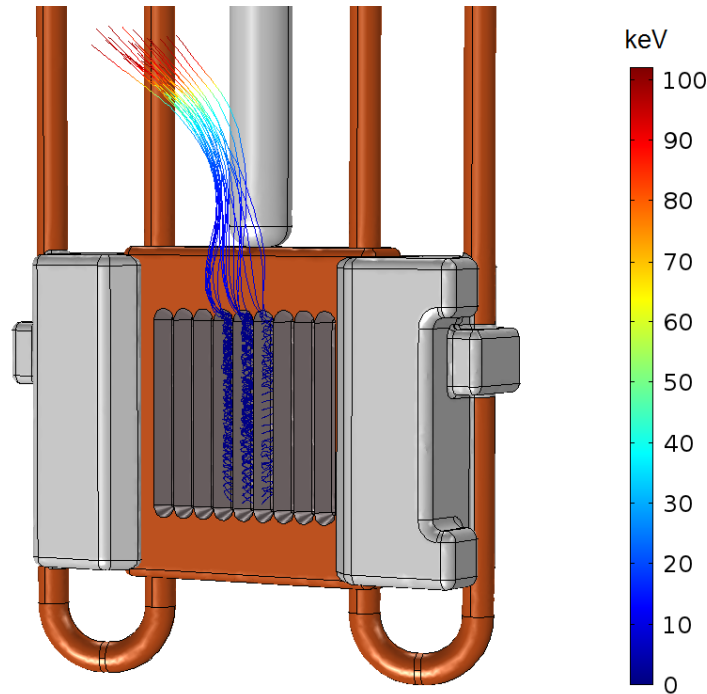


Figure 2.3: Comsol electron path simulation

arrow location. The magnetic field strength at the center of the target is approximately 800 gauss. The field strength along the surface was verified using a Hall probe. The strength of the electrical field can be seen in Fig. 2.2b. The field is quite large near the corners of the magnet holders, approaching a value of 80 kV/cm. It is important to remain below the breakdown voltage in vacuum, which can be approximated by the following ([17]):

$$E_{max} = \frac{8000}{V} \quad (2.8)$$

where V is the extraction voltage (kV) and E_{max} is in kV/cm. At 100 kV, the breakdown voltage becomes approximately 80 kV/cm.

Fig. 2.3 shows the Comsol simulated electron paths, assuming 3 strips of deuterium beams striking the center of the angled target. The voltage of the target is -100 kV. The electrons liberated by the deuterium beams spiral up the target due to the $E \times B$ drift. When the electrons reach an area of weakened magnetic field, the electric field dominates and the electrons accelerate to the vacuum chamber wall. Experimental tests confirmed the electrons were colliding with the vacuum chamber wall exactly in the location shown by the Comsol simulation.

Further analyzing the Comsol simulation shows that when the electrons spiral back toward the target, they get close to the surface but do not collide. The magnetic force a particle feels is proportional to its velocity. The electron slows down as it spirals back toward the surface due to the electric field, causing the magnetic force to weaken. This leads

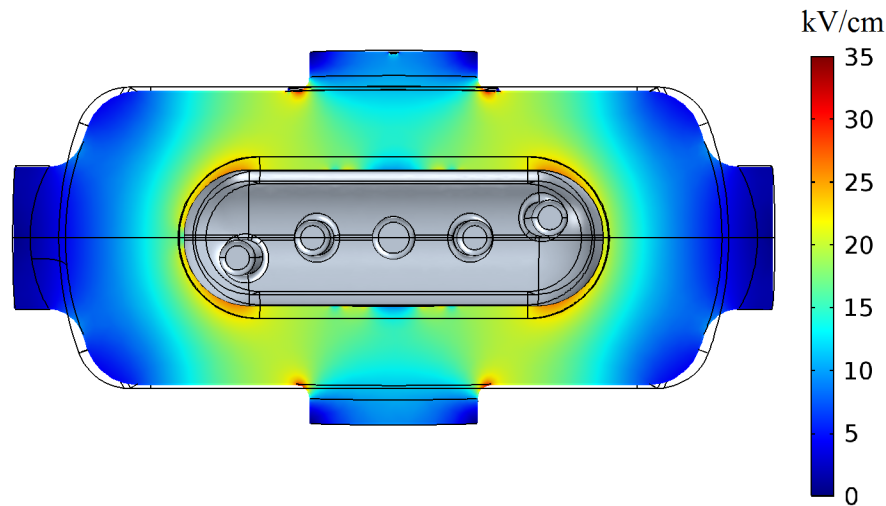


Figure 2.4: Electric field simulation outside shroud with target potential at -100 kV and shroud potential at -102 kV

to a possible conclusion that since magnetic fields can only change the path of the electron and do not add energy, it is difficult for the electrons to overcome the electric field force and recombine with the target.

2.3 Electrostatic Shroud

As previously discussed in chapter 1.3, an electrostatic shroud is a device that suppresses back-streaming electrons by introducing an opposing electric field near the target surface. This is done by installing a shroud around the target that is kept at a more negative potential. Locally the resulting electric field is directed away from the target surface, causing electrons to be repelled from the shroud and back to the target.

Figure 2.4 shows the simulation of the electric field with the installation of the shroud design shown in Fig. 1.7. In the simulation, the shroud voltage is -102 kV, while the target is at -100 kV. Installation of the shroud reduced the distance between the ground and high voltage, but by designing the shroud to have a large radius of curvature everywhere, and installing insulating spacers to move the ion sources back, it was possible to the the electric fields below the 80 kV/cm electrical breakdown limit determined earlier. The maximum electric field is approximately 47 kV/cm near the top of the shroud, and a maximum of 35 kV/cm in the plane central to the deuteron beam.

The minimum voltage differential between the target and shroud required to suppress electrons was determined by analyzing the electric field within the shroud. Figure 2.5 shows the magnitude of the electric field along the direction of the deuteron beam on the central plane within the shroud (same cross section plane shown in Fig. ??). Red areas have a

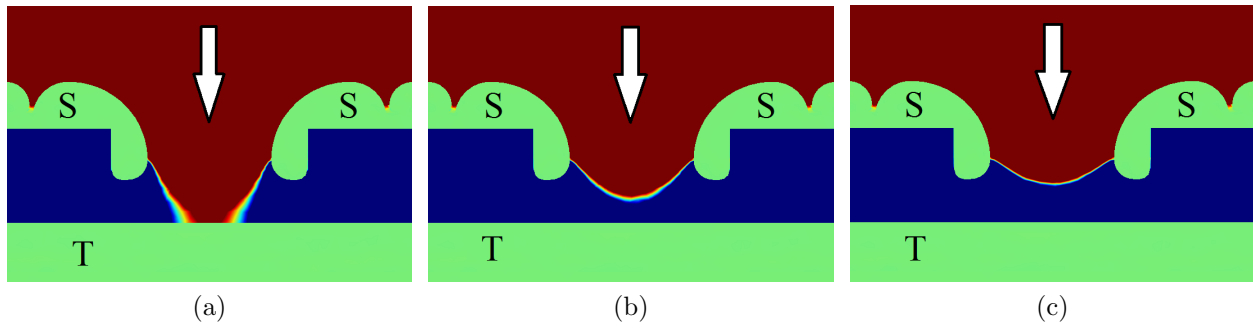


Figure 2.5: Electric field direction near shroud window at (a) 400 V, (b) 800 V, (c) and 1400 V voltage differential. Red indicates field along the direction of the deuteron beam (shown by arrow), blue indicates direction opposite the deuteron beam. T and S denote the target and shroud, respectively.

positive electric field (in the direction along the deuteron beam), and blue areas have a negative electric field. For a deuteron extracted from the top of Fig. 2.4, the electric field will accelerate the deuteron downwards toward the target. When the deuteron enters the shroud and reaches the intersection of the red and blue region, it will have an energy of approximately 102 keV. The red region will then decelerate the deuteron to 100 keV. When the deuteron strikes the target surface and ejects electrons, the electrons will feel the electric force pushing it back toward the target. An optimal design ensures that the red region for the top of Fig. 2.4 does not touch the target, thus preventing an electron from being ejected into an electric field that would accelerate the particle toward the vacuum chamber wall. Factors that effect the electric field within the shroud include the voltage differential and distance between the shroud and target, as well as the window size.

A simulation of the secondary electrons released into 2π from a 1.3 mA deuterium beam striking the flat target surface is shown in Fig. 2.6. Assuming 1.2 electrons released per deuteron ion striking the target, this results in 1.56 mA of electrons. As expected and described previously due to the electric field shown in Fig. 2.5a, for a 400 V voltage differential between the shroud and the target, secondary electrons are not suppressed and leave through the shroud window in a beam that eventually strikes the chamber with an energy of 100 keV. A shroud voltage differential of 800 V results in the electrons returning to the surface of the shroud, as seen in Fig. 2.6b. The maximum energy the electron receives is equal to the energy at release.

Testing of the shroud at 800 V voltage differential or greater on the HFNG has shown a large reduction in the amount of secondary electrons hitting the vacuum chamber. After implementing the shroud, no visual sign of chamber heating could be seen during machine operation due to back-streaming electrons. Also, the dose of bremsstrahlung X-rays detected by a geiger detector in the vault decreased by a factor of more than 20 compared to the magnetic suppression technique.

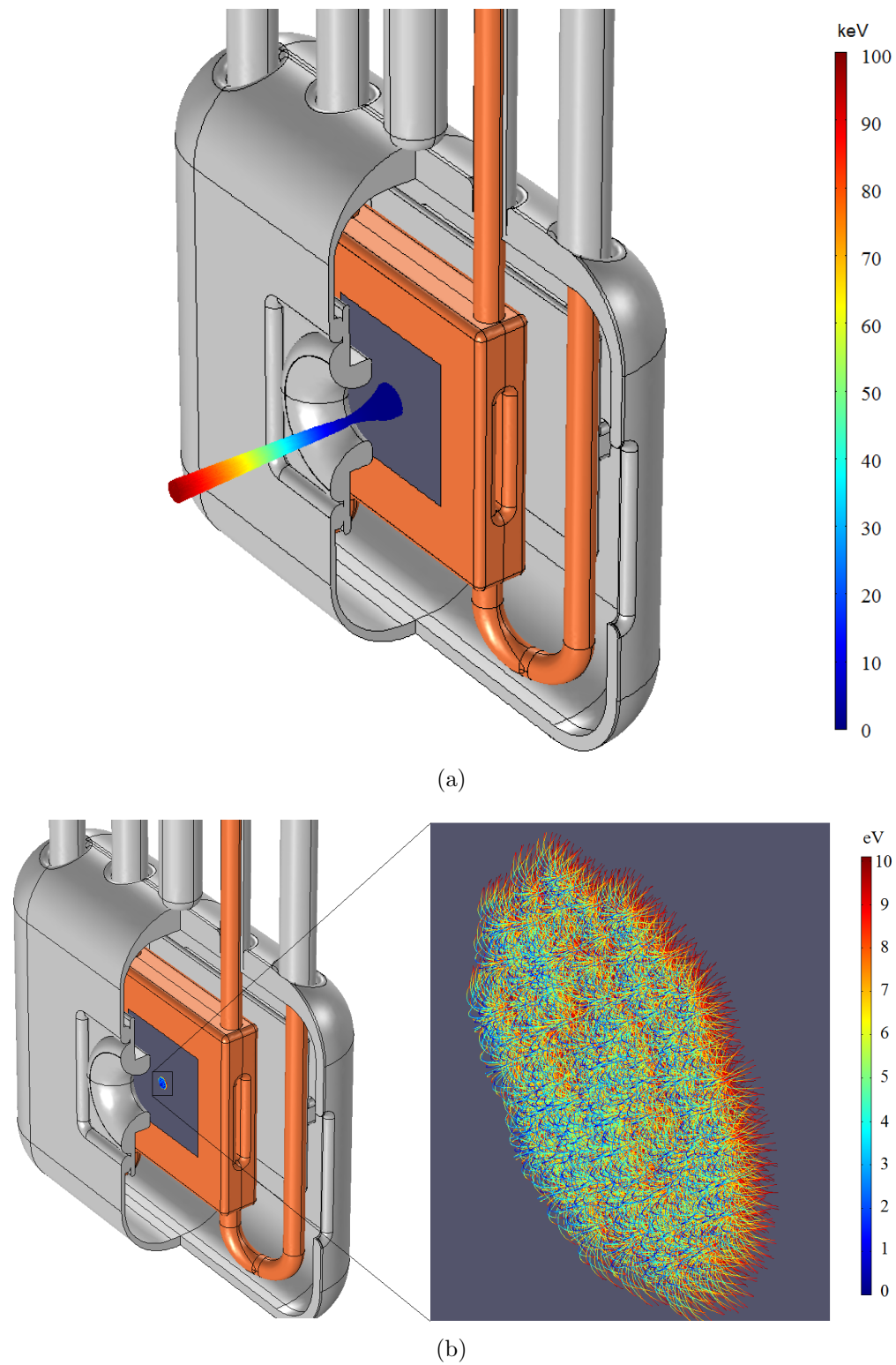


Figure 2.6: Cutaway view of secondary electron trajectories with shroud differential voltages of (a) 400 V and (b) 800 V at 100 kV target potential

Chapter 3

Target Analysis

3.1 Titanium Sputtering

As the deuterons strike the target, they lose energy primarily via electronic stopping, but as they slow down and fall below a critical energy nuclear recoils begin to dominate the energy loss. This process is described by the Kinchin-Pease model, in which nuclear recoils will occur until the primary deuteron falls below the threshold displacement energy of a titanium atom in the target. If a recoil occurs near the surface, a titanium atom may sputter off if it gains energy exceeding the surface binding energy. A surface binding energy of 4.9 eV for titanium was used in the simulation program Stopping and Ranges of Ions in Matter (SRIM) to determine the sputtering rate of the HFNG target. SRIM uses statistical algorithms in a quantum mechanical framework to determine ion and target atom interactions as described in Ref. [18]. Calculations of the sputtering rates are important in determining the average lifetime of a target. Without the titanium on the target surface, the self-loading ability off the target is limited due to the fact that the underlying copper does not getter deuterium well.

Figure 3.1 shows the energy deposition from a SRIM analysis for a 100 keV deuterium ion beam entering the angled and flat targets shown in Fig. 1.6. The SRIM calculation mode

Table 3.1: SRIM analysis: 100 keV, 1.3 mA deuteron beam

Item	Angled Target	Flat Target
Average Deuteron range normal to surface (μm)	0.34	0.85
Beam area at target (cm^2)	0.37	0.14
Displacements/Atom	32	33
Sputtering rate (titanium atom/deuteron)	0.00850	0.00174
Sputtering rate ($\mu\text{m}/\text{hr}$)	0.1184	0.0647
Titanium layer thickness (μm)	20	125
Time until titanium fully depleted (hrs)	168.8	1931

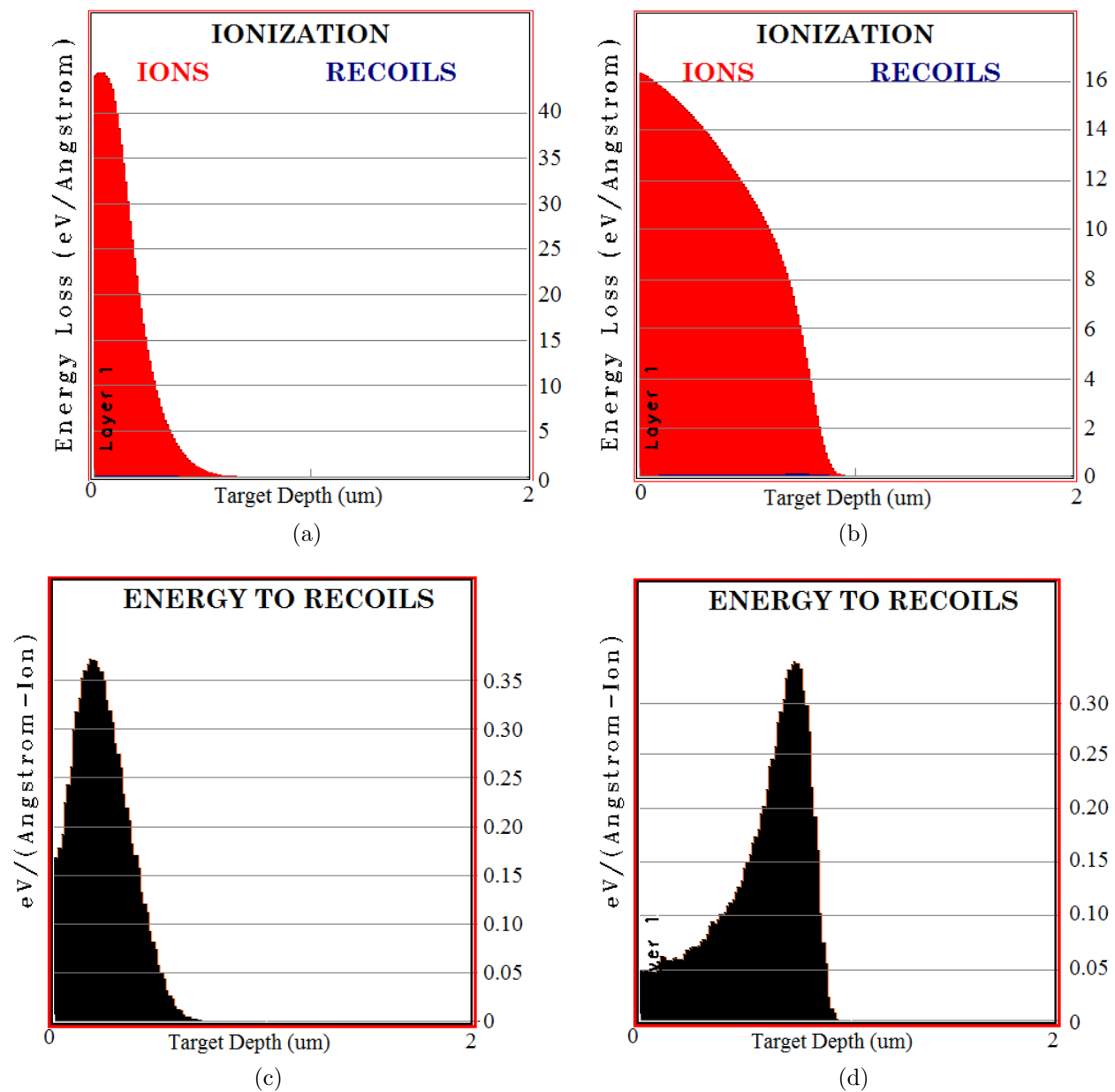


Figure 3.1: Deuteron energy loss in titanium target due to ionization for (a) 67.5 deg. and (b) 0 deg. particle entrance. Energy loss to recoils with titanium target atoms for (c) 67.5 deg. and (d) 0 deg. particle entrance angles.

used was monolayer collision/surface sputtering. The projectile ion chosen was hydrogen, with the mass adjusted to that of deuterium (2.014 amu). The target material is titanium, with a density of 4.52 g/cm³. Figures (a) and (c) show the energy loss of the deuteron as it embeds in the 67.5 degree target, while (b) and (d) show the results from the flat target. In the angled target, most of the ions stop and deposit their energy within 0.34 microns of the target surface while in the flat target the deuteron range is about 2.5 times farther. This gives the flat target a reduced sputtering rate per incoming deuteron since more of the energy is deposited farther away from the target surface. The analyzed results from SRIM are displayed in Table 3.1.

For a uniform current density 4.2 mm diameter deuterium beam, the area striking a flat target is 0.14 cm², while for the angled target the beam area becomes 0.37 cm². Although the beam current density is lower for the angled target, the sputtering per deuteron ion is approximately twice that of the flat target. The explosion bonded process allows for a thicker titanium layer on the flat target, so overall the titanium layer takes about 11.5 times longer to completely deplete compared to that of the angled target. The design of the flat target allows for the titanium bonded copper insert to be de-soldered and replaced when necessary.

3.2 Target Heat Analysis: Subcooled Boiling Overview

Deuteron current densities in the HFNG at extraction are approximately 15-20 mA/cm², depending on the plasma density and ion temperature in the source as well as the geometry of the extraction plate. As deuteron ions travel toward the target, space charge causes the beam to spread. Current densities at target then become around 9-12 mA/cm², more analysis of the beam profile is discussed in Chapter 4. At 100 keV, these current densities result in a heat flux of 900-1200 W/cm². For comparison, the heat flux generated from a computer processor is approximately 50-100 W/cm². The ability of titanium to getter hydrogen degrades at temperatures above 400°C as shown in Ref. [19]. Heat deposited in the flat target shown in Fig. 1.6b is removed by deionized water flowing through 20 cooling channels, 10 for each side of the target. Copper is chosen as the main target material due to its superior electrical and heat conductivity.

Considering the high heat fluxes, it is most likely that temperatures along the walls of the cooling channels will be higher than the saturation temperature of the cooling water. This extends the convective heat transfer analysis to regimes of boiling. Figure 3.2 shows the varying regimes of boiling for forced convection depending on the superheat of the wall, or the difference in temperature of the cooling channel wall and the saturation temperature of the cooling fluid. At low values of superheat, the cooling mechanism departs from single phase flow and enters nucleate boiling. This regime includes sub-cooled boiling in which the bulk liquid flow is at a temperature lower than the saturation temperature. Boiling occurs at the walls, and the vapor from the boiling enters the bulk liquid flow and condenses back

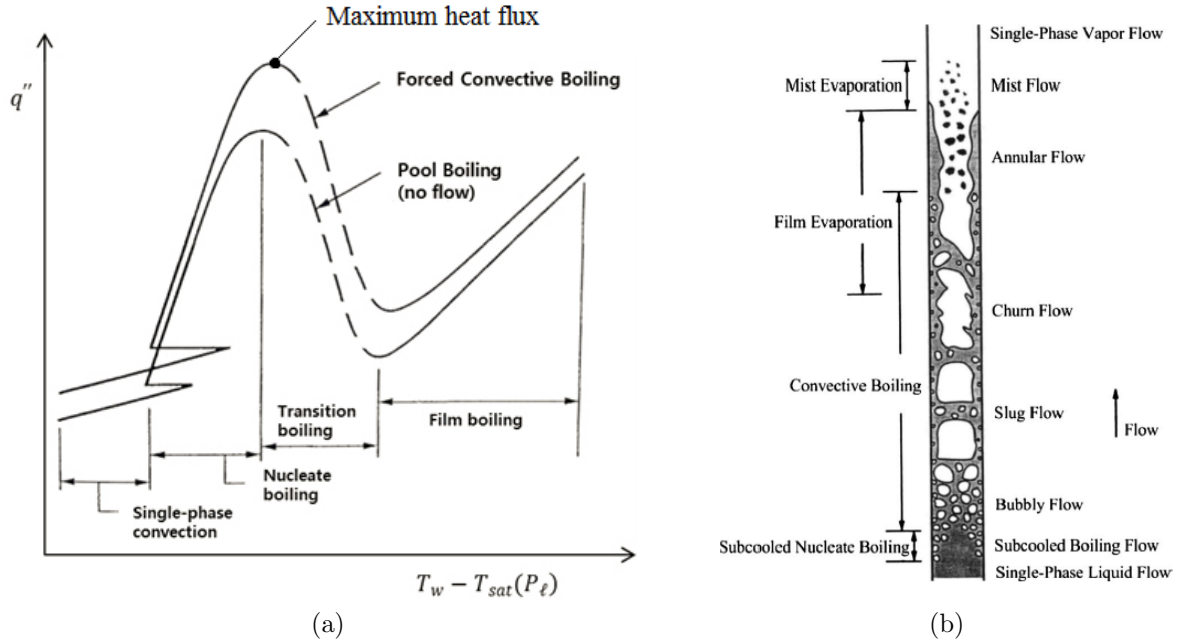


Figure 3.2: Boiling regimes corresponding to wall superheat (Ref. [20])

to liquid, as can be seen in the lower section of the vertical pipe in Fig. 3.2b. If the heat flux is too high and surpasses the critical heat flux (q''_{crit}), the system will depart from subcooled boiling and enter transition or film boiling. These regimes are usually avoided due to lower heat transfer rates resulting in higher wall temperatures. Also, if the quality is high dry-out can occur, resulting in dry regions along the water channel walls that will result in minimum heat transfer and high temperatures.

For the HFNG cooling system, sub-cooled boiling is ideal due to the lower temperatures created by the high heat removal rate created by the addition of boiling. Many correlations for subcooled boiling developed by Bergles, Rohsenow, and Hsu and others found in Ref. [20] will be presented for the heat transfer analysis of the HFNG. The regime of subcooled boiling occurs when the heat flux is in-between the onset of nucleate boiling heat flux and the critical heat flux. The relation for wall heat flux at the onset of nucleate boiling proposed by Rohsenow is as follows

$$q''_{ONB} = 5.30P^{1.156}[1.80(T_w - T_{sat})_{ONB}]^{\frac{2.41}{P^{0.0234}}} \quad (3.1)$$

where P is the fluid pressure (kPa), T_w is the cooling channel wall temperature ($^{\circ}\text{C}$), and T_{sat} is the fluid saturation temperature ($^{\circ}\text{C}$). This relation is valid for fluid pressures in the range of 103 to 13,700 kPa. A correlation for the critical heat flux proposed by Celeta et al. is

$$q''_{crit} = \frac{C_C G h_{lv}}{Re^{0.5}} \quad (3.2)$$

$$C_C = (0.216 + 0.0474P)\psi \quad (3.3)$$

$$\psi = \begin{cases} 1 & \chi_{out} < -0.1 \\ 0.825 + 0.986\chi_{out} & 0 > \chi_{out} > -0.1 \end{cases} \quad (3.4)$$

where h_{lv} is the latent heat of vaporization (J/kg), Re is the Reynolds number due to the bulk liquid flow at the outlet, G is the mass flux ($\text{kg}/\text{m}^2 \text{ s}$), μ_l is the liquid viscosity (Pa s), and χ_{out} is the outlet quality. In the subcooled boiling regime, Rohsenow developed a correlation for the total heat flux involving the addition of a single phase and nucleate boiling contribution, shown in equations (3.5) - (3.7).

$$q''_{total} = q''_{spl} + q''_{snb} \quad (3.5)$$

$$q''_{spl} = h_{le}[T_w - T_l(z)] \quad (3.6)$$

$$q''_{snb} = \mu_l h_{lv} \left[\frac{g(\rho_l - \rho_v)}{\sigma} \right]^{1/2} Pr_l^{-s/r} \left[\frac{c_{pl}[T_w - T_{sat}(P_l)]}{C_{sf} h_{lv}} \right]^{1/r} \quad (3.7)$$

For equation 3.7, $r = 0.33$ and $s=1.0$ for water and $C_{sf} = 0.013$ for water in a vertical copper tube. Pr_l is the liquid Prandtl number, h_{le} is the convective heat transfer coefficient ($\text{W}/\text{m}^2 \text{ K}$), c_{pl} is the specific heat of the liquid ($\text{J}/\text{kg K}$), μ_l is the liquid dynamic viscosity (Pa s), σ is surface tension of the fluid (N/m), and ρ_l and ρ_v are the liquid and vapor densities (kg/m^3), respectively. For fully developed turbulent flow ($Re > 4000$), the convective heat transfer coefficient can be determined by equation 3.8.

$$h_{le} = 0.023 \left(\frac{k_l}{D} \right) Re_{le}^{0.8} Pr_l^{0.4} \quad (3.8)$$

Using these equations, the heat flux removed at the cooling channel walls and the corresponding wall temperatures can be approximated.

3.3 Finite Differences Method Including Subcooled Boiling Heat Transfer

A 2D heat transfer calculation using a finite differences method (FDM) was created to determine the temperature profile in the flat target inserts of the HFNG. A FDM approximates differential equations using difference equations in a nodal mesh and relies upon iteration between nodes to converge upon a solution. The cross section of the target analyzed is along the center of where the deuteron beam strikes the titanium surface and can be seen in Fig.

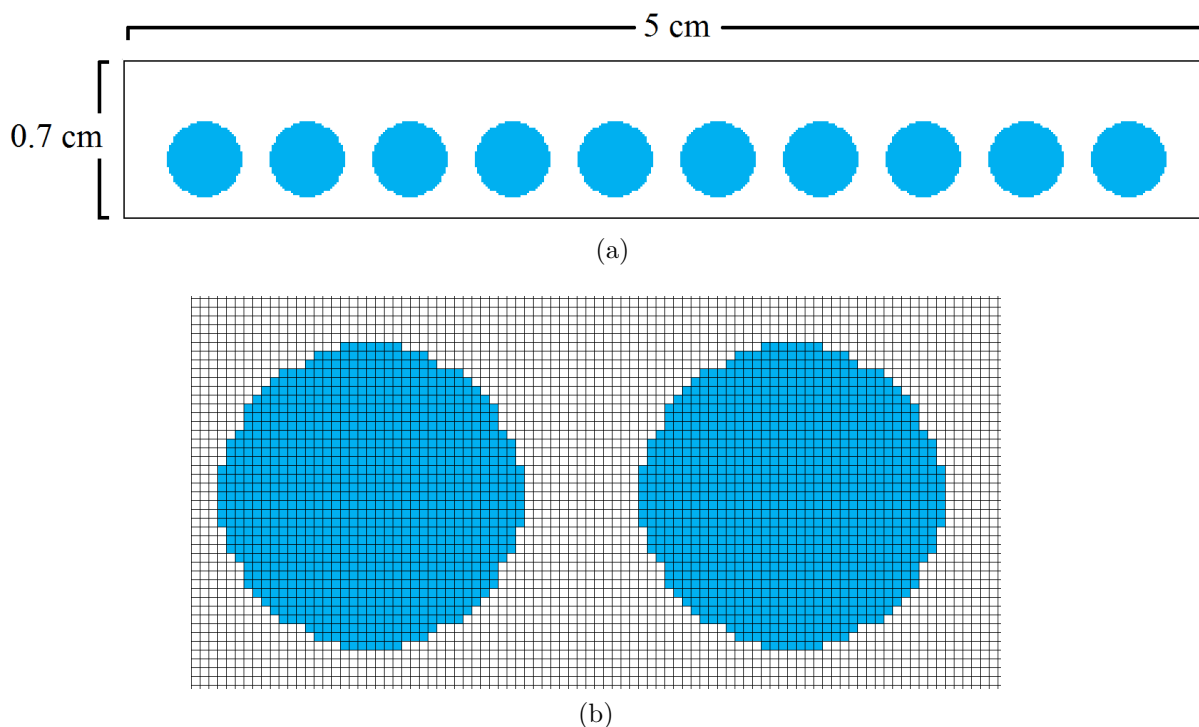


Figure 3.3: FDM nodal grid cross section. Nodes are at center of each square. (a) Cross section along center of target, blue shaded regions are water channels. (b) Nodal grid of water channels

3.3. Using a two-dimensional calculation of temperatures along the central plane is a conservative approach. This is due to the fact that along the center cut of a gaussian shaped beam (along the x-axis in the beam center), all values of heat flux above and below the cut plane would be lower within the beam area. This would result in a heat flow out of the central cut-plane in a three-dimensional calculation, which would further reduce the calculated temperatures. The following analysis is completed for one ion beam striking one half the target, since the HFNG is symmetric identical results are expected for an ion beam impinging on the other half of the target. The grid size used in the analysis is 0.1 mm between nodes in both the vertical and horizontal directions. A 0.125 mm nodal layer is added for the titanium layer on the surface. A nodal mesh resolution of 0.1 mm resulted in the circumference of the water channel mesh being about 3% larger than the actual circumference of the water channel.

Two methods of heat transfer are apparent in the target, conduction and convection. Since it is required to keep temperatures below 400°C , one assumption is that radiative heat losses can be ignored since they are small relative to the heat flux of the incoming deuteron beam. Testing this assumption post analysis gave agreeing results, for an example case of a 1000 W/cm^2 deuteron beam with a 5 mm beam diameter, the total calculated radiative heat

flux was 5.5% of the beam heat flux. Ignoring the radiative heat losses simplifies the analysis so the beam heating becomes equal yet opposite to the total convective water heat removed ($q_{beam} = -q_{convection}$). Not including the radiative heat flux also makes the temperature calculation more conservative, as calculated temperatures will be slightly higher since the radiative heat leaving the target is ignored.

Fourier's law of heat conduction is used to determine the temperature gradients throughout the titanium and copper within the target. Fourier's law is given as follows

$$q'' = -k\nabla T \quad (3.9)$$

where ∇T is the temperature gradient. At the titanium/copper interface, perfect thermal contact is assumed since the materials are strongly bonded by an explosion bonding process. Constant thermal conductivities corresponding to a temperature of about 300 °C were used for both titanium and pure copper (values from Ref. [21]). Temperatures at cooling channel walls are then calculated using convective boundary conditions, either single phase or sub-cooled boiling depending on the given heat flux at the wall. An adiabatic wall condition is used along surfaces that meet vacuum. The different types of boundary conditions used in the FDM is shown in Fig. 3.4.

To determine the equation used in each node, the energy balance method was used. To begin, the purely conductive heat transfer nodal square shown in Fig. 3.4a will be analyzed. The node represents the temperature within a square of width ΔX and height ΔY with the node at the center. Fourier's law of conduction in one dimension is as follows

$$q'' = -k \frac{dT}{dx} \quad (3.10)$$

where x denotes the horizontal direction, and y will represent the vertical direction. At steady state, the heat flux flowing into and out of the square for that node must sum to 0. This leads to the results shown in equation 3.11.

$$0 = -k \frac{\Delta Y (T_{i-1,j} - T_{i,j})}{\Delta X} - k \frac{\Delta Y (T_{i+1,j} - T_{i,j})}{\Delta X} - k \frac{\Delta X (T_{i,j+1} - T_{i,j})}{\Delta Y} - k \frac{\Delta X (T_{i,j-1} - T_{i,j})}{\Delta Y} \quad (3.11)$$

Given that $\Delta X = \Delta Y$, solving for $T_{i,j}$ gives the following:

$$T_{i,j} = \frac{T_{i+1,j} + T_{i-1,j} + T_{i,j+1} + T_{i,j-1}}{4}. \quad (3.12)$$

which is just the average of the surrounding nodes. For the adiabatic wall condition shown in Fig. 3.4b, no heat transfer occurs across the vacuum/target interface. Heat conduction occurs horizontally across half the nodal square and vertically from below. This results in the following expression:

$$0 = -k \frac{\Delta Y}{2} \frac{(T_{i-1,j} - T_{i,j})}{\Delta X} - k \frac{\Delta Y}{2} \frac{(T_{i+1,j} - T_{i,j})}{\Delta X} - k \frac{\Delta X (T_{i,j-1} - T_{i,j})}{\Delta Y} \quad (3.13)$$

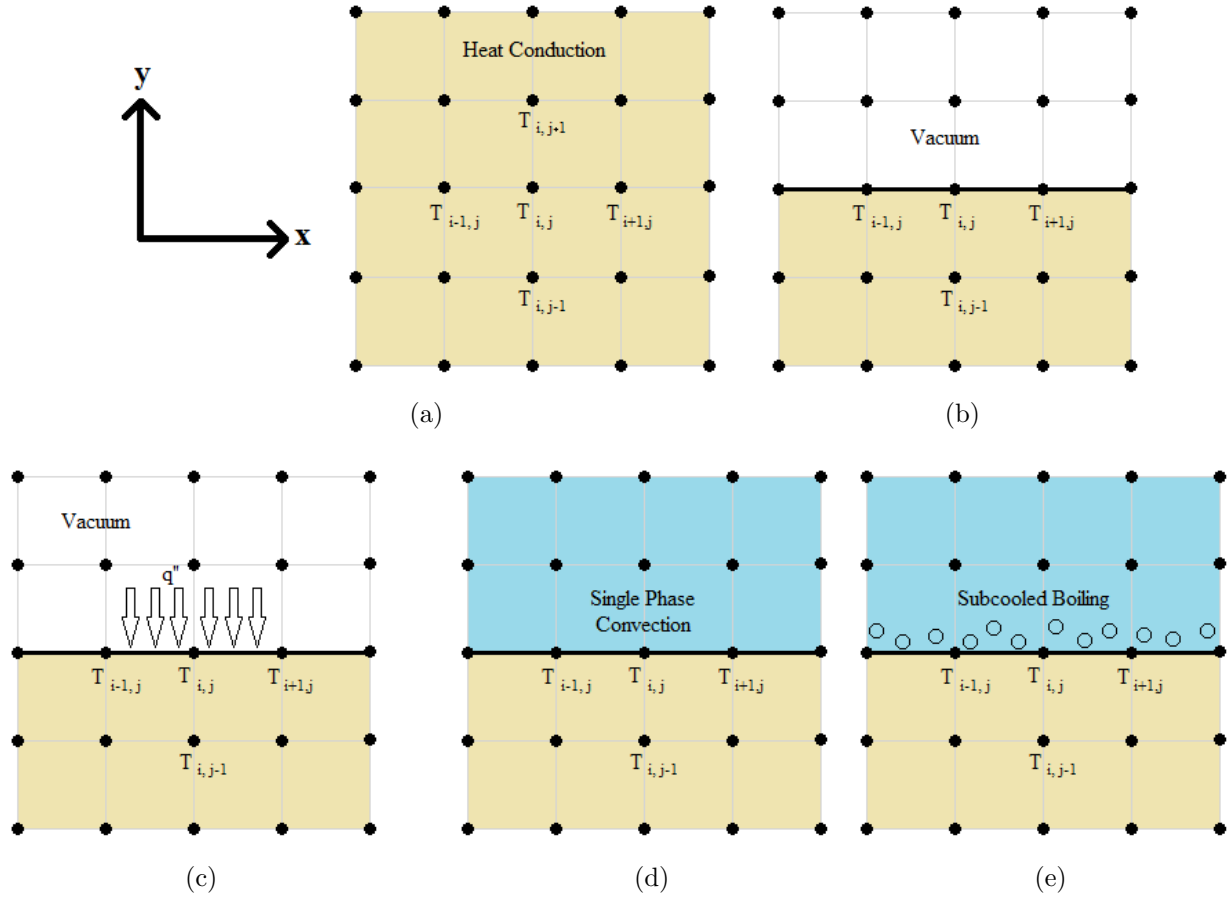


Figure 3.4: Finite differences grid setup for various heat transfer modes and boundary conditions: (a) heat conduction, (b) adiabatic wall, (c) surface heat flux, (d) single phase convection, (e) subcooled boiling

Simplifying then gives:

$$T_{i,j} = \frac{T_{i-1,j} + T_{i+1,j} + 2T_{i,j-1}}{4} \quad (3.14)$$

For the surface heat flux boundary condition in Fig. 3.4c, a similar treatment to the adiabatic boundary condition gives:

$$T_{i,j} = \frac{(T_{i-1,j} + T_{i+1,j})}{4} + \frac{T_{i,j-1}}{2} + \frac{\Delta X q''}{2k} \quad (3.15)$$

The heat flux across the cooling channel surface for single-phase convection boundary condition in Fig. 3.4d is calculated using equation (3.6). The corresponding FDM node tem-

perature equation then becomes

$$T_{i,j} = \frac{T_{i-1,j} + T_{i+1,j} + 2T_{i-1,j} + \frac{2h_{le}\Delta XT_l}{k}}{2\left(\frac{h_{le}\Delta X}{k} + 2\right)} \quad (3.16)$$

When the temperature threshold for the onset of nucleate boiling is surpassed, as determined by solving equation (3.1), the subcooled nucleate boiling heat flux, equation (3.7), is added to the convective boundary condition resulting in the following node temperature equation:

$$T_{i,j} = \frac{T_{i-1,j} + T_{i+1,j} + 2T_{i-1,j} + \frac{2\Delta X}{k}(h_{le}T_l - C(T_{i,j} - T_{sat})^{1/r})}{2\left(\frac{h_{le}\Delta X}{k} + 2\right)} \quad (3.17)$$

where C is

$$C = \mu_l h_{lv} \left[\frac{g(\rho_l - \rho_v)}{\sigma} \right]^{1/2} Pr_l^{-s/r} \left[\frac{c_{pl}}{C_{sf} h_{lv}} \right]^{1/r} \quad (3.18)$$

The node temperature for equation (3.17) does not have an explicit solution as $T_{i,j}$ appears on both sides of the equation. The solution is determined implicitly using iteration. Figure 3.4 only shows the basic geometry boundaries used in the FDM analysis of the HFNG target. For other boundary shapes with their corresponding node temperature equations, see Appendix A.

An example input to the developed HFNG FDM target temperature calculation program is shown in Fig. 3.5. Water properties from NIST (Ref. [22]) are determined using fits to data tables based on water pressure. As previously mentioned, the geometry and grid setup used is shown in Fig. 3.3. A user defined heat flux (either uniform or a distribution) is entered along the top surface, and heat is removed via the 10 water channels. The water mass flow is split equally into each channel (10 water channels per half of the target, 20 water channels total). The program iteratively calculates the temperature at each node. When the heat flux for the onset of nucleate boiling is reached at a water channel wall node, the nodal equation then adds the contribution to subcooled boiling (equation (3.17)). The solution normally takes over 30,000 iterations to converge. The program assumes convergence if after 500 iterations the total heat flux removed in the water channels changes by less than 0.001 W/cm. The program output includes temperatures at all nodes, as well as a temperature contour map. The status of all the wall nodes is also recorded, with information including the boiling condition and the heat flux through the nodes. Global results such as the maximum surface temperature and cooling channel wall heat flux relative to the critical heat flux is given.

Validation of the energy balance results from the FDM calculations can be seen in Table 3.2 for a 5 mm diameter uniform heat flux beam. The convergence criteria was by the number of iterations required until the change in heat flux removed by the water was less than 0.001 W/m. Two criteria values were chosen for the results in Table 3.2. It can be seen that the residual difference between the heat removed by the water and the amount

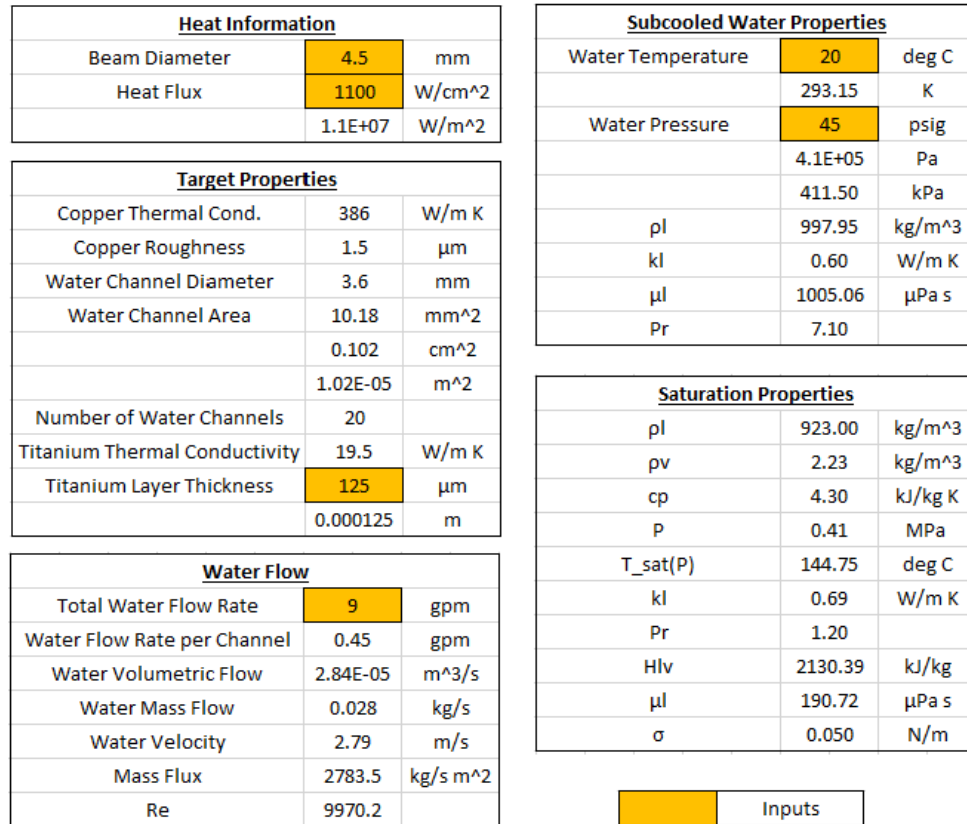


Figure 3.5: Inputs and calculated water properties for the HFNG FDM temperature calculator

Table 3.2: Energy Balance Validation for 5 mm Beam Diameter

Beam Heat Flux (W/cm ²)	Convergence Criteria (# of Iterations)	Beam Deposited Heat (·10 ⁴ W/m)	Heat Removed by Water (·10 ⁴ W/m)	% Difference
1000	500	5.00	4.85	3.1
1000	5000	5.00	4.88	2.5
1300	500	6.50	6.32	2.8
1300	5000	6.50	6.33	2.6

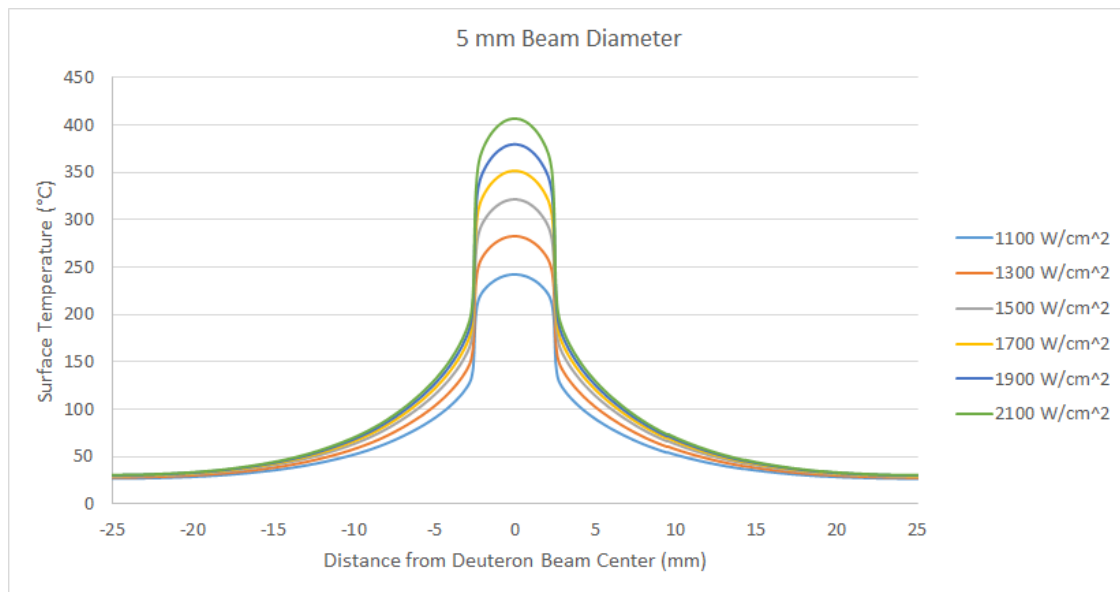
deposited by the beam is between 2.5-3.1%. Changing the convergence criteria from 500 to 5000 iterations resulted in slightly more accurate results, but the calculation time greatly increased.

3.4 HFNG Target Temperatures: Calculated Results

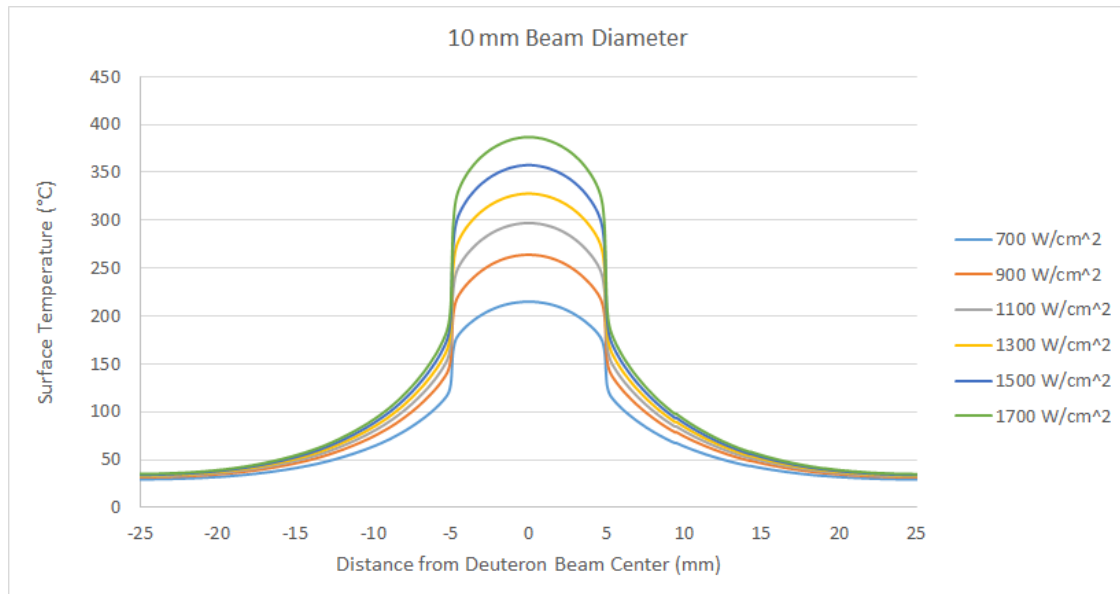
The previously described FDM program was used to analyze the heat transfer through the HFNG target for various uniform heat flux deuterium beams of different diameters. Water input properties displayed in Fig. 3.5 were used throughout the analysis. The resulting temperatures across the titanium target surface are displayed in Fig. 3.6 for beam diameters of 5 and 10 mm. The temperature profiles at 15 mm and 20 mm, as well as temperature maps can be seen in Appendix B. The maximum temperature allowed at the surface is 400°C due to the degradation of the ability for titanium to getter deuterium. Near the edge of the target insert, temperatures are not allowed to reach above 220°C or the solder that holds the insert in place will melt. It can be seen that the temperatures near the edges never exceed 40°C, so melting of the solder will not become an issue. For a 5 mm uniform heat flux beam, a 2100 W/cm² heat flux results in the target surface exceeding 400°C. The limitation of a 10 mm diameter beam arises at approximately 1400 W/cm² when the maximum heat flux at the cooling channel wall exceeds the critical heat flux. The ratio of the maximum cooling channel wall heat flux to that of the critical heat flux at various diameters can be seen in Fig. 3.7. The analysis shows that at below approximately 6.5 mm in diameter, the limiting factor is exceeding a surface temperature of 400°C, while above 6.5 mm the critical heat flux is surpassed prior to reaching 400°C.

When heat fluxes reach a level where subcooled boiling occurs, the entire wall does not enter the subcooled boiling regime. In all of the heat fluxes given for 5-20 mm diameter deuteron beams, a maximum of 38% of a cooling channel wall boundary underwent subcooled boiling. Within the subcooled boiling region, the heat flux removed by the water was 5 times that of single phased convection.

Surface temperatures for non-uniform beam profiles that match the expected deuterium beams of the HFNG are discussed in Chapter 4.2.



(a)



(b)

Figure 3.6: Surface temperatures along the target for uniform heat flux ion beams of (a) 5 mm and (b) 10 mm diameter

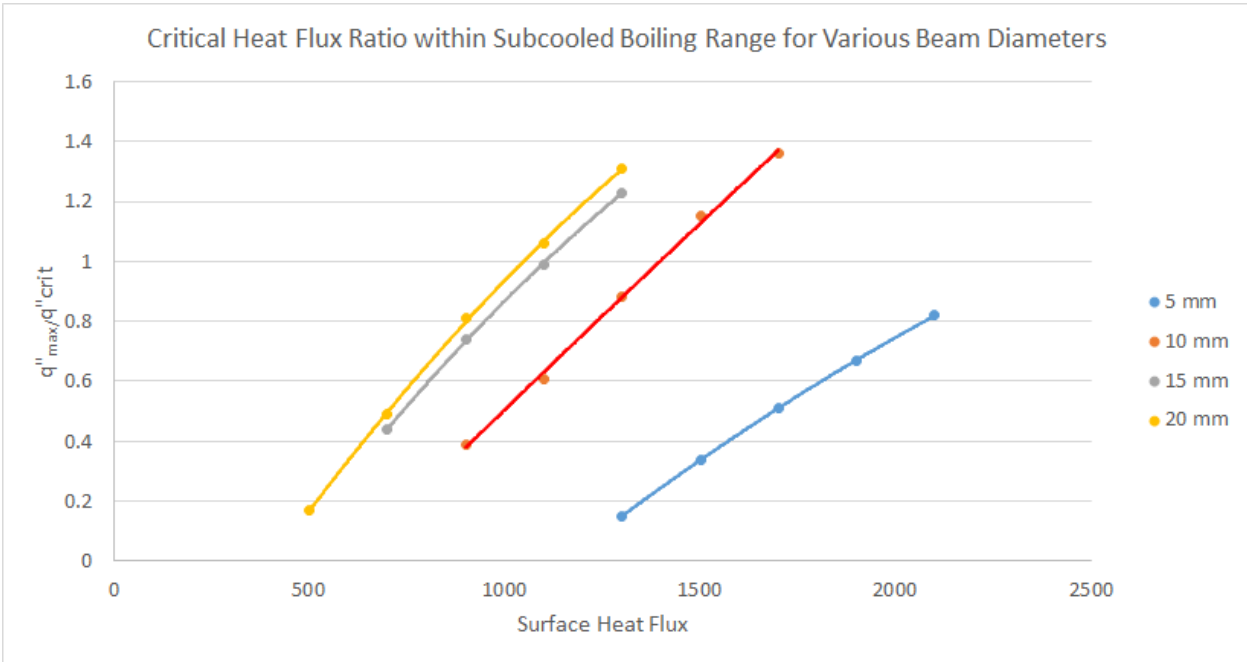


Figure 3.7: Ratio of maximum heat flux along a cooling channel wall to the critical heat flux

Chapter 4

Deuterium Beam Analysis

4.1 Plasma Meniscus and Ion Beam Simulation Overview

The plasma meniscus is the ion emission surface at the extraction electrode that separates the bulk plasma from the vacuum [13]. The shape of this surface has a large effect on the ion beam profile. The shape of the surface can be determined by analyzing Child's law and Bohr's equation for ion beam extraction. The beam current extracted between parallel plate electrodes in vacuum can be determined using Child's law, shown in equation 4.1.

$$j_c = \frac{4\epsilon_0}{9} \sqrt{\frac{2Ze}{m_i}} \frac{V_0^{3/2}}{d^2} \quad (4.1)$$

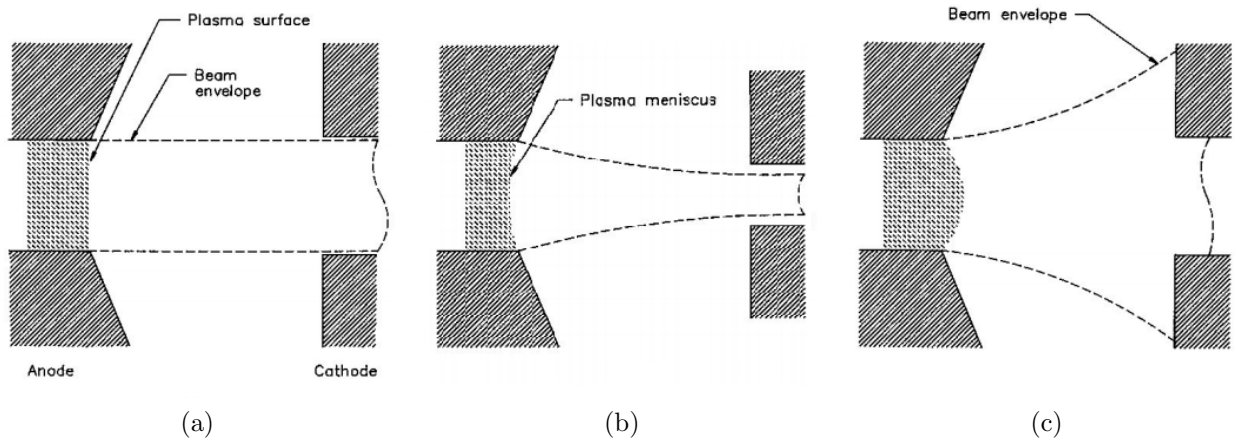


Figure 4.1: Plasma meniscus shape: (a) flat, (b) concave, and (c) convex plasma meniscus from Ref. [13]

Equation 4.2 by Bohr determines the actual current that can be extracted from a cold plasma based on the electron temperature and ion density.

$$j_b = 0.6en_i\sqrt{\frac{kT_e}{m_i}} \quad (4.2)$$

Setting equations 4.1 and 4.2 equal and solving for d gives

$$d^2 = \frac{20}{27} \frac{\epsilon_0 V_0^{3/2}}{en_i} \sqrt{\frac{2Ze}{kT_e}} \quad (4.3)$$

Equation 4.3 defines the distance necessary between the extraction electrode and the anode to create a flat plasma meniscus. Fig. 4.1 shows the effect of the plasma meniscus shape on beam extraction. A flat plasma meniscus, as shown in Fig. 4.1a, results in a parallel extracted ion beam, one that is neither converging nor diverging at extraction. Though the beam will diverge during travel due to space charge, this is the most ideal ion beam for a uniform neutron flux created at the target. Divergence of the beam can be reduced by shaping the anode to curve the electric field lines, resulting in a focusing force.

A concave and convex plasma meniscus, as shown in Fig. 4.1b and 4.1c, results in a converging and diverging ion beam, respectively. Examining equation 4.3 can lead to the concave and convex plasma meniscus solutions. Keeping a constant voltage, lowering the ion density (n_i) or electron temperature (T_e) results in a larger distance (d). If the distance between the anode and electrode is fixed, this results in the plasma meniscus retracting into the source to increase the distance. Increasing the ion density or electron temperature has the opposite effect, which creates a convex plasma meniscus. For the HFNG, a concave plasma meniscus and a converging beam can result in overheating of the target. A convex plasma meniscus and a diverging beam results in the ion beam hitting the shroud, causing the ejection of unwanted electrons.

Comsol multiphysics was used for ion beam simulations. To speed up calculation time, Comsol simulations use a static current, meaning each particle represents a continuous stream of particles that are released at regular time intervals and follow the same path. This reduces the size of the calculation compared to tracing individual particles. Ion beam trajectories are solved by using the following iterative approach (Ref. [23]):

- 1) Solve stationary electric and magnetic fields based on user given boundary conditions (see chapter 2.2).
- 2) Run transient beam analysis. Solver solves static current particle positions for each time step, and also calculates the space charge of beam.
- 3) Recalculate the electric field including the space charge solution from step 2.
- 4) Repeat steps 2 and 3 until solution is steady. Usually this is reached at three iterations.

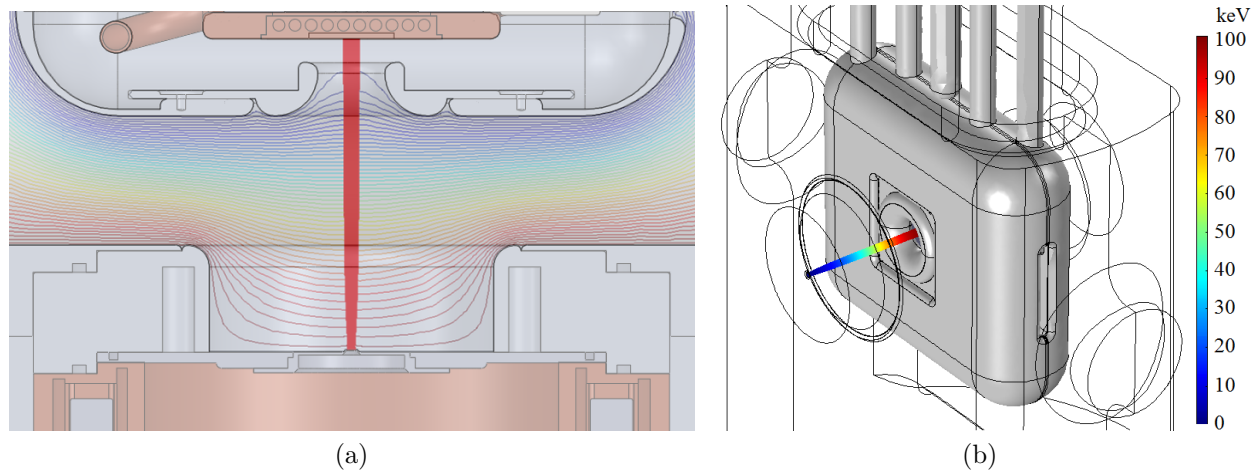


Figure 4.2: Comsol simulation of electric field and deuteron beam trajectory at 100 kV and 1.43 mA

The accuracy of the solution is highly dependent on the resolution of the geometry mesh. This is especially important in the region near extraction. In this region space charge is dominant, as the ions are closest to each other and are traveling at low velocities. This gives an increase in amount of time the ions have to repel from each other and spread. The shape of the electric field lines in this region is important as the electric force can either cause further beam divergence or convergence depending on the direction. Shaping of the extraction aperture affects the electric field in this region. A boundary layer geometry mesh is used here which creates a very fine mesh that results in length between nodes being around the same length as distance an ion travels for one time step during the solution. The boundary mesh increases in size as it gets farther from the extraction surface to reduce the total number of mesh elements and decrease the calculation time. As previously mentioned, a flat plasma meniscus is ideal, so the current density extracted in simulations is determined by equation 4.1. This allows the particles to start at a flat surface in the simulation, eliminating the necessity to determine the curvature of the emission surface.

4.2 Extraction Design and Ion Beam Optics Results

A detailed beam optics analysis for the HFNG is important to insure that the deuterium ion beam does not hit the shroud or become too focused and overheat the target surface. A successful extraction geometry and beam analysis for a 1.43 mA deuteron beam at 100 kV can be seen in Fig. 4.2, the method to achieve the results will be discussed in this section.

The addition of an electrostatic shroud for the HFNG reduced the distance between the extraction electrode and the anode to 3.81 cm. Using equation 4.1, the current density re-

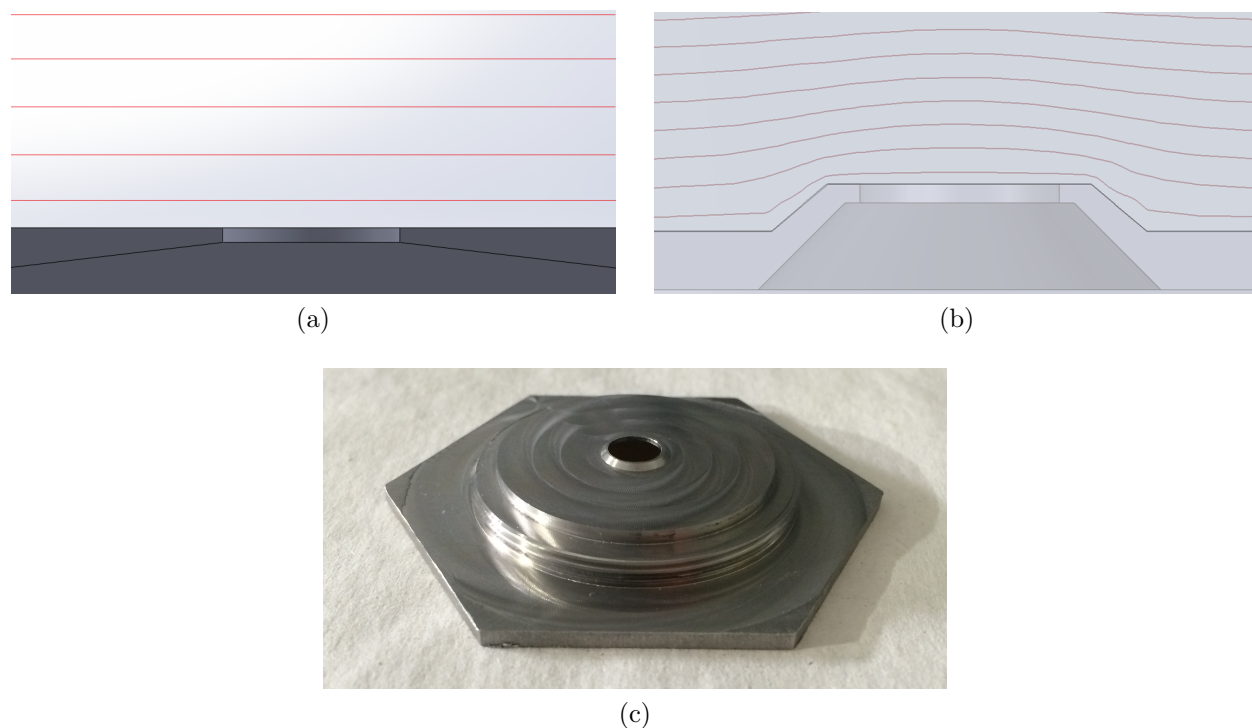


Figure 4.1: (a) Flat extraction geometry (b) electric potential shaping with an extraction nozzle (c) 10 mA at 125 kV threaded nozzle insert for the HFNG

quired to make a flat plasma meniscus at -100 kV at a distance of 3.81 cm is 84 mA/cm^2 . This value is not obtainable with the current HFNG multicusp ion source. An aluminum cylindrical spacer was added to move the ion source back by an additional 1.25 inches, lowering the current density required to make a flat plasma meniscus at -100 kV to approximately 25 mA/cm^2 .

The cylindrical spacer creates a focusing electric force at the extraction hole. This can be seen in Fig. 4.2a, where inside the cylindrical spacer at the extraction of the beam the electrical potential lines are concave. Since the magnitude of electric field is perpendicular to the equipotential lines, this results in an inward force, causing the beam to focus. In systems with a near parallel plate design, the equipotential lines are nearly parallel to the surface of the extraction plate. Assuming a flat plasma meniscus, this results in a parallel beam extraction in which the beam quickly begins to diverge due to space charge. To reduce the divergence of the beam, usually an concave chamfer is added at the extraction hole to slightly bend the equipotential lines and cause a slightly focusing electric field to counteract the repulsion force due to space charge. This is commonly called a Pierce electrode. For the case of the HFNG, the cylindrical spacer design eliminates the need of a Pierce electrode as it provides this focusing field. If the depth of the spacer is fixed, as the diameter increases, the concavity of the equipotential lines decreases, lowering the focusing force of the electric

field. Due to limitations in the ability to change the original HFNG chamber, the HFNG spacer had a maximum allowable diameter of about 8.57 cm. At the maximum diameter allowed for the given design, the focusing of the field can be too strong for a flat extraction design as shown in Fig. 4.3a, depending in the ion beam current. Figures 4.2a and 4.2c show the power density at the target of using a flat extraction plate to extract the deuteron beam with 2.7 mm (1.43 mA) and 60.5 mm (10 mA) extraction holes at 100 kV and 125 kV, respectively. A halo of increased current density occurs with a flat extraction geometry, with power densities reaching over 3000 W/cm² for the 10 mA beam case. As the beam spreads due to space charge, the further an ion makes it from the center of the beam the larger the electric field force becomes in the beam-center direction due to the concave electric field. This results in the buildup of ions along the edge of the beam.

In order to spread the neutron beam and lower the current density at the target, a convex extraction nozzle was implemented, shown in Fig. 4.2c. The nozzle rises 0.635 mm above the base of the extraction plate, and has a chamfer angle of 45°, and varies in diameter depending on the desired current to be extracted. Adding a concave nozzle to the extraction plate creates a defocussing field at extraction. As seen in Fig. 5.11, the addition of the nozzle greatly reduces the ion current density at the surface of the target. Using the FDM heat transfer calculator discussed in Chapter 3, the temperatures across the surface of the target for the 1.43 mA, 100 kV and 10 mA, 125 kV beams for the flat and nozzle extraction geometries are shown in Fig. 4.3. At 1.43 mA and 100 kV, the temperatures remained below 400°C and the critical heat fluxes for each case were far below the critical heat flux. The nozzle design results in temperatures below 150°C, and the target cooling remains in the single phase regime. At 10 mA and 125 kV, the addition of the nozzle is necessary. With the flat extraction, the target surface temperatures are near 400°C, and the heat flux at the central cooling channel walls surpass the critical heat flux. The nozzle reduces the temperatures across the surface by about 50°C with a critical heat flux ratio of 0.86.

The 1.43 mA nozzle has been tested on the HFNG. Direct temperature measurements of the target is difficult due to the target being at a -100 kV potential and it's proximity to the RF ion source. It was determined that overheating of the target did not occur as the measured neutron flux of the generator was near predicted values assuming the target was fully saturated with deuterium (approximately 1 deuteron per titanium atom). Measurement of the heat spot left on the target showed a beam diameter of approximately 5.3 mm, which is close to the simulated 5.1 mm beam diameter.

To summarize, the shape of the plasma meniscus dictates the spreading of an ion beam. This shape is set by the extraction voltage and distance between extraction and the high voltage electrode. For the HFNG, the addition of a spacer to create a distance suitable for a flat plasma meniscus resulted in the creation of a focusing electric field. To spread the deuterium beam, convex extraction nozzles were designed to create an electric field with a diverging net force at extraction. The 1.43 mA beam nozzle was successfully tested, and resulted in expected neutron fluxes for 1.43 mA and 100 kV. Further discussion of the neutron flux will be found in Chapter 5. The accurate simulation of extraction nozzles can be useful for future ion beam optics designs, as these nozzles can allow for smaller beam

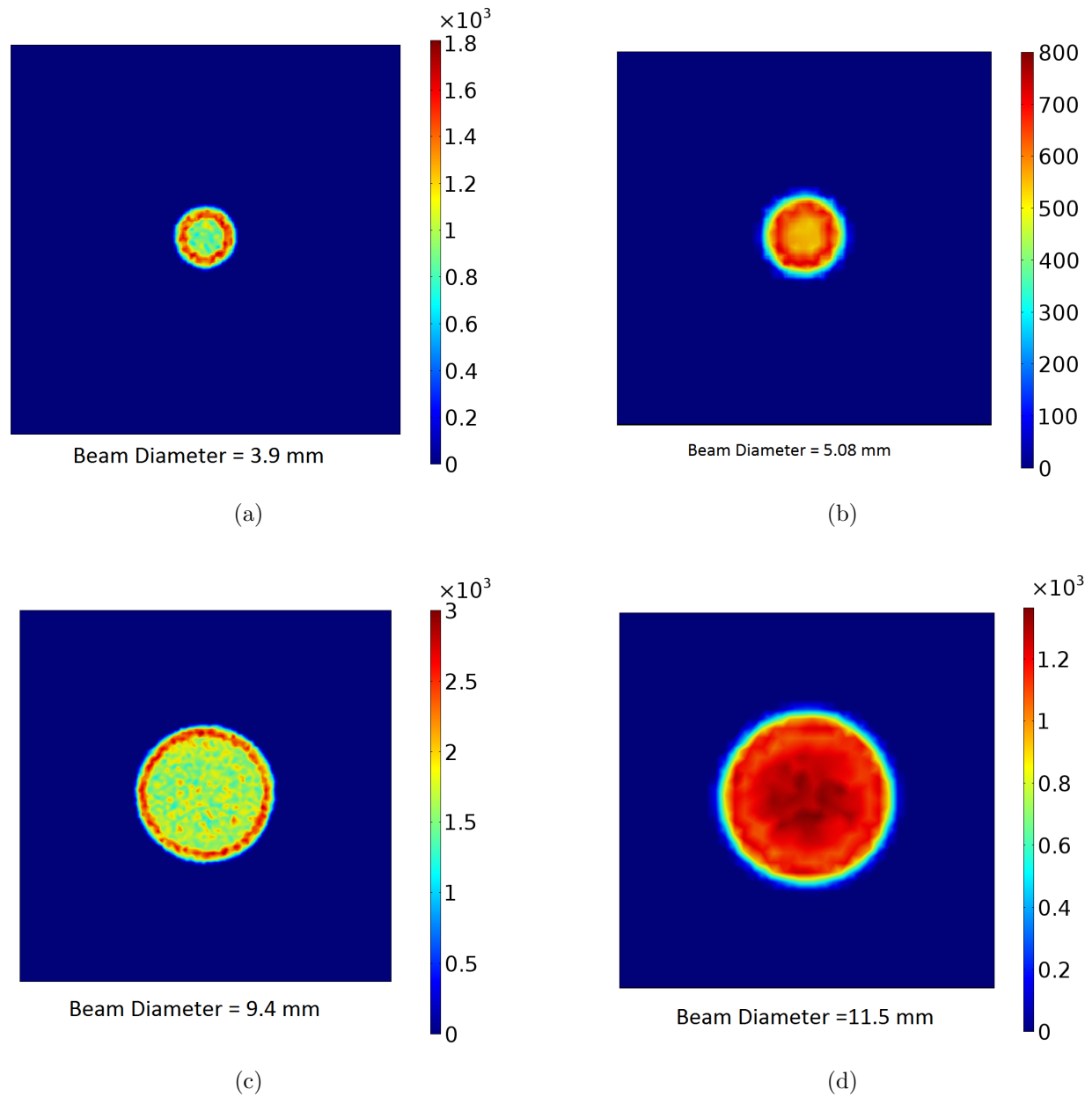


Figure 4.2: Beam Power on target for (a) 1.43 mA, 100 kV flat plate extraction; (b) 1.43 mA, 100 kV nozzle defocussing extraction; (c) 10 mA, 125 kV flat plate extraction; (d) 10 mA, 125 kV nozzle defocussing extraction

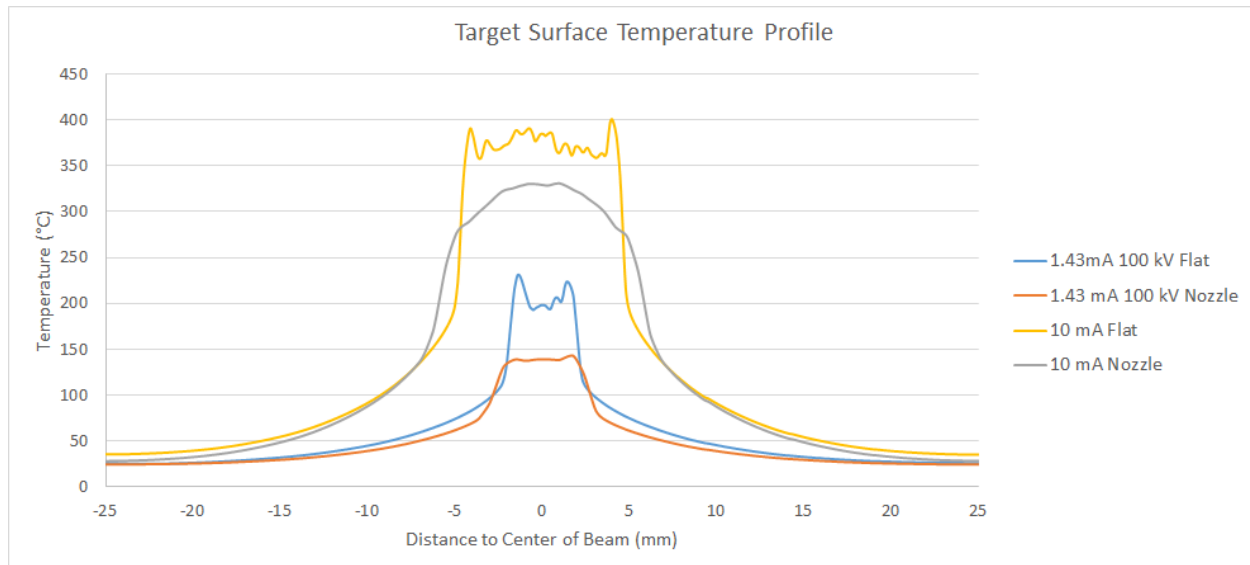


Figure 4.3: Electric potential shaping with an extraction nozzle. Convex equipotential lines result in a diverging electric field.

column diameters, creating more compact neutron generators.

Chapter 5

Neutron Flux and Distribution

5.1 Neutron Flux Analysis

Various parameters must be taken into account when estimating the neutron flux for a thick target neutron generator. As a deuteron slows down within the target, it loses energy, resulting in a reduction of the cross section for the DD-fusion reaction. Therefore, for a given incoming deuteron energy the average cross section varies along the depth of the target. When the DD fusion reaction occurs, release of neutrons is not isotropic, and the distribution relative to the incoming beam in the lab reference frame can be determined by using equation 1.6.

An important factor in calculating the neutron flux is determining the deuteron stopping power within the target, as this determines the energy of the deuteron as a function of depth as well as the total depth of implantation. The lower the stopping power, the further the implantation which increases the total reaction volume within the target. To determine the target stopping power, the implanted deuterium must be included in the calculation. Bragg's law of additivity, as described in Ref. [24] and [25], can be used to determine the stopping power in compounds. The law states that the total stopping power of a compound can be derived from the sum of its elemental stopping powers. To calculate the stopping power in a titanium hydride target, titanium and deuterium elemental stopping power data were taken from SRIM. The total calculated stopping power of a deuteron ion in a titanium hydride target with a deuterium/titanium ratio of 1 is shown in Fig. 5.1. It can be seen that the addition of deuterium implanted in titanium increases the stopping power by over a factor of two compared to that of titanium alone.

The deuterium to titanium loading ratio of the target varies by temperature, and various sources report different loading ratios (see ref. [26], [27], and [28]). An increase in the deuterium to titanium ratio increases the stopping power of the target, reducing the implantation depth and average energy at a given depth and therefore lowering the cross section, but the availability of more deuterium for DD fusion reaction opposes this reduction. A loading ratio of 1:1 is used in the calculation to predict the flux of the HFNG neutron

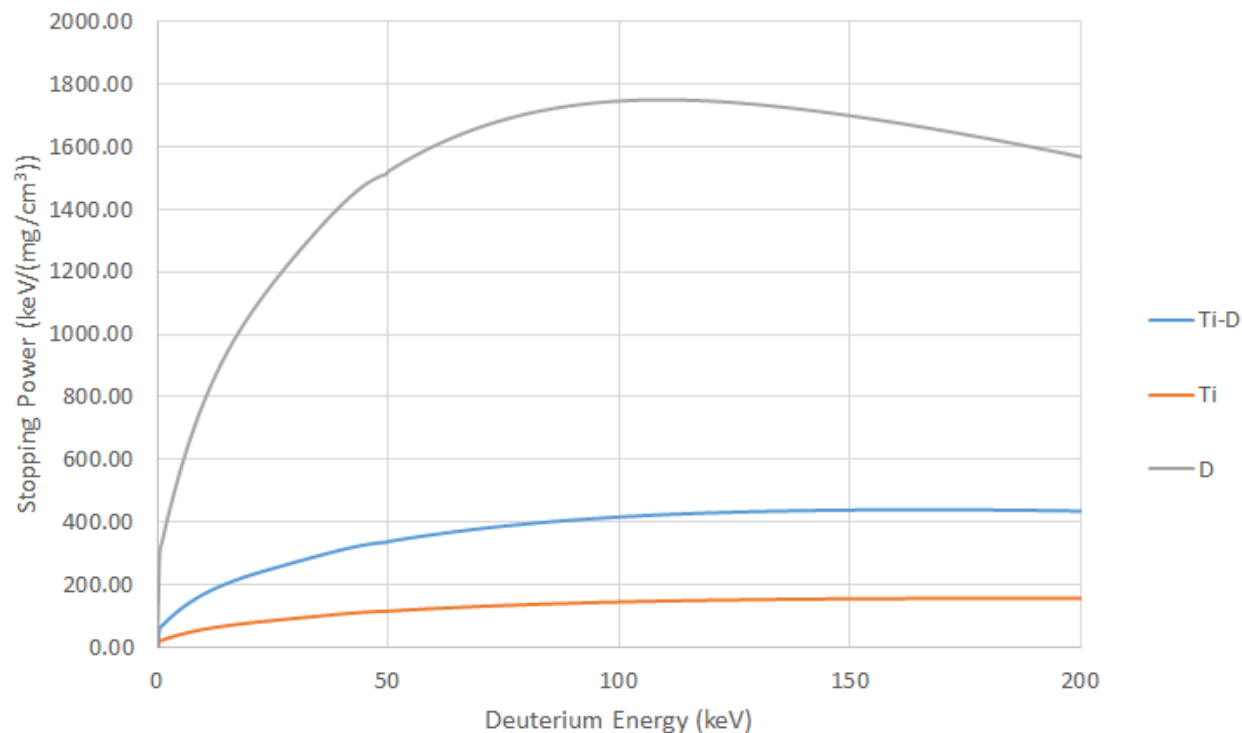


Figure 5.1: Deuterated target stopping power for deuteron ions for target with D/Ti loading ratio of 1

generator.

Another factor that affects the neutron flux is the atomic species makeup of the ionized deuterium in the beam. In the ion source, three allotropes of deuterium can exist: monatomic (D^+), diatomic (D_2^+), and triatomic (D_3^+). D_2^+ is the stable allotrope, and monatomic D can exist in the source due to breakup of D_2^+ . As shown in Ref. [29], D_3^+ can be created in low pressure ion sources by the following reaction:



The existence of D_2^+ and D_3^+ lowers the flux for a given deuteron beam current. This is due to the energy per deuteron for D_2^+ and D_3^+ are one half and one third of the energy of a D^+ , respectively. At 100 kV for example, the cross section for a 100 keV deuteron is approximately 3.5 times larger than that at 50 keV, so the total cross section of two 50 keV deuterons is less than two-thirds the value of a single 100 keV deuteron. Experimental measurements of the ion species fractions within the same type of multi-cusp ion source used by the HFNG is shown in Fig. 5.2 for hydrogen. Currently there are no measurements for the atomic species using deuterium in the HFNG multi-cusp ion source. For the current calculations, the hydrogen data will be used (and here-in referred to as deuterium atomic species). Operation of the HFNG multi-cusp ion source is normally near 1200 W, resulting

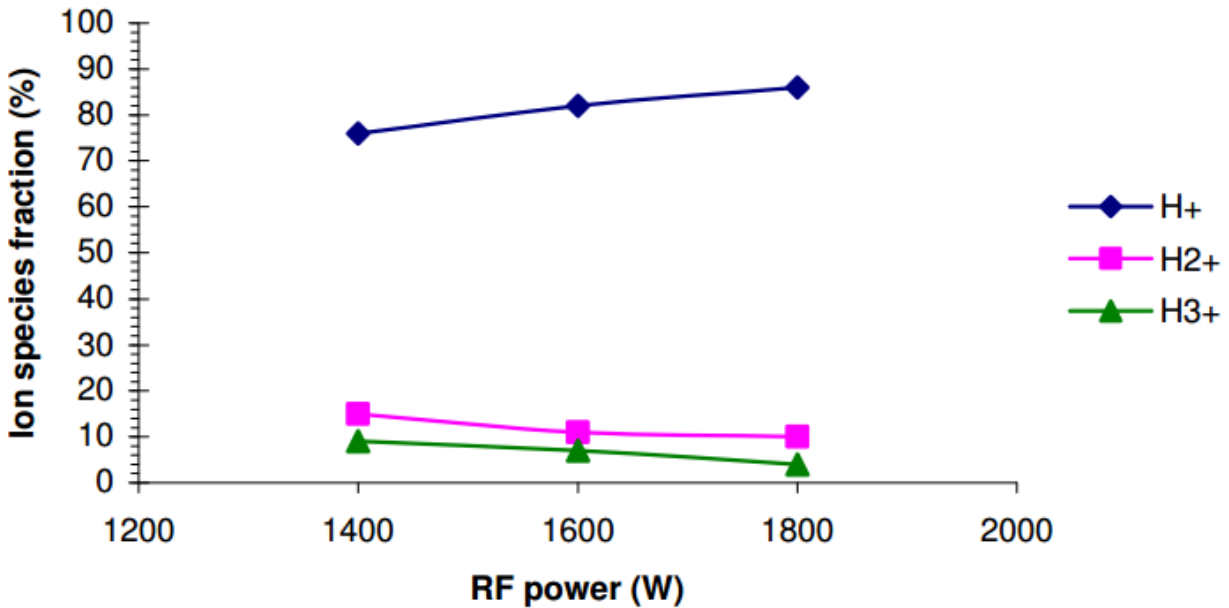


Figure 5.2: Ion species in multi-cusp ion source (Ref. [30])

in approximately 65% D⁺, 25% D₂⁺, and 10% D₃⁺. Higher powers result in a larger fraction of D⁺, but require more cooling of the multi-cusp ion source to insure the magnets within do not surpass the Curie temperature.

A Matlab flux calculation code, attached in Appendix C, calculates the predicted flux within the target slot at 100 keV and a given current for the HFNG. The code takes an input of a current density map at the target surface (provided by a Comsol beam optics simulation similar to Fig. 4.2b) that is divided into a grid with n by n elements. A secondary grid of the same dimensions as the target current density grid is created in the target slot at a distance of 8.38 mm normal to the current density grid. The solid angles between the centers of the current density and sample slot grid elements are then calculated. The target is divided into 9 layers, in which an average energy is assumed per layer (20, 30, 40... 100 keV). The thickness of each layer is determined through the use of stopping power data shown in Fig. 5.1. The target deuterium loading is 1:1 D/Ti, and the deuterium species ratio is 65% D⁺, 25% D₂⁺, and 10% D₃⁺. The angle between the center of each grid element between the target slot grid and the current density grid is determined, and a corresponding angular differential cross section from Ref. [2] based on that angle is assigned to the element. The angular differential cross section is multiplied by the corresponding solid angle to determine the total cross section. The reaction rate equation, equation 1.4, is then used to determine the reaction rate in each layer of the target for each grid node. The final step takes the summation of the reaction rates due to each layer per node to give the total reactions per element.

Since the mean free path of a 2.45 MeV neutron in Cu is 3.7 cm, and for water it is

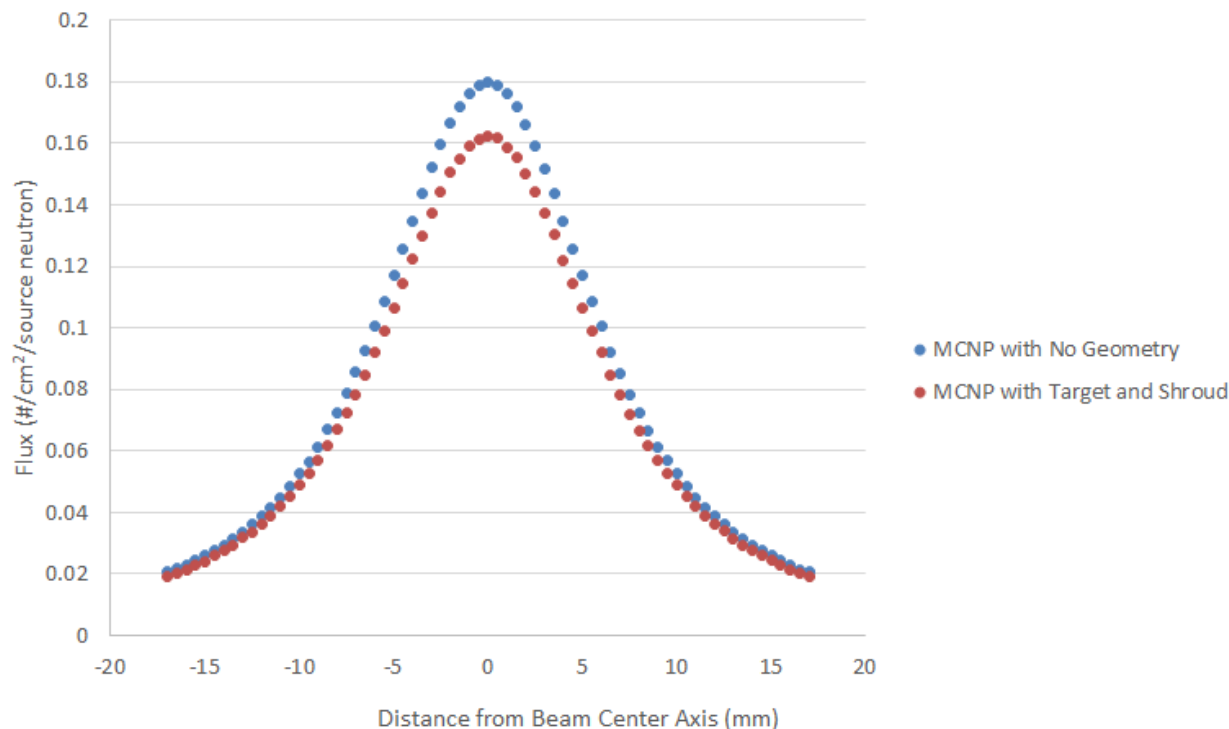


Figure 5.3: MCNP simulation of neutron flux along center-line of target slot as a distance of 8.38 mm away from target surface.

4.96 cm, and the minimum distance through the target is about 0.62 cm, attenuation of the target should be taken into account to improve the accuracy of the simulation. To correct for attenuation, a second neutron flux code, created by Joseph Bauer (LLNL), was created using the Monte Carlo N-Particle (MCNP, see Ref. [31]) code package. The simulation includes the copper target with water channels, as well as the surrounding electrostatic shroud. A uniform disk neutron source is placed at the target surface, and the flux distribution from the source follows fits at 100 kV provided by the CRC handbook (Ref. [3]). The differences between the Matlab code and the MCNP code are shown in Table 5.1. Fig. 5.3 displays the results of the MCNP simulation with and without the target and shroud (geometry) included. It can be seen that the target attenuation reduces the flux across the target slot, with a maximum attenuation of approximately 11% at the center of the beam. To correct for attenuation in the Matlab code, the MCNP code attenuation percentages are used as an estimation.

The neutron flux distribution within the target slot is an important parameter for many experiments. To determine the accuracy of the flux prediction code created for the HFNG, two types of experiments were implemented, one to determine the flux profile shape across the target using CR-39 (section 5.2), and another using activation techniques with indium foils to further verify the CR-39 results and to determine the actual flux (section 5.3). To

Table 5.1: Differences in Matlab and MCNP codes

	Matlab	MCNP
Flux distribution	Differential cross sections from 20 to 100 keV from Ref [2]	Angular correlation fit for 100 keV from Ref. [3]
Neutron source characteristics	Calculates neutron flux using: Comsol deuterium current density Implantation depths and deuteron energies Deuterium species fractions	Does not solve total flux Solves neutron distribution per source neutron Must know total number of reactions to calculate flux
Attenuation characteristics	No direct attenuation solving Uses attenuation results from MCNP code	Includes HFNG copper target, water channels, and shroud

calculate the predicted total flux of the HFNG, cross sections from ENDFVII (Ref. [32]) are used in a similar program to the Matlab code, replacing angular differential cross sections and the need to calculate solid angles. The calculated results for different deuterium atomic species ratios are shown in Fig. 5.4. It can be seen that as the accelerating voltage increases, the neutron flux increases more than linearly up to 200 kV. As previously mentioned, this is due to the increase in cross section as well as the increase in implantation depth into the target. At 200 kV, the calculated reaction rate is approximately 5 times larger than that at 100 kV. Also, the atomic species fraction plays an important role in the total flux. The total flux with 100% D+ is approximately 20% larger at 100 kV than that of a 75% to 25% D+ to D_2^+ mixture.

Figure 5.5 shows the calculated number of neutron producing D-D reactions that create

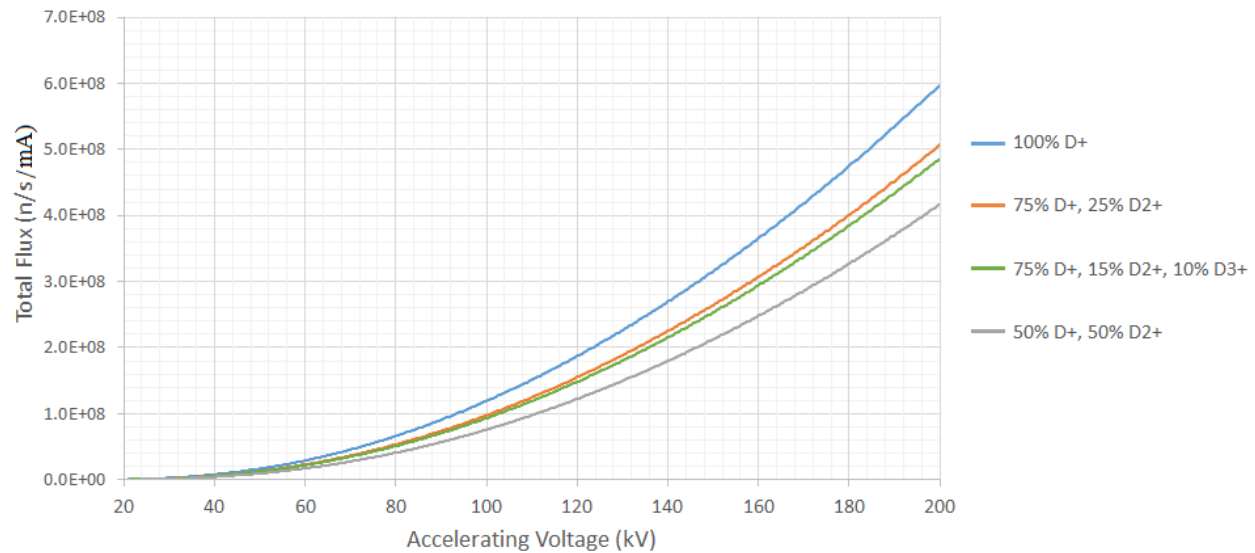


Figure 5.4: Total calculated flux for various atomic species fractions

neutrons intercepting a 3.5 X 3.5 cm sample centered at a distance of 8.4 mm normal to the target surface in the sample slot holder of the HFNG. Reactions near the surface occur at a higher energy, therefore a higher cross section resulting in more reactions. As seen in Fig. 1.3, higher energy reactions produce a neutron distribution that favors 0° . The inclusion of lower energy reactions causes the neutron spectrum to become more isotropic. The inclusion of lower energy reactions is a key difference between the Matlab and MCNP generated codes used in the analysis of the HFNG.

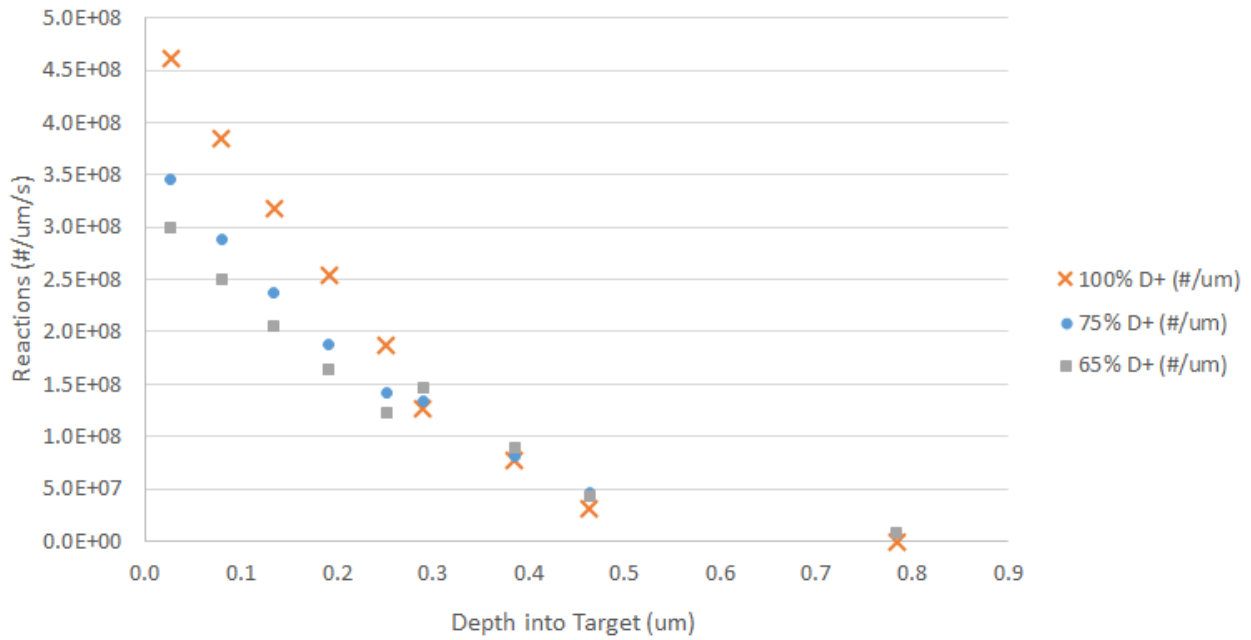


Figure 5.5: Total calculated flux for various atomic species fractions

5.2 CR-39 Measurements of Flux Distribution in Target Slot

CR-39 is a hydrocarbon solid-state track detector that is commonly used in neutron dosimetry. When neutrons elastically scatter with a proton, the resulting recoil proton leaves a damage track. These tracks can be visually seen upon chemical etching of the CR-39 with a basic solution, such as NaOH. The size of the resulting etch pits can be used to approximate the energy of the recoiling proton. The angle of the proton recoil can also be determined by measuring the elliptical pit. A more oblong elliptical pit is the result of a larger recoil angle (Ref. [33]).

A cutaway of the the CR39 experimental setup for the HFNG is shown in Fig. 5.6. The CR-39 detectors used were manufactured by Intercast, an Italian company. The CR-39 detector, with a 2×3 cm scan region, is placed 8.38 mm away with respect to the surface of the target. Neutrons created by the D-D fusion reactions occurring at the surface of the target then must travel through the target to possibly interact with the CR-39 detector. Post irradiation, a scanning system, called Politrack, then scans the CR-39 to determine the track density (See Ref. [34],[35], and [36]). The system can also deduce the angle of the hydrogen recoil by measuring the elliptical pit. Over irradiation of the CR-39 results in overlapping tracks, which cannot be read accurately using the Politrack scanning system. This results in limiting the irradiation time to less than 1 minute for a neutron flux of 1×10^8 with the detector located approximately 8.4 mm away from the target surface.

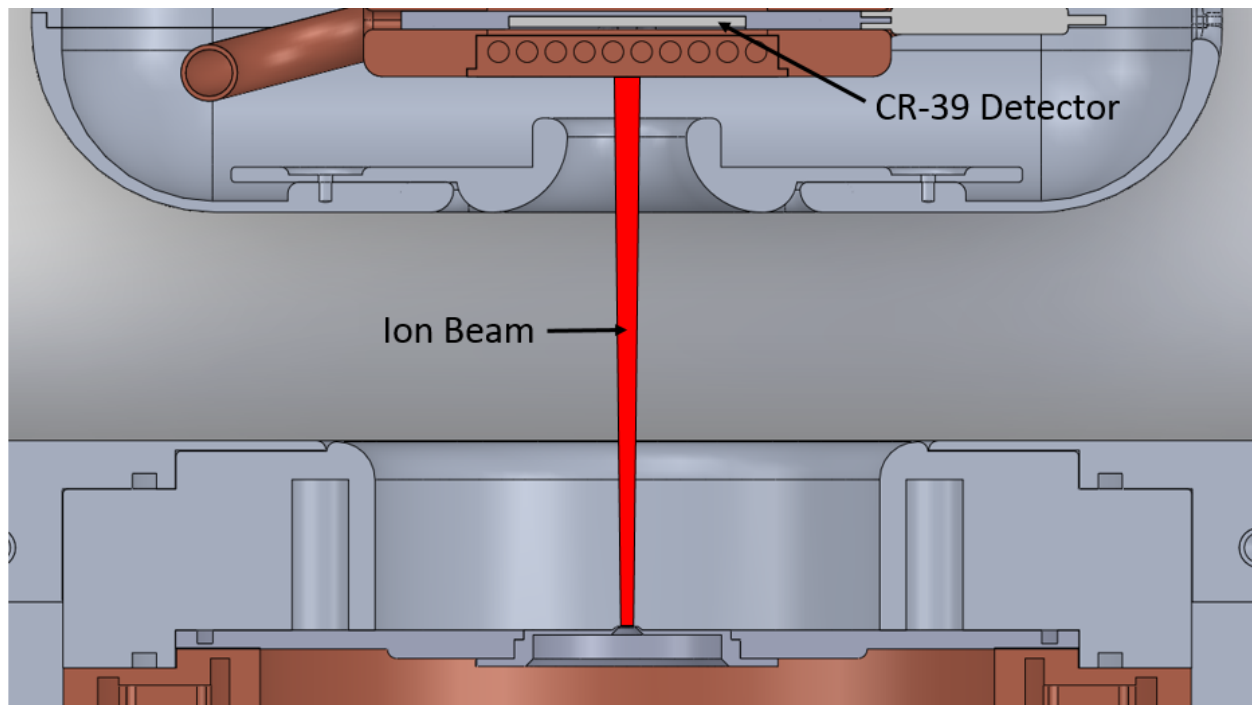


Figure 5.6: HFNG cross section showing CR-39 placement

Fig. 5.7 shows the predicted neutron flux and maximum energy maps in the target sample slot for a 100 keV, 1.33 mA beam derived from the Matlab flux calculation code described in section 5.1, prior to corrections due to target attenuation. The maximum flux at the center is 2.07×10^7 n/cm²/s, and the maximum neutron energy is 2.80 MeV. Due to the HFNG target actively loading during the short 45 second irradiation times and not being at a steady state flux, a direct comparison of flux values from the CR-39 compared to predicted results cannot be made. Instead, a comparison of the flux distribution profile will be made by normalizing the predicted counts per cell by a constant N. Figure 5.8 shows the horizontal flux profile across the beam center of the CR-39 detector compared to the calculated results from both the Matlab code and the MCNP simulation. The vertical error bars are statistical errors. The results of the MCNP and Matlab codes are approximately the same. The corresponding chi-square calculated probabilities are shown in Table 5.2. The normalized MCNP and Matlab results match well. With the P-value being much larger than the standard significance level of 0.05 for both the MCNP, it is determined that the observed experimental results do not differ significantly from that of the expected calculated results.

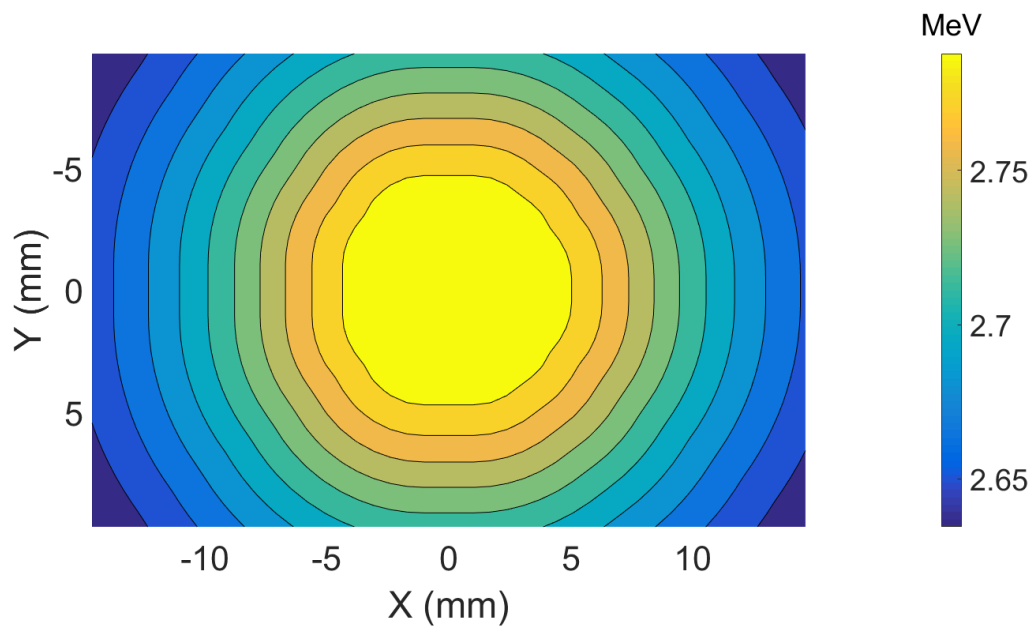
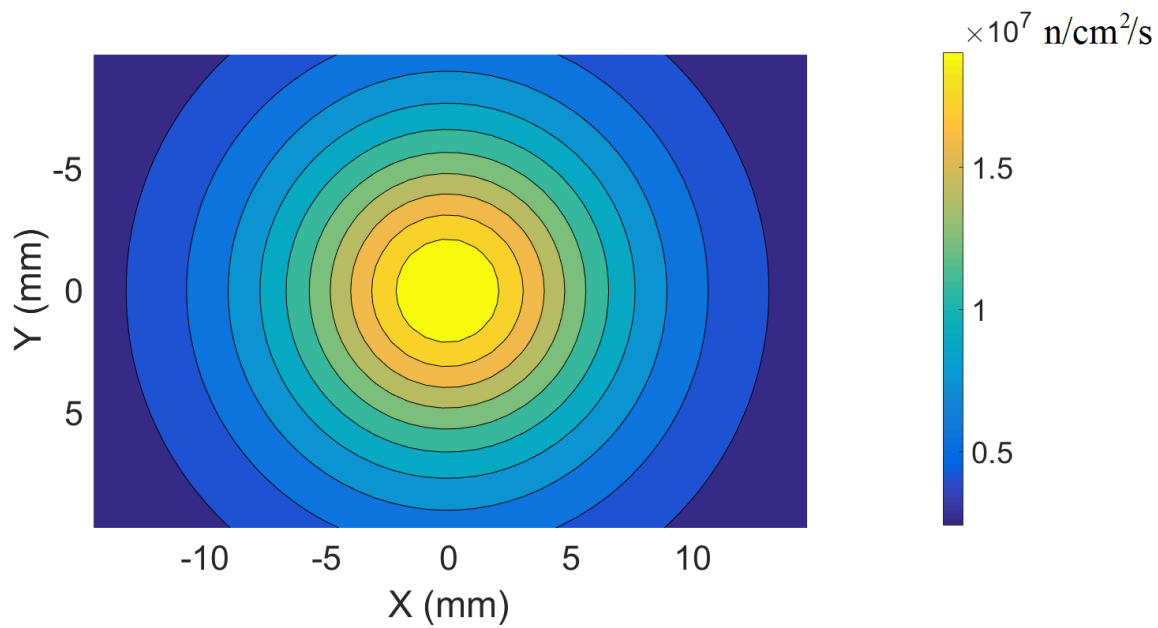


Figure 5.7: 100 kV, 1.33 mA predicted flux and maximum neutron energy maps in HFNG target slot

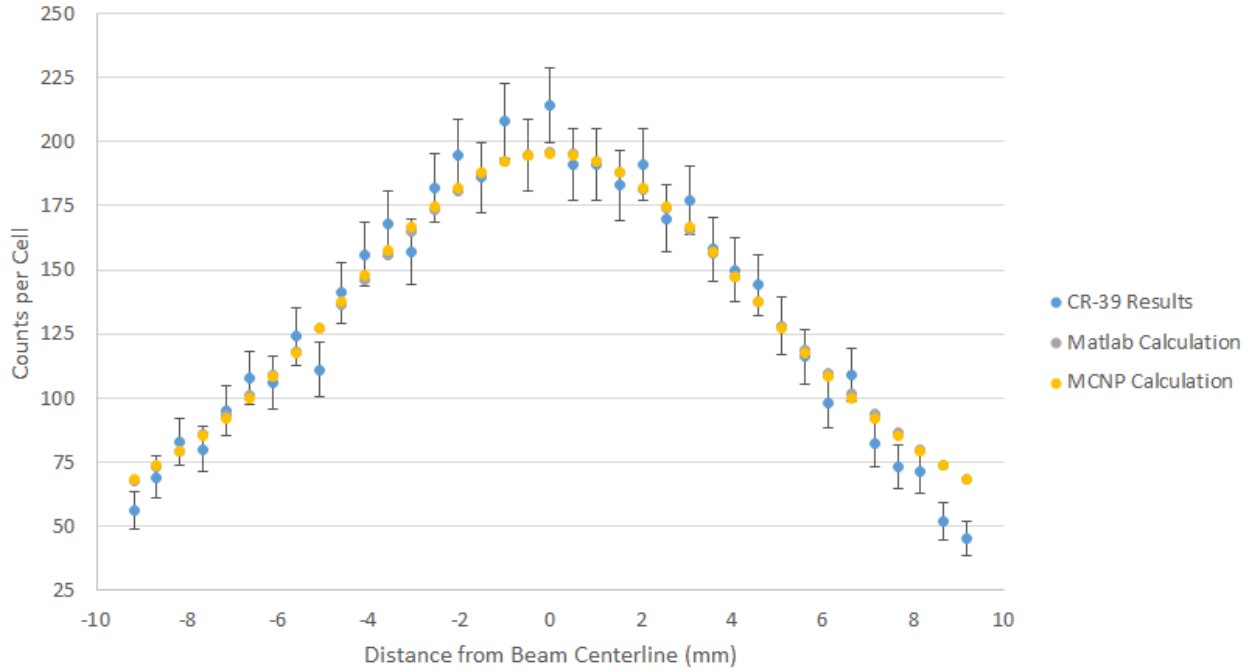


Figure 5.8: CR-39 detector counts vs. normalized predicted results

Table 5.2: Percent Difference Compared to Experimental Results

Calculation	Degrees of Freedom	Chi-Square Critical Value	Probability $p(X^2 > C.V)$
Matlab	36	35.3	99.50
MCNP	36	33.95	99.67

5.3 Indium Foil Fast Flux Measurements

To validate the flux estimations, experimental flux measurements were taken by neutron activation analysis of indium foils. Indium consists of two naturally occurring isotopes, ^{113}In and ^{115}In , with abundances of 4.3% and 95.7%, respectively. ^{115}In has two useful reactions for calculating flux:



Reaction 5.2 has a high cross section for fast neutrons, while reaction 5.3 has a larger thermal cross section. ^{115m}In decays with a half life of 4.486 hours giving off a 336.2 keV gamma ray with a branching ratio of 45.8% (Ref. [37]). The cross sections from ENDF database (Ref. [38]) for reaction 5.2 is shown in Fig. 5.9. Below 3 MeV, the cross section has a peak value of 0.346 barns at 2.7 MeV.

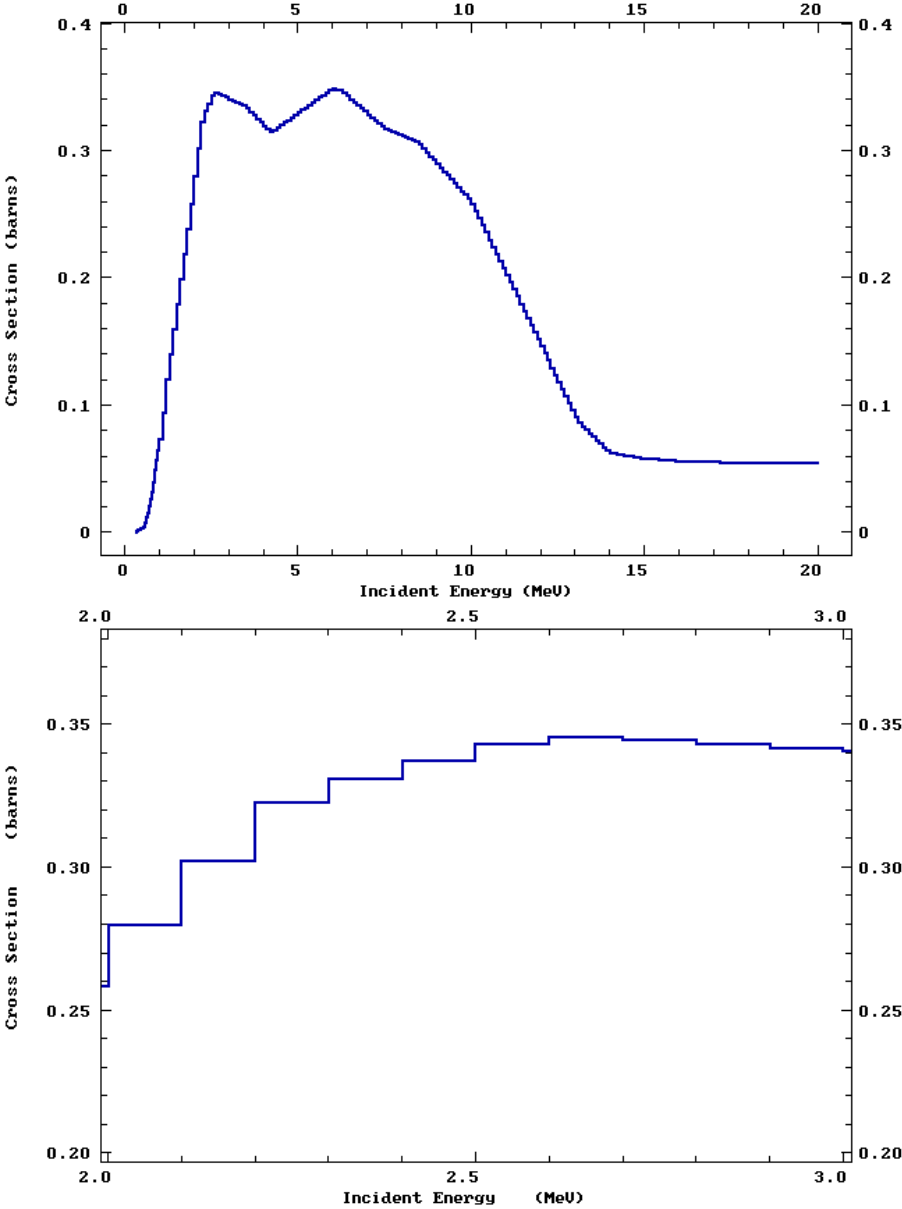


Figure 5.9: $^{115}\text{In}(n,n')^{115m}\text{In}$ experimental cross section values from ENDF database. Lower graph depicts the region between 2-3 MeV.

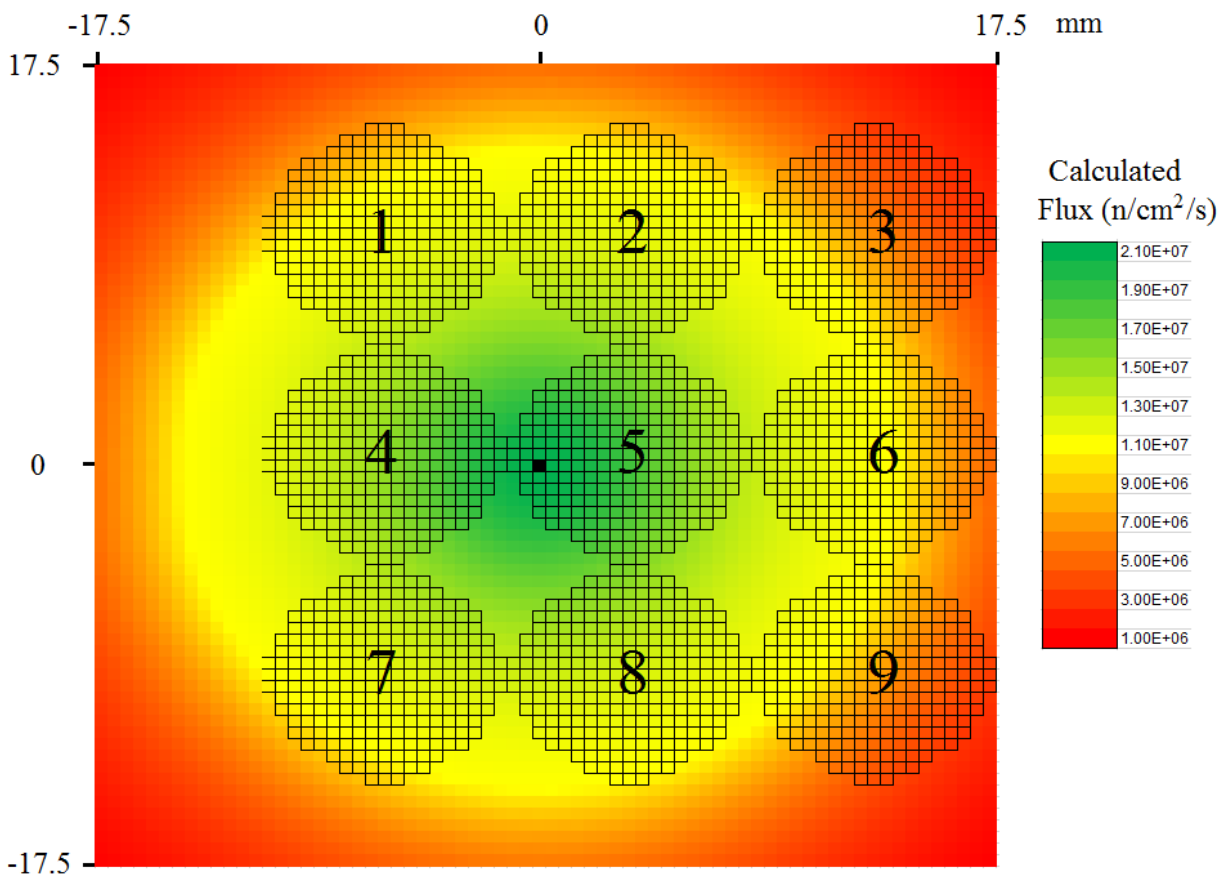


Figure 5.10: Foil locations compared to beam center. Flux map is Matlab predicted flux with 65% D+, 25% D₂⁺, and 10% D₃⁺ atomic ratio

Nine indium foils were placed in the HFNG sample slot arranged in a 3 X 3 array for irradiation. The experimental setup is the same as shown in Fig. 5.6 with the CR-39 replaced with the indium foil array, which is located about 8.9 mm away from the target surface. The centers of the foils were approximately 1 cm apart, and each foil was approximately 0.9 cm in diameter. The central indium foil of the array was aligned with the center of the target. The location of the foils relative to the center of the beam was determined post irradiation by measuring the location of the center of the burn mark left by the deuterium beam. The locations of the foils relative to ion beam can be seen in Fig. 5.10. The center foil was located 0.5 mm above and 3.7 mm to the right relative to the center of where the deuterium ion beam strikes the surface of the target. The experimental data was taken with a 100 keV, 1.43 mA deuterium beam.

The predicted flux using the Matlab code with target neutron attenuation is also shown in Fig. 5.10 with a 65% D+, 25% D₂⁺, and 10% D₃⁺ deuterium atomic ratio. The maximum flux, which is at the location closest to the center of the ion beam, is 1.93×10^7 n/cm²/s.

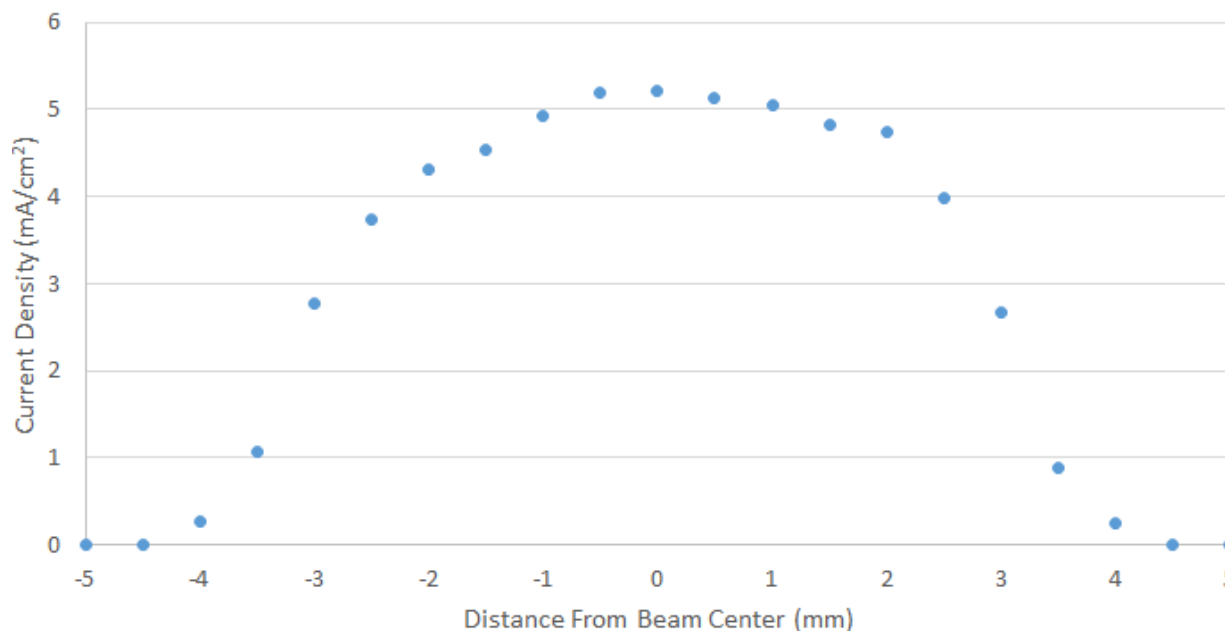


Figure 5.11: Comsol simulated current density at target for 1.43 mA, 100 kV deuterium beam

A center lineout of the Comsol simulated current beam density at 100 keV and 1.43 mA used to determine the flux map is shown in Fig. 5.11. Due to the indium foils being located at various angles relative to the beam axis, the neutron energy spectrum in each foil is different, as previously discussed in Chapter 1 and shown in Fig. 1.2. Attenuation caused by the target creates lower energy down scattered neutrons and also reduces the number of neutron reaching the foils. The foils that are off-center present a greater thickness to the neutron beam. These effects are in "opposite directions" with the former decreasing the activation and the latter increasing it. To compare the calculated results to the experimental results, the track-length flux is calculated. This corrects for neutrons entering the foils at angles. Since the foils are thin, an infinitesimally thin surface approximation is used, where the area of the surface becomes the normal surface area multiplied by the absolute value of the cosine of the angle between the surface normal and the particle trajectory. Knowledge of the energy spectrum of each foil is important in determining the inelastic cross section. Using the MCNP code, the energy distribution of each foil was determined using the thick target neutron energy spectrum at 100 keV and is shown in Fig. 5.12.

The indium foils were irradiated in the HFNG for 3 hours and 40 minutes and then removed from the neutron generator and placed in front of a germanium detector for gamma ray counting. The foils were counted one at a time and the experimental data, such as gamma ray counts and counting times, can be seen in Appendix E. To calculate the experimental flux, the cross section adjusted for the given neutron energy spectrum must be determined. Reference [39] provides details of unfolding the neutron energy spectrum from

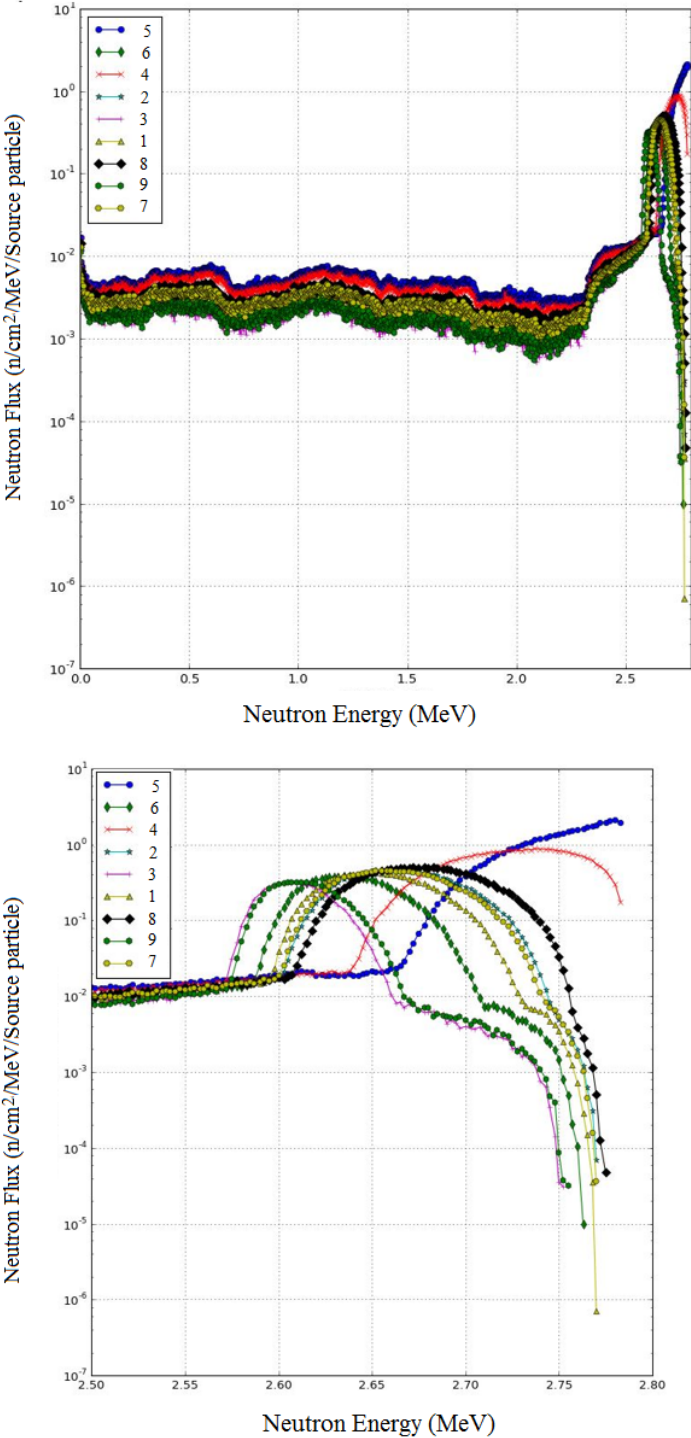


Figure 5.12: MCNP calculation of neutron energy spectrum in each foil. Lower graph depicts the 2.5-2.8 MeV region.

a set of measured reaction rates. By splitting the energy spectrum into bins and using this formulation in reverse, the reaction rates for given energy ranges can be determined. The total reaction rate can be determined by splitting the flux spectrum into n number of groups, where each group contains neutrons within a certain energy band. The total reaction rate is then:

$$R = \sum_{i=1}^n N(F_i\phi)\sigma_i = N\phi \sum_{i=1}^n F_i\sigma_i \quad (5.4)$$

N = number of target atoms (#)

F_i = fraction of neutrons in the i^{th} energy group

ϕ = total neutron flux (n/cm²/s)

σ_i = average cross section for energy group i (cm²)

For calculation of the neutron flux, flux bins divided by energy intervals of 200 keV for each indium foil were created using the data from the MCNP results shown in Fig. 5.7 (See Appendix E for data). Using the production (reaction rate) and decay of ^{115m}In during irradiation and making corrections for decay after irradiation and during the counting of the foil, the total flux can then be determined by using equation 5.5.

$$\phi = \frac{C\lambda}{N \left[\sum_{i=1}^n F_i\sigma_i \right] \gamma \varepsilon (1 - e^{-\lambda t_{irr}}) (1 - e^{-\lambda t_c}) e^{-\lambda t_w}} \quad (5.5)$$

where

C = gamma ray counts (#)

t_{irr} = irradiation time (s)

t_w = wait time between end of irradiation and beginning of gamma counting (s)

t_c = gamma ray count time (s)

γ = gamma ray branching ratio

ε = detector absolute efficiency

λ = gama ray decay constant (s⁻¹)

Using equation 5.5, the flux for each foil was determine and is shown in Table 5.3. Predicted values using both the Matlab and MCNP code are compared to the experimental values. Since the MCNP code solves the neutron distribution per source neutron, a total neutron flux value of 1.21×10^8 was multiplied by the results. This value is the total flux determined by using the total D-D reaction cross section, as seen in Fig. 5.4, for an atomic species ratio of 65% D+, 25% D₂+, and 10% D₃+. The Matlab code calculated flux all fall within an 15% difference to that of the experimental values, with many values falling within the uncertainty of the experimental measurements. The MCNP calculated values are larger than the Matlab calculated values. This is due to the MCNP code using only the 100 keV reaction neutron distribution for all reactions. This distribution is more forward (beam direction) peaked compared to including neutrons created at lower reaction energies.

Table 5.3: Experimental vs. Calculated Flux

Foil Location	Cross Section (mb)	Experimental Flux ($\cdot 10^6$ n/cm ² /s)	Matlab 65% D+ Flux ($\cdot 10^6$ n/cm ² /s)	Matlab % Difference	MCNP 1.21 $\cdot 10^8$ Flux ($\cdot 10^6$ n/cm ² /s)	MCNP % Difference
1	306.5	4.57 \pm 0.28	4.20	-8.7	4.72	3.2
2	309.8	4.70 \pm 0.31	4.81	2.4	5.57	15.6
3	295.7	2.40 \pm 0.15	2.39	0.6	2.54	5.5
4	322.7	8.40 \pm 0.64	8.83	5.0	11.1	24.6
5	327.3	10.4 \pm 0.73	11.1	6.4	14.9	30.3
6	303.0	3.39 \pm 0.23	3.61	6.2	3.87	12.4
7	308.8	4.79 \pm 0.36	4.92	2.6	5.32	10.0
8	312.5	4.90 \pm 0.38	5.72	14.5	6.41	23.6
9	296.9	2.24 \pm 0.16	2.61	14.3	2.78	19.7

Overall, many factors affect the flux distribution of the HFNG neutron generator. The target stopping power, deuterium atomic species, and target loading ratio all play an important role in calculating the flux. The CR-39 and indium foil flux measurements matched well with the predicted flux values obtained by the Matlab code. The MCNP simulation calculates information on the target neutron attenuation, though the flux results are larger than experimental results due to the inclusion of reactions only occurring at 100 keV. Including the flux distribution due to lower energy reactions in the MCNP simulation will provide a more accurate prediction of the flux in the sample holder location.

Chapter 6

Overview of HFNG Experiments

Since the commissioning at approximately 1×10^8 n/cm²/s, experiments using the HFNG have included data collection of medical isotope cross sections, delayed gamma measurements from the fission of ²³⁸U, and electronic chip testing for single event failures due to neutron irradiation. Planned experiments for geochronology include cross section measurements of ³⁹K(n,p)³⁹Ar reaction. Geochronology experiments are planned as the HFNG is conditioned at higher fluxes.

6.1 Medical Isotope Cross Sections

As mentioned in Chapter 1, neutron induced reaction cross sections for the production of many medical isotopes, especially for (n,p) reactions, have little data. One such isotope, ⁴⁷Sc, is used in imaging. As explained in Ref. [40], ⁴⁷Sc is an attractive isotope for imaging due to its relatively long half life of 3.35 days, and its low energy beta and gamma emission. The reason why ⁴⁷Sc isn't commonly used is due to its poor availability. The use of a compact neutron generator would allow for the production of medical isotopes on site at medical facilities.

Experimental data was collected to determine the cross section of the ⁴⁷Ti(n,p)⁴⁷Sc reaction using the HFNG. Titanium has four stable isotopes, of which ⁴⁷Ti is 7.5% in naturally occurring titanium. A titanium foil was placed in the HFNG sample slot along with an indium foil. Since the activation of indium foils is well documented for fast neutrons in the range of 2-3 MeV, the ⁴⁷Ti(n,p)⁴⁷Sc cross section can be determined by the activation ratio of ⁴⁷Sc to ^{115m}In. Figure 6.1 shows the preliminary gamma ray spectrum from the experimental foil after a two hour irradiation using the HFNG. The indium and irradiated titanium foils were counted using a low energy photon spectrometer.

A similar experimental measurement of the (n,p) reaction cross section on ⁶⁴Zn and ⁶⁷Zn to create ⁶⁴Cu and ⁶⁷Cu has been explored using the HFNG. ⁶⁴Cu can be used in cancer therapy, as well as to study a rare disease called Wilson's disease. Wilson's disease is an autosomal recessive genetic disorder in which copper accumulates in tissues and can

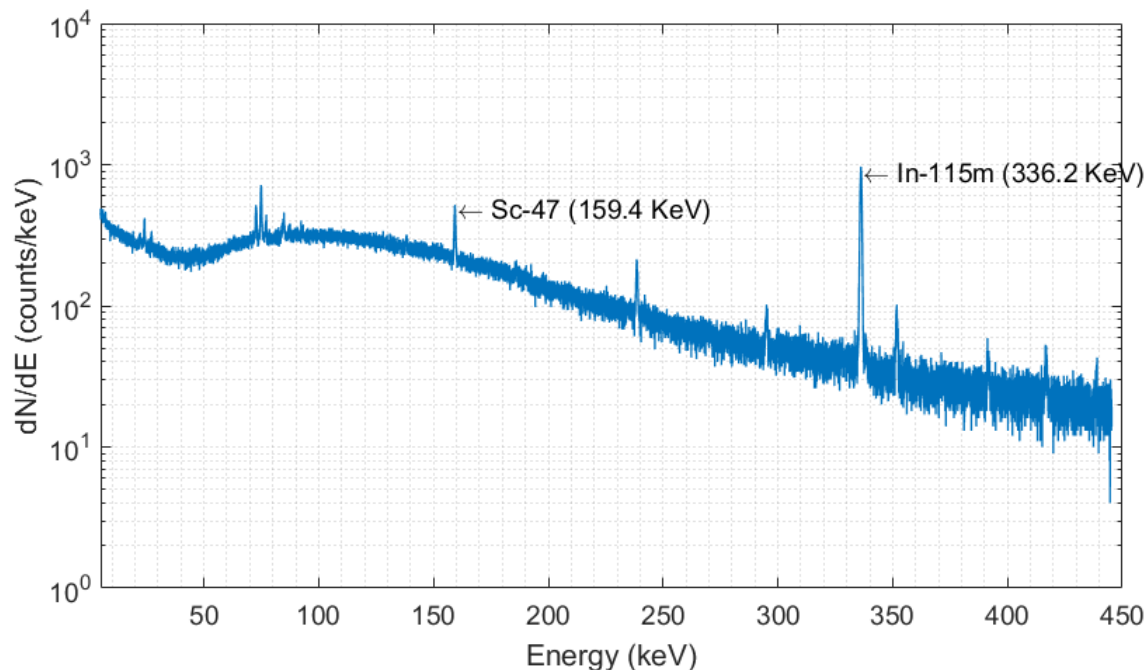


Figure 6.1: Gamma ray spectrum post irradiation of a titanium foil using the HFNG

Table 6.1: Proposed Medical Isotope (n,p) Cross Section Measurement Experiments

Target	Product
³² S	³² P
⁸⁹ Y	⁸⁹ Sr
¹⁰⁵ Pd	¹⁰⁵ Rh
¹⁴⁹ Sm	¹⁴⁹ Pm
¹⁵³ Eu	¹⁵³ Sm
¹⁵⁹ Tb	¹⁵⁹ Gd
¹⁶¹ Dy	¹⁶¹ Tb
¹⁶⁶ Er	¹⁶⁶ Ho
¹⁶⁹ Tm	¹⁶⁹ Er
¹⁷⁵ Lu	¹⁷⁵ Yb
¹⁷⁷ Hf	¹⁷⁷ Lu

eventually lead to liver disease. ⁶⁴Cu can be used to determine how the body retains copper (Ref. [41]). A campaign to measure more (n,p) cross sections at energies near 2.5 MeV are planned at the HFNG; a full list of proposed reactions can be seen in Table 6.1. These proposed cross section measurements are from a plenary lecture given at the workshop on Nuclear Data Needs and Capabilities for Applications (NDNCA) in Berkeley, California (Ref. [42]).

6.2 Geochronology

One of the main driving forces in the development of the HFNG is to create a compact neutron source to enable the $^{40}\text{Ar}/^{39}\text{Ar}$ dating technique. As discussed in chapter 1, the current approach of using fission reactor irradiation introduces systematic uncertainties due to the presence of both low and high energy neutrons which can transmute argon gas via various (n,destruction) reactions summarized in Table 1.3. In order to use a D-D neutron generator, fast neutron fluxes above 10^{10} n/cm²/s, and preferably above 10^{11} n/cm²/s, are desirable to allow for sample irradiation in a moderate time period. Current efforts are being made to increase the flux above 10^8 n/cm²/s by increasing the accelerating voltage and beam current in the generator. Beam induced arcing between the shroud and vacuum has limited progress. Developments focusing on electric field reduction as well as elimination of charge buildup in electrical insulators to reduce arcing is being explored.

As mentioned in Chapter 1, through neutron irradiation, ^{39}Ar is produced from ^{39}K through an (n,p) reaction. As long as the a sample is irradiated with another sample of known age, the ratio of $^{40}\text{Ar}/^{39}\text{Ar}$ can be used to determine the age of the unknown sample. Knowledge of the $^{39}\text{K}(n,p)^{39}\text{Ar}$ cross section is useful in determining how long to irradiate a sample. The cross section for the reaction near 2.5 MeV is not well defined. The ENDSF-VII database (Ref. [32]) gives a value of 188 mb. Other values, reported in Ref. [43], are determined to be around 80 mb. Using the HFNG, a future experiment to measure the $^{39}\text{K}(n,p)^{39}\text{Ar}$ cross section is planned. Using the same method as the medical isotope cross section measurements, a potassium bromide sample placed with an indium foil will be irradiated in the HFNG to determine the (n,p) cross section relative to the inelastic cross section from ^{115}In .

6.3 Delayed Gammas from Uranium Fission

Beta-delayed gamma rays are an important diagnostic for nuclear forensic analyses. The FIER (Fission Induced Electromagnetic Response) code developed at Lawrence Berkeley National Lab (LBNL) is a tool to model time-dependent delayed gamma-ray spectra from neutron-induced fission (Ref. [44]). To benchmark the FIER code, an experiment was performed at the HFNG to irradiate a sample of ^{238}U with 2.45 MeV neutrons. The resulting delayed gamma-ray spectrum was obtained by counting the sample using a HPGe detector, and compared to FIER simulation output. A portion of the delayed gamma ray spectrum data can be seen in Fig. 6.2. These data can also be used in conjunction with FIER to illuminate discrepancies in the input evaluated nuclear databases, including the ^{238}U fast fission yield and fission fragment nuclear structure data.

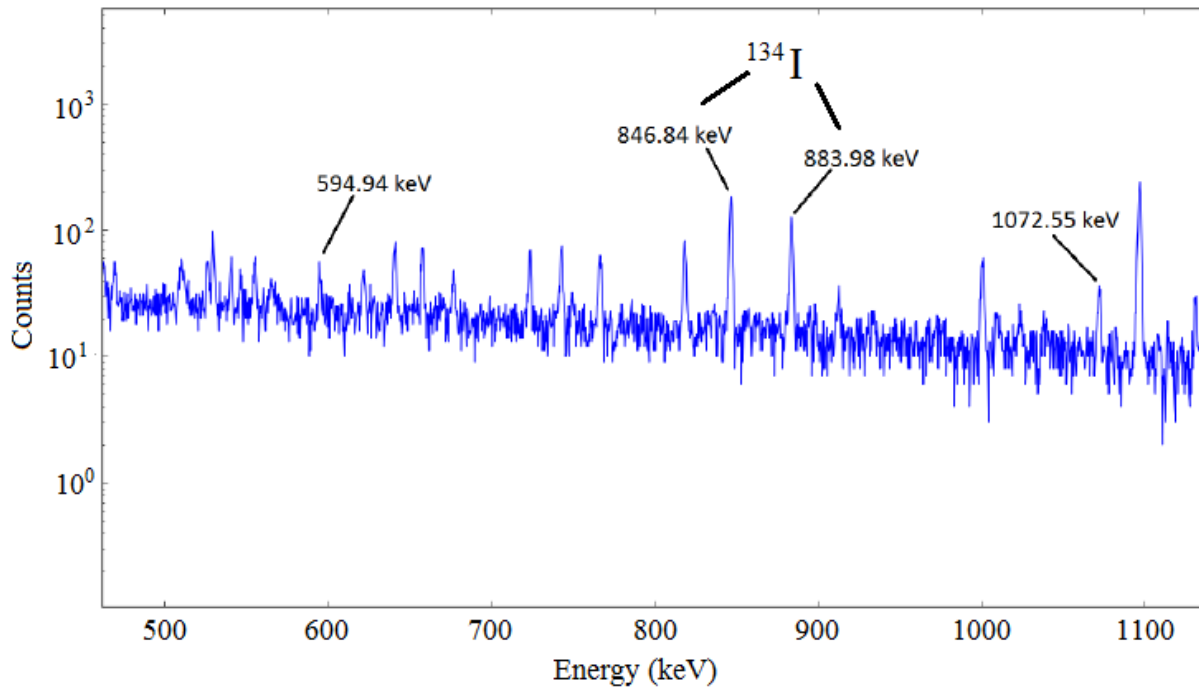
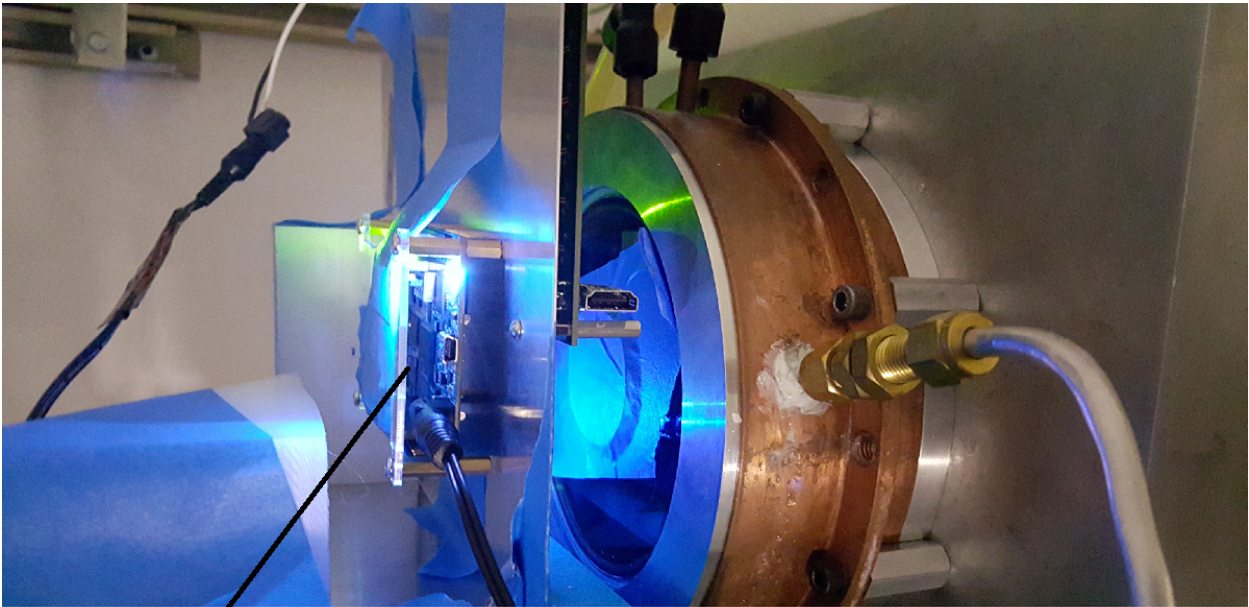


Figure 6.2: Delayed gamma spectrum from the fission of ^{238}U using the HFNG. Measured lifetimes of the 847 and 884 keV gamma decays were confirmed with that of ^{134}I .

6.4 Single Event Upset of CPUs

Radiation can create single event upsets (SEU's) in electronic semiconductor chips that can flip or reverse the data state in a memory cell. The creation of radiation hardened electronic components is important in applications in outer space and high altitude flights, as well as near particle accelerators and nuclear reactors. Ionizing radiation, or an event that causes ionizing radiation, is the cause of a SEU. High energy cosmic rays are a significant source of SEU's. High energy cosmic rays interact with the atmosphere creating a cascade of secondary particles. Of these secondary particles, neutrons are the most likely to cause upsets in devices at terrestrial altitudes (Ref. [45]). Neutrons themselves are not ionizing, but can cause elastic and inelastic scattering within a semiconductor, in which the scattered particle in return can cause an ionizing damage track resulting in a possible SEU.

Preliminary tests by researchers from LBNL have shown the feasibility of using the HFNG to qualify radiation hardened electronics at energies of about 2.5 MeV and below. An electronics processor board was irradiated outside the vacuum chamber near one of the HFNG ion sources for irradiation as shown in Fig.6.3 (the opposite ion source was used for the irradiation). After an hour irradiation, the processor chip received a fluence of over 10^8 n/cm² with no SEU's. Future experiments at higher neutron fluxes will allow for larger fluences in a shorter irradiation time.



CPU Board

Figure 6.3: Experimental setup of SEU testing of electronic components

Chapter 7

Conclusions and Future Work

7.1 Conclusions

The HFNG was commissioned at a flux of 1×10^8 neutrons/sec. During commissioning, characterizing of the HFNG's operating parameters was essential for characterizing the stability of the machine, as well as for determining the neutron flux for irradiation experiments. Characteristics that effect the operational stability of the HFNG include the suppression of the target-emitted back streaming electrons, target sputtering and cooling, and ion beam optics. Understanding these parameters are necessary to determine the possible neutron flux distribution and total output of the HFNG.

Two main methods of electron suppression were tested: using permanent magnets to bend electrons back to the target, and implementing an electrostatic shroud creating a suppressing electric field. Simulations of the permanent magnet design showed that even with magnetic fields surpassing 1000 gauss, electrons would migrate along the target due to the $E \times B$ force without coming into contact with the surface. When electrons would reach an area of lower magnetic field they would escape the target area and collide with the vacuum chamber wall. Experimental tests confirmed the electrons were colliding with the vacuum chamber wall exactly in the location shown by the simulation. Simulations of an electrostatic shroud showed full suppression of electrons emitted from the target surface. For the chosen shroud geometry, a voltage differential of -400 V or greater compared to the target resulted in successful electron suppression. Experimental results with the addition of a shroud reduced the back streaming electrons significantly to undetectable levels. Furthermore, the dose due to bremsstrahlung x-rays was reduced by a factor of more than 20. Analysis of both suppression techniques resulted in the conclusion that the use of electric fields for electron suppression is more effective due to the fact that electric fields add energy to the electron while a magnetic field can only change its direction.

Two different target styles were analyzed and tested. One target had angled surfaces to reduce the beam heat flux and a titanium layer sputter coated on the surface. The second target was flat to provide a more uniform flux and had an explosion bonded titanium layer.

Using a Stopping Range of Ions in Matter (SRIM) simulation it was shown that the flat target would retain its titanium layer over 11 times longer than the angled target.

The final design of the HFNG created an acceleration column with a focusing electric field. To defocus the ion beam and keep target temperatures below 400 °C, a convex nozzle extraction plate was designed. To calculate the target temperatures, a finite difference method solver incorporating the additional heat removal effects of subcooled boiling was developed. Validation of the energy balance results from the finite difference method calculations showed the iterative solver converged to heat removal results within about 3% of the expected value. Direct temperature measurements of the target is difficult due to the target being at a -100 kV potential and it's proximity to the RF ion source. Testing of the extraction nozzle at 1.43 mA and 100 kV determined that overheating of the target did not occur as the measured neutron flux of the generator was near predicted values. Measurement of the heat spot left on the target showed a beam diameter of approximately 5.3 mm, which is close to the simulated 5.1 mm beam diameter. With the successful implementation of an extraction nozzle, future neutron generators can be more compact if desired. This is due to the ability to make the acceleration column narrower and then defocus the beam with a nozzle geometry.

Many factors affect the flux distribution of the HFNG neutron generator, and a detailed analysis to understand these factors effects was completed. The target stopping power, deuterium atomic species, and target loading ratio all play an important role in calculating the flux. Two different models were developed to predict the neutron flux distribution within the target sample slot of the HFNG. The Matlab model used flux distribution data from Ref. [2] and incorporated the energy dependence of the distribution, the beam current density distribution determined by Comsol, and the atomic deuteron species makeup of the beam. The second model was developed using MCNP and included the neutron distribution at 100 kV, as well as effects due to target attenuation. CR-39 detector measurements matched the flux distributions calculated by both the Matlab and MCNP models with over a 99% chi-square probability. The indium foil flux measurements matched with the predicted total flux values obtained by the Matlab code, with residual errors between the foil flux and calculated values being less than 15%. The MCNP simulation resulted in flux results are larger than experimental results due to the inclusion of reactions only occurring at 100 keV. This result shows that the reaction is not just a surface effect, but that the stopping power and imbedded depth plays an important role in determining the neutron flux.

7.2 Future Work

Increasing the neutron flux will allow the HFNG to be used for a broader range of experiments. Current analysis of higher fluxes has been completed, and an extraction nozzle for 10 mA and 125 kV has been fabricated to help spread the beam and reduce the heat flux. Temperature calculations show that the addition of the nozzle is necessary at these parameters, as with a flat extraction the target surface temperatures will be near 400°C and

the heat flux at the central cooling channel walls surpass the critical heat flux. The nozzle reduces the temperatures across the surface by about 50°C with a critical heat flux ratio of 0.86.

In order to increase the flux, beam induced arcing between the shroud and the vacuum chamber must be reduced. Investigation in insulator charge build-up, as well as electrical flash-over of insulators should be explored. This may include looking at thin conductive coatings, or into the use of anti-static plastics. Further experimental measurements and analysis of the fast to thermal flux ratio will be beneficial as well. Experimental measurements of the $^{39}\text{K}(n,p)^{39}\text{Ar}$ cross section at approximately 2.5 MeV is important for using the $^{40}\text{Ar}/^{39}\text{Ar}$ dating technique.

Bibliography

- [1] Kenneth Krane. *Introductory to Nuclear Physics*. New York: Wiley, 1988.
- [2] Horst Liskien and Arno Paulsen. “Neutron Production Cross Sections and Energies for the Reactions $T(p,n)^3\text{He}$, $D(d,n)^3\text{He}$, AND $T(d,n)^4\text{He}$ ”. *Nuclear Data Tables* 11 (1973), pp. 569–619.
- [3] Julius Csikai. *CRC Handbook of Fast Neutron Generators*. Boca Raton: CRC.
- [4] K. Kudo et al. “Production of a Reference Monoenergetic Neutron Field using $D(d,n)^3\text{He}$ Reaction”. *Nuclear Data Science and Technology: Proceedings of an International Conference, 13-17 May 1991*. Springer Science and Media, 2012, pp. 533–535.
- [5] National Research Council. *Radiation Source Use and Replacement: Abbreviated Version*. Washington, D.C.: National Academies.
- [6] Richard R. Pemper et al. “The Direct Measurement of Carbon in Wells Containing Oil and Natural Gas Using a Pulsed Neutron Mineralogy Tool”. SPE Annual Technical Conference and Exhibition. 2009.
- [7] A.H. Youmans et al. “Neutron Lifetime, a New Nuclear Log”. *J Petrol Technol* 16 (1964), pp. 319–328.
- [8] Thomas Ruth. “Accelerating Production of Medical Isotopes”. *Nature* 457 (2009), pp. 536–537.
- [9] K. Pagdon et al. “Production of Tc-99m from Naturally Occurring Molybdenum Absent Uranium”. IEEE/NPSS 24th Symposium on Fusion Engineering. 2011.
- [10] Paul R. Renne et al. “Application of Deuterondeuteron (DD) Fusion Neutrons to $40\text{Ar}/39\text{Ar}$ Geochronology”. *Appl Radiat Isotopes* 62 (2005), pp. 25–32.
- [11] H. Leutz, G. Schulz, and H. Wenninger. “The Decay of Potassium-40”. *Zeitschrift fur Physik Z. Physik* 187 (1965), pp. 151–164.
- [12] Q. Ji, A. Sy, and J.W. Kwan. “Radio frequency-driven proton source with a back-streaming electron dump”. *Rev Sci Instrum* 81 (2010).
- [13] Stanley Humphries. *Charged Particle Beams*. New York: Wiley, 1990.
- [14] L.N. Large and W. S. Whitlock. “Secondary Electron Emission from Clean Metal Surfaces Bombarded by Fast Hydrogen Atoms”. *Proc Phys Soc* 79 (1962), pp. 148–157.

- [15] Manfred Kaminsky. *Atomic and Ionic Impact Phenomena on Metal Surfaces*. New York: Academic, 1965.
- [16] *AC/DC Module User Guide for Comsol Multi-physics*. Comsol Multi-physics. May 2013.
- [17] A.J. Durand and A.M. Shroff. “High Voltage Breakdown in the Electron Gun of Linear Microwave Tubes”. *High Voltage Vacuum Insulation (R.V. Latham ed.)* (1995), pp. 403–429.
- [18] J. F. Ziegler and J. P. Biersack. *SRIM, the Stopping and Range of Ions in Matter*. SRIM Co., 2008.
- [19] Virgil L. Stout and Martin D. Gibbons. “Gettering of Gas by Titanium”. *J Appl Phys* 26 (1955).
- [20] Van P. Carey. *Liquid-Vapor Phase-Change Phenomena*. New York: Taylor and Francis, 2008.
- [21] C. Y. Ho R. W. Powell and P. E. Liley. “Thermal Conductivity of Selected Materials”. *NSRDS* (1966), pp. 22, 109.
- [22] *Thermophysical Properties of Fluid Systems*. NIST Database, Data retrieved Jan. 2016.
- [23] *Electron Beam Divergence: Instruction Manual*. Comsol Multi-physics. May 2013.
- [24] Wagnet L. Araujo and Tarcisio Passos Ribeiro de Campos. “Design and Investigations of a DD Compact Neutron Generator in Head Radiotherapy”. *International Nuclear Atlantic Conference Proceedings*. 2013.
- [25] D.I. Thwaites. “Bragg’s Rule of Stopping Power Additivity: A Compilation and Summary of Results”. *Radiat Res* 95 (1983), pp. 495–518.
- [26] J. Reijonen. “Neutron generators developed at LBNL for homeland security and imaging applications”. *CAARI Proceedings*. 2007.
- [27] P. Tayyebi and F. Abbasi Davani. “Design and Construction of Deuterium Target for Fast neutron Production”. *IEEE NPSS Toronto Proceedings*. 2010.
- [28] J. H. Vainionpaa et al. “Technology and applications of neutron generators developed by Adelphi Technology, Inc”. *Physics Procedia* 60 (2014), pp. 203–211.
- [29] H. Figger, W. Ketterle, and H. Walther. “Spectroscopy of triatomic hydrogen”. *Zeitschrift fr Physik* 13 (2 1989), pp. 129–137.
- [30] S. K. Hahto et al. “Multicusp ion source with external RF antenna for production of protons”. *Rev Sci Instrum* 75 (2 2004), pp. 355–359.
- [31] X-5 Monte Carlo Team. *MCNP - Version 5, Vol. I: Overview and Theory*. LA-UR-03-1987, 2003.
- [32] M.B. Chadwick et al. “ENDF/B-VII.1: Nuclear Data for Science and Technology: Cross Sections, Covariances, Fission Product Yields and Decay Data”. *Nucl Data Sheets* 112 (2011).

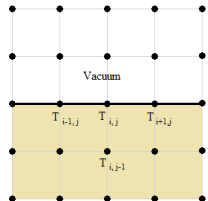
- [33] Gary W. Phillips et al. “Neutron Spectrometry Using CR-39 Track Etch Detectors”. *Radiation Protection Dosimetry* 120 (1-4 2006), pp. 457–460.
- [34] A. Parravicini M. Caresana M. Ferrarini and A. Sashala Naik. “Dose Measurements with CR-39 detectors at the CERF Reference Facility at CERN”. *Radiat Meas* 71 (2014), pp. 502–504.
- [35] M. Fuerstner M. Caresana M. Ferrarini and S. Mayer. “Determination of LET in PADC detectors through the measurement of track parameters”. *Nucl Instrum Meth A* 683 (2012), pp. 8–15.
- [36] Alvin Sashala Naik. “Neutron Dosimetry and Spectrometry in Complex Radiation Fields using CR-39 Track Detectors”. PhD thesis. Politecnico di Milano, 2016.
- [37] J. Blachot. “Nuclear Data Sheets for A=115”. *Nucl Data Sheets* 113 (2012), pp. 2391–2535.
- [38] F. Schmittroth, D. L. Smith, and S. Chiba. *Report ANL/NDM-115*. (1990). Data extracted from the ENDF database, version VI (April 2016).
- [39] Cezar Ciprian Negoita. “Measurement of Neutron Flux Spectra in a Tungsten Benchmark by Neutron Foil Activation Method”. PhD thesis. zur Erlangung des akademischen Grades, 1973.
- [40] Richard P. Baum. *Therapeutic Nuclear Medicine*. Springer, 2014.
- [41] K. Ashkan J. S. Dooley M. L. Schilsky A. Ala A. P. Walker. “Wilson’s Disease”. *Lancet* 369 (2007), pp. 397–408.
- [42] Syed M. Qaim. “Nuclear Data for Medical Radionuclide Production: Present Status and Future Needs”. *Nuclear Data Needs and Capabilities for Applications Proceedings*. 2015.
- [43] R. Bass et al. “Disintegration of K39 by Fast Neutrons”. *Nucl Phys* 28 (1961), pp. 479–493.
- [44] Bethany L. Goldblum Eric F. Matthews Brian J. Quiter. “Fission Induced Electromagnetic Response”. *Nuclear Data Needs and Capabilities for Applications Proceedings*. 2015.
- [45] Robert C. Baumann. “Radiation-induced Soft Errors in Advanced Semiconductor Technologies”. *IEEE* 5 (2005), pp. 305–316.

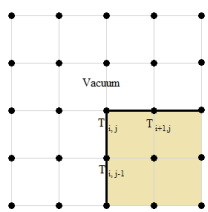
Appendix A

Finite Difference Equations

All equations are for the condition where $\Delta X = \Delta Y$. Subcooled boiling equations are used when the wall heat flux is in the nucleate boiling range ($q''_{ONB} < q''_{wall} < q''_{crit}$). For subcooled boiling equations, C is determined using equation (3.18)

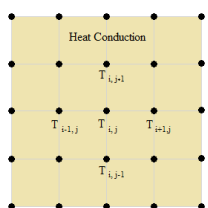
Adiabatic Boundary



$$T_{i,j} = \frac{T_{i-1,j} + T_{i+1,j} + 2T_{i,j-1}}{4} \quad (\text{A.1})$$


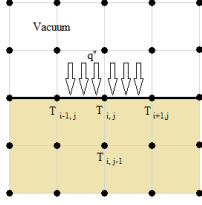
$$T_{i,j} = \frac{T_{i+1,j} + T_{i,j-1}}{2} \quad (\text{A.2})$$

Conduction



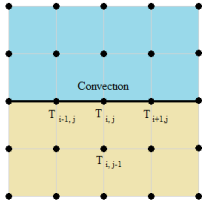
$$T_{i,j} = \frac{T_{i+1,j} + T_{i-1,j} + T_{i,j+1} + T_{i,j-1}}{4} \quad (\text{A.3})$$

Surface Heat Flux



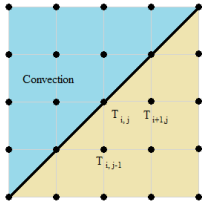
$$T_{i,j} = \frac{(T_{i-1,j} + T_{i+1,j})}{4} + \frac{T_{i,j-1}}{2} + \frac{\Delta X q''}{2k} \quad (\text{A.4})$$

Convection



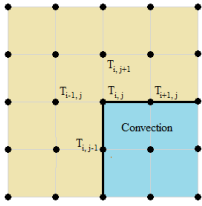
$$\text{Single Phase } T_{i,j} = \frac{T_{i-1,j} + T_{i+1,j} + 2T_{i-1,j} + \frac{2h_{le}\Delta X T_l}{k}}{2\left(\frac{h_{le}\Delta X}{k} + 2\right)} \quad (\text{A.5})$$

$$\text{Subcooled Boiling } T_{i,j} = \frac{T_{i-1,j} + T_{i+1,j} + 2T_{i-1,j} + \frac{2\Delta X}{k}\left(h_{le}T_l - C(T_{i,j} - T_{sat})^{1/r}\right)}{2\left(\frac{h_{le}\Delta X}{k} + 2\right)} \quad (\text{A.6})$$



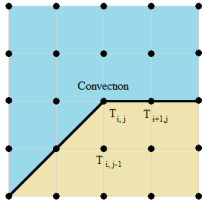
$$\text{Single Phase } T_{i,j} = \frac{T_{i+1,j} + T_{i,j-1} + \frac{\sqrt{2}\Delta X h_{le} T_l}{k}}{\left(\frac{\sqrt{2}h_{le}\Delta X}{k} + 2\right)} \quad (\text{A.7})$$

$$\text{Subcooled Boiling } T_{i,j} = \frac{T_{i+1,j} + T_{i,j-1} + \frac{\sqrt{2}\Delta X}{k}\left(h_{le}T_l - C(T_{i,j} - T_{sat})^{1/r}\right)}{\left(\frac{\sqrt{2}h_{le}\Delta X}{k} + 2\right)} \quad (\text{A.8})$$



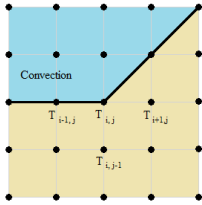
$$\text{Single Phase } T_{i,j} = \frac{T_{i-1,j} + T_{i+1,j} + T_{i,j-1} + T_{i,j+1} + \frac{\Delta X h_{le} T_l}{k}}{\left(\frac{h_{le}\Delta X}{k} + 3\right)} \quad (\text{A.9})$$

$$\text{Subcooled Boiling } T_{i,j} = \frac{T_{i-1,j} + T_{i+1,j} + T_{i,j-1} + T_{i,j+1} + \frac{\Delta X}{k}\left(h_{le}T_l - C(T_{i,j} - T_{sat})^{1/r}\right)}{\left(\frac{h_{le}\Delta X}{k} + 3\right)} \quad (\text{A.10})$$



$$\text{Single Phase } T_{i,j} = \frac{T_{i+1,j} + T_{i,j-1} + \frac{(\sqrt{2}+1)\Delta X h_{le} T_l}{k}}{\left(\frac{(\sqrt{2}+1)h_{le}\Delta X}{k} + 3\right)} \quad (\text{A.11})$$

$$\text{Subcooled Boiling } T_{i,j} = \frac{2T_{i+1,j} + T_{i,j-1} + \frac{(\sqrt{2}+1)\Delta X}{k}\left(h_{le}T_l - C(T_{i,j} - T_{sat})^{1/r}\right)}{\left(\frac{(\sqrt{2}+1)h_{le}\Delta X}{k} + 3\right)} \quad (\text{A.12})$$



$$\text{Single Phase } T_{i,j} = \frac{2T_{i+1,j} + 2T_{i,j-1} + T_{i-1,j} + \frac{(\sqrt{2}+1)\Delta X h_{le} T_l}{k}}{\left(\frac{(\sqrt{2}+1)h_{le}\Delta X}{k} + 5\right)} \quad (\text{A.13})$$

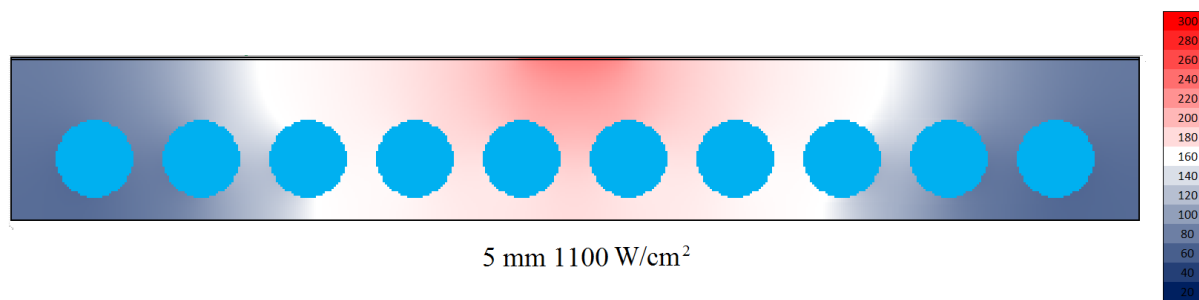
$$\text{Subcooled Boiling } T_{i,j} = \frac{2T_{i+1,j} + 2T_{i,j-1} + T_{i-1,j} + \frac{(\sqrt{2}+1)\Delta X}{k}\left(h_{le}T_l - C(T_{i,j} - T_{sat})^{1/r}\right)}{\left(\frac{(\sqrt{2}+1)h_{le}\Delta X}{k} + 5\right)} \quad (\text{A.14})$$

Appendix B

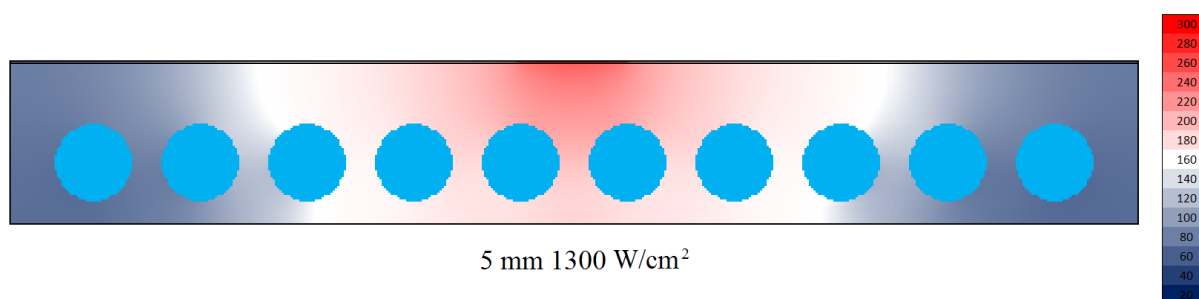
Temperature Maps

Select 2D temperature maps for 5 mm to 20 mm diameter uniform flux deuteron beam profiles given the water flow rates and properties shown in Fig. 3.5 are shown in Fig. B.0. The selected temperature maps have maximum surface temperatures of approximately 300°C or less. It can be seen that the temperature isotherm of 160°C is practically in the same location for all scenarios.

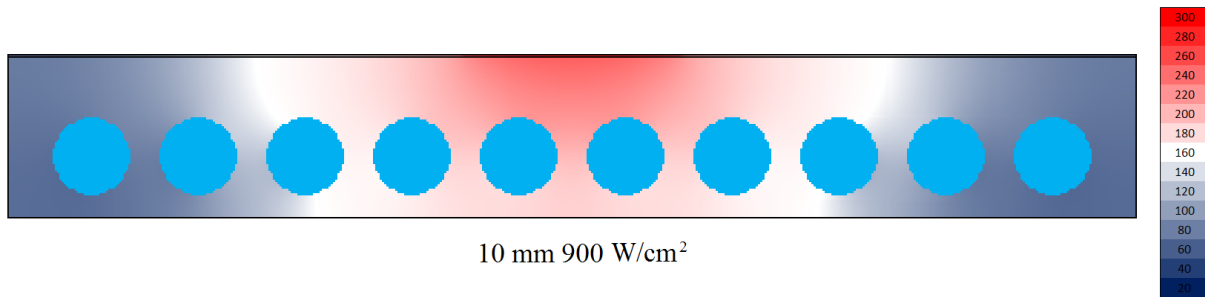
Following the temperature maps are graphs showing the temperature across the titanium surface for various uniform beam fluxes with beam diameters of 15 mm to 20 mm.



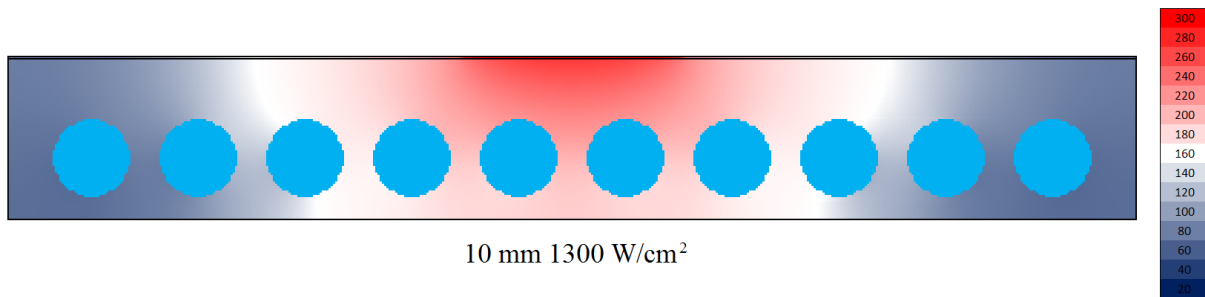
(a)



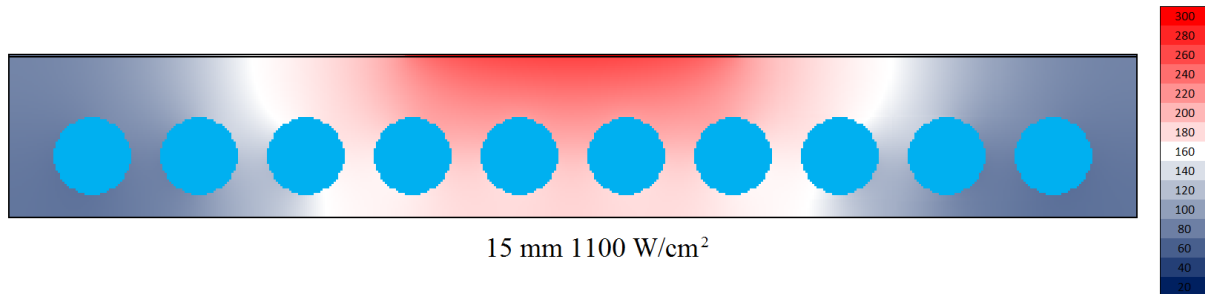
(b)



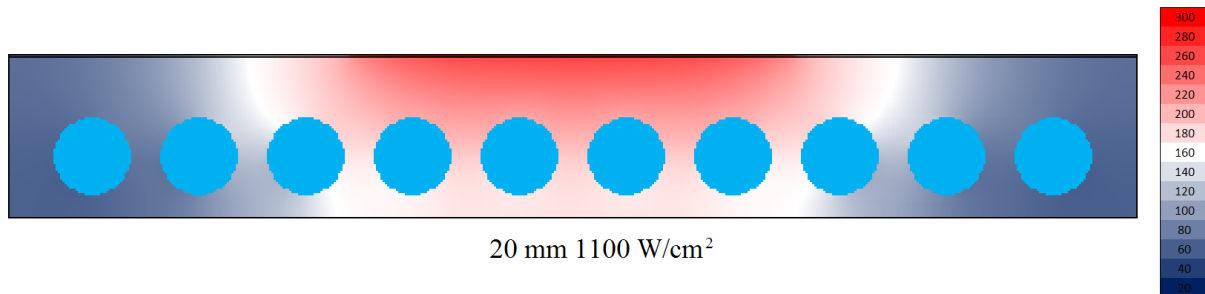
(c)



(d)

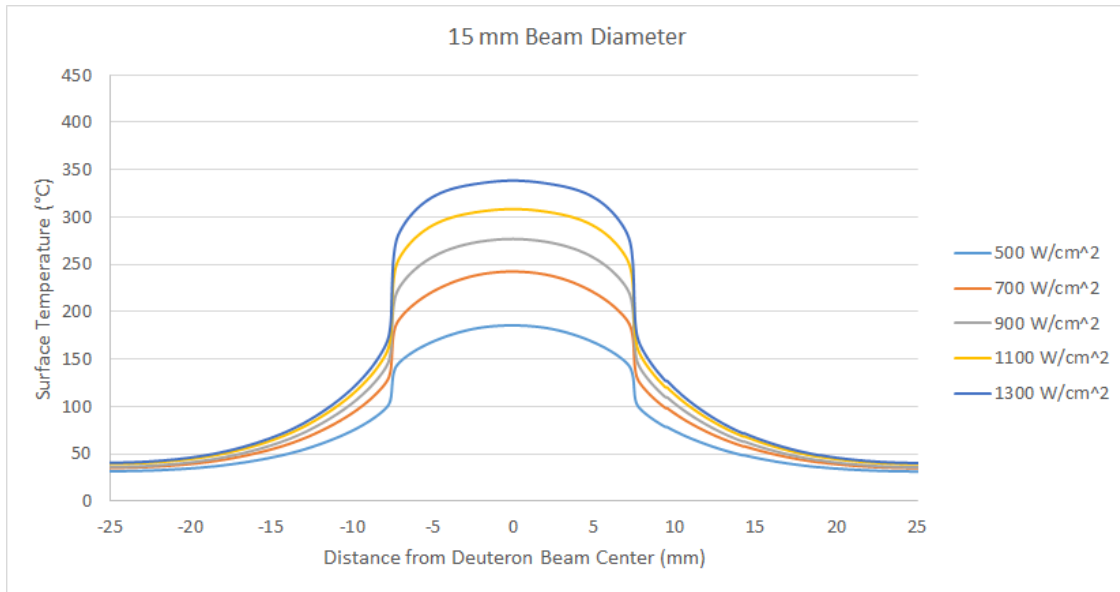


(e)

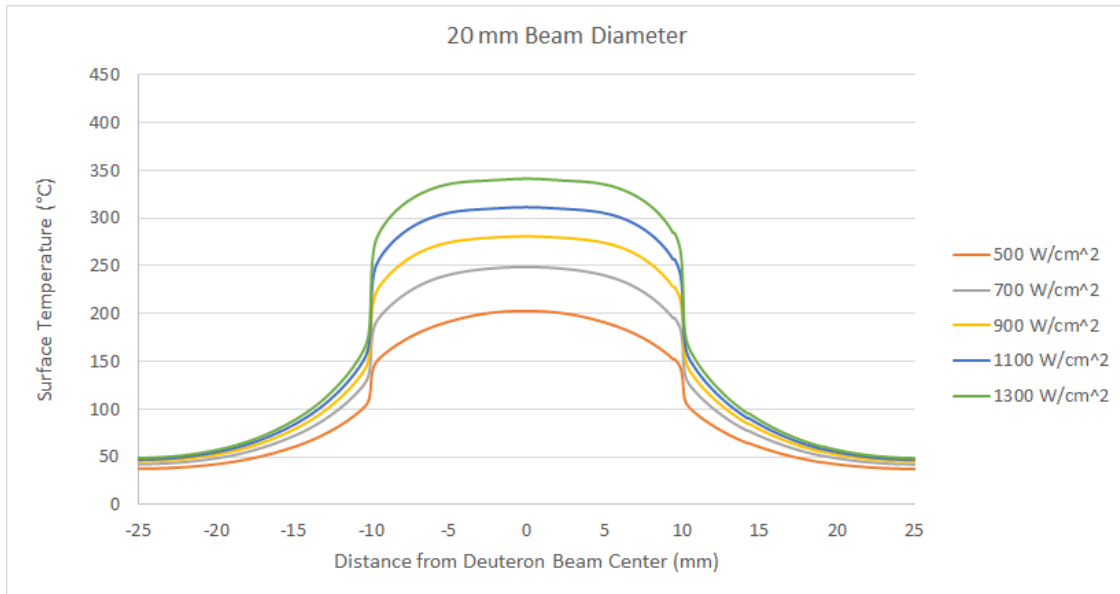


(f)

Figure B.0: Target temperature maps for uniform beam flux with beam diameters of (a and b) 5 mm, (c and d) 10 mm, (e) 15 mm, and (f) 20 mm.



(a)



(b)

Figure B.1: Target surface temperatures for uniform beam heat flux for (a) 5 mm, (b) 10 mm, (c) 15 mm, and (d) 20 mm ion beam diameters.

Appendix C

Neutron Flux and Energy Distribution Codes

C.1 Matlab Flux Code

The Matlab neutron flux distribution code provided requires two inputs. The first input is data from a CR-39 neutron exposure. This is a spreadsheet that contains a matrix of count values divided into small bins that are 0.510 mm by 0.68 mm in size across the detector surface. Other sizes are available for input if the `x_det` and `y_det` variables are altered to the correct size. The second input contains the beam current density at the target determined by a Comsol simulation. This spreadsheet is formatted into three columns, X distance (mm), Y distance (mm), and current density (mA/cm²). Both inputs are quite large, so they are not included in this appendix.

The supplied code is also indented to fit on a standard 8.5 in by 11 in page. All outputs are for a 2 cm x 3 cm rectangular surface centered and parallel to the beam center of the target surface at a user given distance. The outputs include 3D surface plots of the target current density and the CR-39 detector counts, and 2D contour plots of the maximum neutron energy and flux distributions. Output tabulated data includes the total flux by energy intervals (n/s), total flux per cell (n/cm²/s), and total counts per cell based on a given irradiation time.

```
%Start of Code%
```

```
%Open CR39 File
```

```
directory = 'C:\Users\Desktop\CR39 Matlab\'; %Input directory location
filename = cat(2,directory,'3611.xlsx'); %input filename
detector = xlsread(filename);
distance = 8.38; %distance between target and CR39, mm
irradiation_time = 45; %sec
```

```

%Plot CR39 Detector
x_length = size(detector,2);
y_length = size(detector,1);
x_det = -0.255*(x_length-1):0.255*2:0.255*(x_length-1);
y_det = -0.340*(y_length-1):0.340*2:0.340*(y_length-1);
x_det_length = size(x_det,2);
y_det_length = size(y_det,2);
[X_det,Y_det] = meshgrid(x_det,y_det);
figure('name','CR39 Detector Counts - Filtered');
filteredImg = filterImg(detector);
CR39_Plot_Filt = surf(x_det,y_det,filteredImg);
xlabel('X (mm)');
ylabel('Y (mm)');
zlabel('Counts (#/cell)');
daspect([1 1 5]);

%Open Comsol File
directory2 = 'C:\Users\Desktop\CR39 Matlab\'; %Input directory location
filename2 = cat(2,directory2,'100 kV.xlsx'); %input filename
comsol = xlsread(filename2);
x_width = 0.255*2; %mm
y_height = 0.340*2; %mm
cell_area = x_width*y_height; %mm^2
cell_area2 = cell_area*0.01; %cm^2

%Plot Comsol Target Simulation
x_com = comsol(:,1)'.*25.4;
y_com = comsol(:,2)'.*25.4;
z_com = comsol(:,3)';
x_com_length = size(x_com,2);
y_com_length = size(y_com,2);
x_grid = x_det;
y_grid = y_det;
[X,Y] = meshgrid(x_grid,y_grid);
com_grid = griddata(x_com,y_com,z_com,X,Y); %mA/cm^2
com_grid2 = com_grid*cell_area2*6.2422E15; %#/s
com_grid3 = com_grid2;
com_grid(isnan(com_grid)) = 0;
com_grid2(isnan(com_grid2)) = 0;
com_grid3(com_grid3<1E13)=0;
com_grid3(com_grid3>1E13)=1;
com_grid3(isnan(com_grid3)) = 0;

```



```

figure('name','Comsol Current Density Target');
Comsol_Current_Density = surf(X,Y,com_grid);
xlabel('X (mm)');
ylabel('Y (mm)');
zlabel('Current Density (mA/cm^2)');
daspect([1 1 5]);

%Solid Angles Between Detectors, Omega (Sr)
centers_x_det = X_det;
centers_y_det = Y_det;
centers_x_com = x_det;
centers_y_com = y_det;
x_distance = [];
y_distance = [];

for j = 1:y_det_length
    for i = 1:x_det_length
        x_distance = X_det - x_det(i);
        y_distance = Y_det - y_det(j);
        omega = zeros(y_length,x_length);
        for l = 1:y_det_length
            for k = 1:x_det_length
                if x_distance(1,k) == 0 && y_distance(1,k) == 0;
                    omega(1,k) = 4*acos(sqrt((1 + (x_width/(2*distance))^2
                        +(y_height/(2*distance))^2)./((1+(x_width/
                            (2*distance))^2)*(1+(y_height/(2*distance))^2))));
                elseif x_distance(1,k)-x_width/2 > 0 && y_distance(1,k)== 0
                    omega(1,k) = (4*acos(sqrt((1 + (2*(x_distance(1,k)
                        +x_width/2)/(2*distance))^2+(2*(y_distance(1,k)
                        + y_height/2)/(2*distance))^2)./((1+(2*(x_distance(1,k)
                        +x_width/2)/(2*distance))^2)*(1+(2*(y_distance(1,k)
                        +y_height/2)/(2*distance))^2))))-4*acos(sqrt((1
                        +(2*(x_distance(1,k)-x_width/2)/(2*distance))^2
                        +(2*(y_distance(1,k)+y_height/2)/(2*distance))^2)./((1
                        +(2*(x_distance(1,k)-x_width/2)/(2*distance))^2)*(1
                        +(2*(y_distance(1,k)+y_height/2)/(2*distance))^2))))))/2;
                elseif x_distance(1,k)-x_width/2 < 0 && y_distance(1,k)== 0
                    omega(1,k) = (4*acos(sqrt((1 +(2*(x_distance(1,k)
                        -x_width/2)/(2*distance))^2+(2*(y_distance(1,k)
                        +y_height/2)/(2*distance))^2)./((1+(2*(x_distance(1,k)
                        -x_width/2)/(2*distance))^2)*(1+(2*(y_distance(1,k)
                        +y_height/2)/(2*distance))^2))))-4*acos(sqrt((1

```

```

+(2*(x_distance(1,k)+x_width/2)/(2*distance))^2
+(2*(y_distance(1,k)+y_height/2)/(2*distance))^2./((1
+(2*(x_distance(1,k)+x_width/2)/(2*distance))^2*(1
+(2*(y_distance(1,k)+y_height/2)/(2*distance))^2))))/2;
elseif y_distance(1,k)-y_height/2 > 0 && x_distance(1,k)== 0
omega(1,k) = (4*acos(sqrt((1 + (2*(x_distance(1,k)
+x_width/2)/(2*distance))^2+(2*(y_distance(1,k)
+y_height/2)/(2*distance))^2)./(1+(2*(x_distance(1,k)
+x_width/2)/(2*distance))^2*(1+(2*(y_distance(1,k)
+y_height/2)/(2*distance))^2))))-4*acos(sqrt((1
+(2*(x_distance(1,k)+x_width/2)/(2*distance))^2
+(2*(y_distance(1,k)-y_height/2)/(2*distance))^2)./(1
+(2*(x_distance(1,k)+x_width/2)/(2*distance))^2*(1+
(2*(y_distance(1,k)-y_height/2)/(2*distance))^2)))))/2;
elseif y_distance(1,k)-y_height/2 < 0 && x_distance(1,k)== 0
omega(1,k) = (4*acos(sqrt((1 + (2*(x_distance(1,k)+x_width/2)/
(2*distance))^2+(2*(y_distance(1,k)-y_height/2)/
(2*distance))^2)./(1+(2*(x_distance(1,k)+x_width/2)/
(2*distance))^2*(1+(2*(y_distance(1,k)-y_height/2)/
(2*distance))^2))))-4*acos(sqrt((1 + (2*(x_distance(1,k)+
x_width/2)/(2*distance))^2+(2*(y_distance(1,k)+y_height/2)/
(2*distance))^2)./(1+(2*(x_distance(1,k)+x_width/2)/
(2*distance))^2*(1+(2*(y_distance(1,k)+y_height/2)/
(2*distance))^2)))))/2;
elseif x_distance(1,k)-x_width/2 > 0 && y_distance(1,k)
-y_height/2 > 0
omega(1,k) = (4*acos(sqrt((1 +(2*(x_distance(1,k)+x_width/2)/
(2*distance))^2+(2*(y_distance(1,k)+y_height/2)/
(2*distance))^2)./(1+(2*(x_distance(1,k)+x_width/2)/
(2*distance))^2*(1+(2*(y_distance(1,k)+y_height/2)/
(2*distance))^2))))-4*acos(sqrt((1 + (2*(x_distance(1,k)
-x_width/2)/(2*distance))^2+(2*(y_distance(1,k)+y_height/2)/
(2*distance))^2)./(1+(2*(x_distance(1,k)-x_width/2)/
(2*distance))^2*(1+(2*(y_distance(1,k)+y_height/2)/
(2*distance))^2))))-4*acos(sqrt((1 + (2*(x_distance(1,k)
+x_width/2)/(2*distance))^2+(2*(y_distance(1,k)-y_height/2)/
(2*distance))^2)./(1+(2*(x_distance(1,k)+x_width/2)/
(2*distance))^2*(1+(2*(y_distance(1,k)-y_height/2)/
(2*distance))^2))))+4*acos(sqrt((1 + (2*(x_distance(1,k)
-x_width/2)/(2*distance))^2+(2*(y_distance(1,k)-y_height/2)/
(2*distance))^2)./(1+(2*(x_distance(1,k)-x_width/2)/
(2*distance))^2*(1+(2*(y_distance(1,k)-y_height/2)/

```

```

(2*distance))^2))))/4;
elseif x_distance(1,k)-x_width/2 < 0 && y_distance(1,k)
-y_height/2 < 0
omega(1,k) = (4*acos(sqrt((1 + (2*(x_distance(1,k)-x_width/2)/
(2*distance))^2+(2*(y_distance(1,k)-y_height/2)/
(2*distance))^2)./(1+(2*(x_distance(1,k)-x_width/2)/
(2*distance))^2*(1+(2*(y_distance(1,k)-y_height/2)/
(2*distance))^2))))-4*acos(sqrt((1 + (2*(x_distance(1,k)
+x_width/2)/(2*distance))^2+(2*(y_distance(1,k)-y_height/2)/
(2*distance))^2)./(1+(2*(x_distance(1,k)+x_width/2)/
(2*distance))^2*(1+(2*(y_distance(1,k)-y_height/2)/
(2*distance))^2))))-4*acos(sqrt((1 + (2*(x_distance(1,k)
-x_width/2)/(2*distance))^2+(2*(y_distance(1,k)+y_height/2)/
(2*distance))^2)./(1+(2*(x_distance(1,k)-x_width/2)/
(2*distance))^2*(1+(2*(y_distance(1,k)+y_height/2)/
(2*distance))^2))))+4*acos(sqrt((1 + (2*(x_distance(1,k)
+x_width/2)/(2*distance))^2+(2*(y_distance(1,k)+y_height/2)/
(2*distance))^2)./(1+(2*(x_distance(1,k)+x_width/2)/
(2*distance))^2*(1+(2*(y_distance(1,k)+y_height/2)/
(2*distance))^2)))))/4;
elseif x_distance(1,k)-x_width/2 < 0 && y_distance(1,k)
-y_height/2 > 0
omega(1,k) = (4*acos(sqrt((1 + (2*(x_distance(1,k)-x_width/2)/
(2*distance))^2+(2*(y_distance(1,k)+y_height/2)/
(2*distance))^2)./(1+(2*(x_distance(1,k)-x_width/2)/
(2*distance))^2*(1+(2*(y_distance(1,k)+y_height/2)/
(2*distance))^2))))-4*acos(sqrt((1 + (2*(x_distance(1,k)
+x_width/2)/(2*distance))^2+(2*(y_distance(1,k)+y_height/2)/
(2*distance))^2)./(1+(2*(x_distance(1,k)+x_width/2)/
(2*distance))^2*(1+(2*(y_distance(1,k)+y_height/2)/
(2*distance))^2))))-4*acos(sqrt((1 + (2*(x_distance(1,k)
-x_width/2)/(2*distance))^2+(2*(y_distance(1,k)-y_height/2)/
(2*distance))^2)./(1+(2*(x_distance(1,k)-x_width/2)/
(2*distance))^2*(1+(2*(y_distance(1,k)-y_height/2)/
(2*distance))^2))))+4*acos(sqrt((1 + (2*(x_distance(1,k)
+x_width/2)/(2*distance))^2+(2*(y_distance(1,k)-y_height/2)/
(2*distance))^2)./(1+(2*(x_distance(1,k)+x_width/2)/
(2*distance))^2*(1+(2*(y_distance(1,k)-y_height/2)/
(2*distance))^2)))))/4;
elseif x_distance(1,k)-x_width/2 > 0 && y_distance(1,k)
-y_height/2 < 0
omega(1,k) = (4*acos(sqrt((1 + (2*(x_distance(1,k)+x_width/2)/

```

```

(2*distance))^2+(2*(y_distance(1,k)-y_height/2)/
(2*distance))^2)./((1+(2*(x_distance(1,k)+x_width/2)/
(2*distance))^2*(1+(2*(y_distance(1,k)-y_height/2)/
(2*distance))^2))))-4*acos(sqrt((1 + (2*(x_distance(1,k)
-x_width/2)/(2*distance))^2+(2*(y_distance(1,k)-y_height/2)/
(2*distance))^2)./((1+(2*(x_distance(1,k)-x_width/2)/
(2*distance))^2*(1+(2*(y_distance(1,k)-y_height/2)/
(2*distance))^2))))-4*acos(sqrt((1 + (2*(x_distance(1,k)
+x_width/2)/(2*distance))^2+(2*(y_distance(1,k)+y_height/2)/
(2*distance))^2)./((1+(2*(x_distance(1,k)+x_width/2)/
(2*distance))^2*(1+(2*(y_distance(1,k)+y_height/2)/
(2*distance))^2))))+4*acos(sqrt((1 + (2*(x_distance(1,k)
-x_width/2)/(2*distance))^2+(2*(y_distance(1,k)+y_height/2)/
(2*distance))^2)./((1+(2*(x_distance(1,k)-x_width/2)/
(2*distance))^2*(1+(2*(y_distance(1,k)+y_height/2)/
(2*distance))^2))))))/4;
end
end
end

omega_cell{j,i} = omega;

end
end

for i = 1:x_det_length
  for j = 1:y_det_length
    theta = (atan(sqrt((X_det-x_det(i)).^2+(Y_det-y_det(j)).^2)./
distance))*180/pi;

%Differential Cross Sections (m^2/sr)
dcs_20{j,i} = (6.3460E-15.*theta.^6 - 3.1465E-12.*theta.^5
+ 4.4224E-10.*theta.^4 + 4.0203E-10.*theta.^3
- 2.8397E-06.*theta.^2 + 5.4324E-06.*theta
+ 2.6563E-02)*1e-31./cos(theta*pi/180);
dcs_30{j,i} = (3.2362E-14.*theta.^6 - 1.5402E-11.*theta.^5
+ 1.8767E-09.*theta.^4 + 7.8871E-08.*theta.^3
- 2.0174E-05.*theta.^2 + 8.0430E-05.*theta
+ 1.3401E-01)*1e-31./cos(theta*pi/180);
dcs_40{j,i} = (8.2997E-14.*theta.^6 - 3.8977E-11.*theta.^5
+ 4.3754E-09.*theta.^4 + 3.0833E-07.*theta.^3
- 5.9983E-05.*theta.^2 + 2.1863E-04.*theta

```

```

    + 3.3760E-01)*1e-31./cos(theta*pi/180);
dcs_50{j,i} = (1.3584E-13.*theta.^6 - 6.0816E-11.*theta.^5
    + 5.4842E-09.*theta.^4 + 8.3000E-07.*theta.^3
    - 1.2101E-04.*theta.^2 + 5.0626E-04.*theta
    + 5.7203E-01)*1e-31./cos(theta*pi/180);
dcs_60{j,i} = (2.2884E-13.*theta.^6 - 1.0177E-10.*theta.^5
    + 9.2796E-09.*theta.^4 + 1.3174E-06.*theta.^3
    - 1.9369E-04.*theta.^2 + 7.2096E-04.*theta
    + 8.6648E-01)*1e-31./cos(theta*pi/180);
dcs_70{j,i} = (3.5804E-13.*theta.^6 - 1.6219E-10.*theta.^5
    + 1.6805E-08.*theta.^4 + 1.5034E-06.*theta.^3
    - 2.5555E-04.*theta.^2 + 5.1811E-04.*theta
    + 1.1856)*1e-31./cos(theta*pi/180);
dcs_80{j,i} = (3.4373E-13.*theta.^6 - 1.3820E-10.*theta.^5
    + 5.4122E-09.*theta.^4 + 3.6803E-06.*theta.^3
    - 4.1195E-04.*theta.^2 + 1.6193E-03.*theta
    + 1.5186)*1e-31./cos(theta*pi/180);
dcs_90{j,i} = (3.9220E-13.*theta.^6 - 1.4786E-10.*theta.^5
    + 2.7902E-10.*theta.^4 + 5.3953E-06.*theta.^3
    - 5.5592E-04.*theta.^2 + 2.2710E-03.*theta
    + 1.8847)*1e-31./cos(theta*pi/180);
dcs_100{j,i}= (4.4884E-13.*theta.^6 - 1.6129E-10.*theta.^5
    - 4.8836E-09.*theta.^4 + 7.3057E-06.*theta.^3
    - 7.2333E-04.*theta.^2 + 3.3748E-03.*theta
    + 2.2827)*1e-31./cos(theta*pi/180);

    Max_Energy{j,i} = (2.48874 + 0.30083.*(cosd(theta))
    + 0.01368.*(cosd(theta)).^2);
end
end

%Max Energy
for i = 1:x_det_length
    for j = 1:y_det_length
        Max_Energy2{j,i} = Max_Energy{j,i}.*com_grid3(j,i);
    end
end

Max_Energy4 = zeros(y_length,x_length);

for i = 1:x_det_length
    for j = 1:y_det_length

```

```

    for k = 1:x_det_length
        for l = 1:y_det_length
            Max_Energy3=Max_Energy2{j,i};
            if Max_Energy3(1,k)> Max_Energy4(1,k);
                Max_Energy4(1,k) = Max_Energy3(1,k);
            end
        end
    end
end
end
end

end

end

end

%Cross Section = differential cross section * solid angle (m^2)
cs_20 = gmultiply(dcs_20,omega_cell);
cs_30 = gmultiply(dcs_30,omega_cell);
cs_40 = gmultiply(dcs_40,omega_cell);
cs_50 = gmultiply(dcs_50,omega_cell);
cs_60 = gmultiply(dcs_60,omega_cell);
cs_70 = gmultiply(dcs_70,omega_cell);
cs_80 = gmultiply(dcs_80,omega_cell);
cs_90 = gmultiply(dcs_90,omega_cell);
cs_100= gmultiply(dcs_100,omega_cell);

%Target Layer Depths for [0-25keV, 35-45keV... 95-100keV];
target_depth=[0.3229,0.0782,0.0699,0.0646,0.0607,0.0577,
              0.0553,0.0534,0.0687]; %um
target_depth = target_depth.*1E-6; %m

%Reaction Rate = Current*N*cs*Depth
%N*Depth (#/m^2)
N_depth = target_depth.*5.6681E28;
%N*cs*Depth (#)
N_CS_Depth_20 = cellfun(@(x) x*N_depth(1),cs_20,'un',0);
N_CS_Depth_30 = cellfun(@(x) x*N_depth(2),cs_30,'un',0);
N_CS_Depth_40 = cellfun(@(x) x*N_depth(3),cs_40,'un',0);
N_CS_Depth_50 = cellfun(@(x) x*N_depth(4),cs_50,'un',0);
N_CS_Depth_60 = cellfun(@(x) x*N_depth(5),cs_60,'un',0);
N_CS_Depth_70 = cellfun(@(x) x*N_depth(6),cs_70,'un',0);
N_CS_Depth_80 = cellfun(@(x) x*N_depth(7),cs_80,'un',0);
N_CS_Depth_90 = cellfun(@(x) x*N_depth(8),cs_90,'un',0);
N_CS_Depth_100 = cellfun(@(x) x*N_depth(9),cs_100,'un',0);

R_20_Sum = zeros(y_length,x_length);

```

```

R_30_Sum = zeros(y_length,x_length);
R_40_Sum = zeros(y_length,x_length);
R_50_Sum = zeros(y_length,x_length);
R_60_Sum = zeros(y_length,x_length);
R_70_Sum = zeros(y_length,x_length);
R_80_Sum = zeros(y_length,x_length);
R_90_Sum = zeros(y_length,x_length);
R_100_Sum = zeros(y_length,x_length);

for i = 1:x_det_length
    for j = 1:y_det_length
        %Reactions per cell
        R_20{j,i} = N_CS_Depth_20{j,i}.*com_grid2(j,i).*1.35;
        R_30{j,i} = N_CS_Depth_30{j,i}.*com_grid2(j,i).*1.35;
        R_40{j,i} = N_CS_Depth_40{j,i}.*com_grid2(j,i).*1.15;
        R_50{j,i} = N_CS_Depth_50{j,i}.*com_grid2(j,i).*1.15;
        R_60{j,i} = N_CS_Depth_60{j,i}.*com_grid2(j,i).*0.75;
        R_70{j,i} = N_CS_Depth_70{j,i}.*com_grid2(j,i).*0.75;
        R_80{j,i} = N_CS_Depth_80{j,i}.*com_grid2(j,i).*0.75;
        R_90{j,i} = N_CS_Depth_90{j,i}.*com_grid2(j,i).*0.75;
        R_100{j,i}= N_CS_Depth_100{j,i}.*com_grid2(j,i).*0.75;

        R_20_Sum = R_20_Sum + R_20{j,i};
        R_30_Sum = R_30_Sum + R_30{j,i};
        R_40_Sum = R_40_Sum + R_40{j,i};
        R_50_Sum = R_50_Sum + R_50{j,i};
        R_60_Sum = R_60_Sum + R_60{j,i};
        R_70_Sum = R_70_Sum + R_70{j,i};
        R_80_Sum = R_80_Sum + R_80{j,i};
        R_90_Sum = R_90_Sum + R_90{j,i};
        R_100_Sum = R_100_Sum + R_100{j,i};
    end
end

%Total Flux per cell (#/s)
Total_Flux = R_20_Sum + R_30_Sum + R_40_Sum + R_50_Sum
    + R_60_Sum + R_70_Sum + R_80_Sum + R_90_Sum +R_100_Sum;

%Total Flux per Cell (#/cm^2/s)
Total_Flux_cm = Total_Flux/cell_area2;

%Counts per Cell (#/cell)

```

```

Counts = Total_Flux*irradiation_time;

figure('name','100keV Flux');
contourf(x_det,y_det,Total_Flux_cm);
colorbar
axis equal
hcb=colorbar;
title(hcb,'#/cm^2/s')
xlabel('Y (mm)');
ylabel('X (mm)');

figure('name','Max Neutron Energy');
contourf(x_det,y_det,Max_Energy4);
colorbar
hcb=colorbar;
title(hcb,'MeV')
axis equal
xlabel('Y (mm)');
ylabel('X (mm)');

%End of Code%

```

C.2 MCNP Flux Code

The following MCNP code calculates the flux in the target slot assuming a uniform beam of a given diameter. Using MCNP, attenuation of the target can be taken into account.

```

Title - Etcheverry HFNG Irradiation
C -----
C Cells
C -----
10 500 -1.00      60 -70 91 -92 93 -94      imp:n,p=1 $ CR-39 Target
C 20 200 -7.134   70 -75 -80      imp:n,p=1 $
50 300 -8.92     5 -10 20 -30 40 -50 100 101 102 103
                104 115 116 117 118 119      imp:n,p=1 $ Cu Front
60 300 -8.92     5 -10 20 -30 85 -90 105 106 107 108 109
                110 111 112 113 114      imp:n,p=1 $ Cu Back
62 300 -8.92     20 -54 -51 50 5 -10      imp:n,p=1 $ Cu lip lower left
63 300 -8.92     -30 55 -51 50 5 -10      imp:n,p=1 $ Cu lip lower right
64 300 -8.92     20 -54 52 -85 5 -10      imp:n,p=1 $ Cu lip lower left
65 300 -8.92     -30 55 52 -85 5 -10      imp:n,p=1 $ Cu lip lower left

```



```

70 400 -1.00    -100 5 -10                                imp:n,p=1 $ water channel
71 400 -1.00    -101 5 -10                                imp:n,p=1 $ water channel
72 400 -1.00    -102 5 -10                                imp:n,p=1 $ water channel
73 400 -1.00    -103 5 -10                                imp:n,p=1 $ water channel
74 400 -1.00    -104 5 -10                                imp:n,p=1 $ water channel
75 400 -1.00         -105 5 -10                            imp:n,p=1 $ water channel
76 400 -1.00         -106 5 -10                            imp:n,p=1 $ water channel
77 400 -1.00         -107 5 -10                            imp:n,p=1 $ water channel
78 400 -1.00         -108 5 -10                            imp:n,p=1 $ water channel
79 400 -1.00         -109 5 -10                            imp:n,p=1 $ water channel
80 400 -1.00         -110 5 -10                            imp:n,p=1 $ water channel
81 400 -1.00         -111 5 -10                            imp:n,p=1 $ water channel
82 400 -1.00         -112 5 -10                            imp:n,p=1 $ water channel
83 400 -1.00         -113 5 -10                            imp:n,p=1 $ water channel
84 400 -1.00         -114 5 -10                            imp:n,p=1 $ water channel
85 400 -1.00    -115 5 -10                                imp:n,p=1 $ water channel
86 400 -1.00    -116 5 -10                                imp:n,p=1 $ water channel
87 400 -1.00    -117 5 -10                                imp:n,p=1 $ water channel
88 400 -1.00    -118 5 -10                                imp:n,p=1 $ water channel
89 400 -1.00    -119 5 -10                                imp:n,p=1 $ water channel
C 100 500 -0.92    50 -85 5 -10 20 -30 -91 92 -93 94
                                                    imp:n,p=1 $ poly holder
550 0  -200 ((120 128 -130 131):(128 130 132):(128 -131 140)
          :(136 130 -128 129):(126 -129 -130 131):(134 130 -129)
          :(142 -129 -131):(138 -131 129 -128):(-124 129 -128)
          :(122 129 -128))
600 0  (-121 128 -130 131):(128 130 -133):(128 -131 -141)
          :(-137 130 -128 129):(-127 -129 -130 131):(-135 130 -129)
          :(-143 -129 -131):(-139 -131 129 -128)
650 0  (131 -130 125 -123 -128 129) (10: -5: -40: 90: -20: 30)
          :(-144 123 -122):(-144 -125 124)
675 0  (5 -10 40 -90 20 -30)
          ((-85 50 54 -55):(20 -54 51 -52):(55 -30 51 -52))
          #10
700 600 -2.7 (-120 121 128 -130 131) : (-122 123 -128 129 -130 131 144)
          : (124 -125 -128 129 -130 131 144)
          : (-126 127 -129 -130 131) : (-132 133 130 128)
          : (-134 135 -129 130) : (-136 137 130 -128 129)
          : (-140 141 -131 128) : (-142 143 -131 -129)
          : (-138 139 -131 -128 129)
999 0 200

```

```

C -----
C Surfaces
C -----
C -----
5  px -4.66
10 px 4.66 $ 9.32 cm total - 4.66 cm
20 py -4.445 $ 8.89 cm total - 4.445 cm
30 py 4.445
40 pz -0.6858
50 pz 0.
51 pz 0.10795 $ create 1/8" slot
52 pz 0.42545 $ create 1/8" slot
54 py -2.445 $ left interior of lip should be 2.08 cm
55 py 2.445 $ right interior of lip
60 pz 0.1522 $ front surface of CR-39
70 pz 0.3302 $ back surface of CR-39
C 75 pz 0.23375
80 cz 0.5
85 pz 0.5334 $Top Cu lower
90 pz 1.2192 $Top Cu upper
91 py -1.0
92 py 1.0
93 px -1.5
94 px 1.5
100 c/x 0.2413 -0.254 0.1778
101 c/x 0.7413 -0.254 0.1778
102 c/x 1.2239 -0.254 0.1778
103 c/x 1.7065 -0.254 0.1778
104 c/x 2.1891 -0.254 0.1778
C
105 c/x 0.2413 0.7874 0.1778
106 c/x 0.7413 0.7874 0.1778
107 c/x 1.2239 0.7874 0.1778
108 c/x 1.7065 0.7874 0.1778
109 c/x 2.1891 0.7874 0.1778
C
110 c/x -0.2413 0.7874 0.1778
111 c/x -0.7413 0.7874 0.1778
112 c/x -1.2239 0.7874 0.1778
113 c/x -1.7065 0.7874 0.1778
114 c/x -2.1891 0.7874 0.1778
C

```

115 c/x -0.2413 -0.254 0.1778

116 c/x -0.7413 -0.254 0.1778

117 c/x -1.2239 -0.254 0.1778

118 c/x -1.7065 -0.254 0.1778

119 c/x -2.1891 -0.254 0.1778

C ----- SHROUD SURFACES -----

C PLATES WITH CYLINDRICAL CAPS ON TOP, BOTTOM, AND SIDES

C -----

120 C/Y 6.79 0. 3.24

121 C/Y 6.79 0. 2.98

122 PZ 3.23999

123 PZ 2.97999

124 PZ -3.23999

125 PZ -2.97999

126 C/Y -6.79 0. 3.24

127 C/Y -6.79 0. 2.98

128 PX 6.78999

129 PX -6.78999

130 PY 6.78999

131 PY -6.78999

132 S 6.79 6.79 0. 3.24

133 S 6.79 6.79 0. 2.98

134 S -6.79 6.79 0. 3.24

135 S -6.79 6.79 0. 2.98

136 C/X 6.79 0. 3.24

137 C/X 6.79 0. 2.98

138 C/X -6.79 0. 3.24

139 C/X -6.79 0. 2.98

140 S 6.79 -6.79 0. 3.24

141 S 6.79 -6.79 0. 2.98

142 S -6.79 -6.79 0. 3.24

143 S -6.79 -6.79 0. 2.98

144 CZ 2.032

C 145 CY 0.15875 \$ hole in extraction plate

C

200 sph 0. 0. 0. 30.0

C -----

C Data

C -----

C -----

C Materials for Geometry-----

```

C -----
M100 49000      1.0
M200 30000      1.0
M300 29063.70c  0.6915
      29065.70c  0.3085
M400 1001 0.67
      8016 0.33
M500 1001 .5
      6012 .5
M600 13027 1.0
F34:n 10
*F44:n 10
F21:n 200
F22:n 200
C21 -0.9 -0.8 -0.7 -0.6 -0.5 -0.4 -0.3 -0.2 -0.1 &
      0.  0.1 0.2 0.3 0.4 0.5 0.6 0.7 0.8 0.9 1.
FT21 FRV 0. 0. 1.
*F31:n 200
*F32:n 200
F41:n 200
FMESH04:n geom=xyz origin=-1.75 -1.75 0.1522
          imesh=1.75 jmesh=1.75 kmesh=0.1572
          iints=70 jints=70 kints=1
FMESH14:n geom=xyz origin=-1.75 -1.75 0.1522
          imesh=1.75 jmesh=1.75 kmesh=0.1572 emesh=3.
          iints=70 jints=70 kints=1 eints=100
C
C *FMESH14:n geom=xyz origin=0. 0. 0. axs = 0 0 1 vec = 1 0 0
C          imesh=0.5 jmesh=0.025 kmesh=1 emesh=5. eints=50
C          iints=10 jints=1 kints=1
C
C
C tmesh
C cmesh01:n flux
C cora01:n 0. 0.25 0.5
C corb01:n 0. 0.025
C corc01:n 360.
C endmd
C #####
C Source - 0.25 cm radius disk sources located
C          outside the copper target holder
C

```

```

SDEF POS=0. 0. -0.686 AXS=0 0 1 VEC=0 0 1 RAD=D3 PAR=N DIR=D4 &
      ERG=fdir D5 WGT=1.0 EXT=0
C SI1 L 0 -1.1 0. 0 1.1 0.
C SP1 0.5 0.5
C Distribution for axs
C SIn L 0 1 0 0 -1 0
C SPn 0.5 0.5
C Distribution for vec
C DS2 L 0 0 1
C Distribution for rad
SI3 0 0.25
SP3 -21 1.0
C Distribution for dir
C This is cos(theta) in one-degree increments from 180 to 0 degrees
C
SI4  -1      -0.99985      -0.99939      -0.99863      -0.99756 &
-0.99619      -0.99452      -0.99255      -0.99027      -0.98769 &
-0.98481      -0.98163      -0.97815      -0.97437      -0.9703 &
-0.96593      -0.96126      -0.9563      -0.95106      -0.94552 &
-0.93969      -0.93358      -0.92718      -0.9205      -0.91355 &
-0.90631      -0.89879      -0.89101      -0.88295      -0.87462 &
-0.86603      -0.85717      -0.84805      -0.83867      -0.82904 &
-0.81915      -0.80902      -0.79864      -0.78801      -0.77715 &
-0.76604      -0.75471      -0.74314      -0.73135      -0.71934 &
-0.70711      -0.69466      -0.682      -0.66913      -0.65606 &
-0.64279      -0.62932      -0.61566      -0.60182      -0.58779 &
-0.57358      -0.55919      -0.54464      -0.52992      -0.51504 &
-0.5      -0.48481      -0.46947      -0.45399      -0.43837 &
-0.42262      -0.40674      -0.39073      -0.37461      -0.35837 &
-0.34202      -0.32557      -0.30902      -0.29237      -0.27564 &
-0.25882      -0.24192      -0.22495      -0.20791      -0.19081 &
-0.17365      -0.15643      -0.13917      -0.12187      -0.10453 &
-0.087156      -0.069756      -0.052336      -0.034899      -0.017452 &
6.1232e-17      0.017452      0.034899      0.052336      0.069756 &
0.087156      0.10453      0.12187      0.13917      0.15643 &
0.17365      0.19081      0.20791      0.22495      0.24192 &
0.25882      0.27564      0.29237      0.30902      0.32557 &
0.34202      0.35837      0.37461      0.39073      0.40674 &
0.42262      0.43837      0.45399      0.46947      0.48481 &
0.5      0.51504      0.52992      0.54464      0.55919 &
0.57358      0.58779      0.60182      0.61566      0.62932 &
0.64279      0.65606      0.66913      0.682      0.69466 &

```

0.70711	0.71934	0.73135	0.74314	0.75471 &
0.76604	0.77715	0.78801	0.79864	0.80902 &
0.81915	0.82904	0.83867	0.84805	0.85717 &
0.86603	0.87462	0.88295	0.89101	0.89879 &
0.90631	0.91355	0.9205	0.92718	0.93358 &
0.93969	0.94552	0.95106	0.9563	0.96126 &
0.96593	0.9703	0.97437	0.97815	0.98163 &
0.98481	0.98769	0.99027	0.99255	0.99452 &
0.99619	0.99756	0.99863	0.99939	0.99985 &

1.0

```

C -----
C Secondary neutron angular distribution for 100keV incident deuterons
C (dsigma/domega)(theta)*domega normalized
C - from the Handbook of Fast Neutron Generators, Csikai
C I computed the normalized CDF and differenced it
C -----

```

```

SP4 0. 9.8082e-05 0.00029415 0.00048993 0.00068524 &
0.00087988 0.0010737 0.0012664 0.0014579 0.0016481 &
0.0018366 0.0020234 0.0022082 0.0023909 0.0025713 &
0.0027493 0.0029247 0.0030974 0.0032672 0.0034339 &
0.0035974 0.0037576 0.0039144 0.0040676 0.0042172 &
0.004363 0.0045049 0.0046428 0.0047767 0.0049065 &
0.0050321 0.0051534 0.0052704 0.0053831 0.0054913 &
0.0055952 0.0056946 0.0057896 0.0058801 0.0059662 &
0.0060478 0.0061251 0.006198 0.0062665 0.0063308 &
0.0063908 0.0064467 0.0064985 0.0065462 0.0065901 &
0.0066301 0.0066663 0.0066699 0.0067281 0.0067538 &
0.0067763 0.0067956 0.0068119 0.0068254 0.0068361 &
0.0068443 0.00685 0.0068534 0.0068548 0.0068542 &
0.0068517 0.0068477 0.0068421 0.0068353 0.0068273 &
0.0068183 0.0068085 0.006798 0.006787 0.0067756 &
0.006764 0.0067524 0.0067409 0.0067296 0.0067186 &
0.0067082 0.0066983 0.0066893 0.006681 0.0066738 &
0.0066676 0.0066626 0.0066588 0.0066564 0.0066554 &
0.0066558 0.0066577 0.0066613 0.0066664 0.0066732 &
0.0066816 0.0066916 0.0067034 0.0067167 0.0067317 &
0.0067483 0.0067664 0.006786 0.0068071 0.0068295 &
0.0068531 0.006878 0.0069039 0.0069307 0.0069584 &
0.0069868 0.0070157 0.007045 0.0070746 0.0071042 &
0.0071336 0.0071627 0.0071913 0.0072192 0.0072461 &
0.0072719 0.0072963 0.007319 0.00734 0.0073588 &
0.0073752 0.0073891 0.0074002 0.0074082 0.0074128 &

```

0.0074139 0.0074112 0.0074044 0.0073932 0.0073776 &
 0.0073571 0.0073317 0.007301 0.0072649 0.0072231 &
 0.0071755 0.0071219 0.0070621 0.006996 0.0069233 &
 0.006844 0.006758 0.0066651 0.0065653 0.0064585 &
 0.0063446 0.0062236 0.0060954 0.0059602 0.0058179 &
 0.0056685 0.005512 0.0053487 0.0051785 0.0050017 &
 0.0048182 0.0046283 0.0044322 0.00423 0.0040219 &
 0.0038083 0.0035892 0.0033651 0.0031361 0.0029026 &
 0.0026648 0.0024232 0.0021779 0.0019294 0.0016781 &
 0.0014242 0.0011682 0.00091045 0.00065131 0.00039118 &
 0.00013046

C -----
 C Neutron energy vs angle interpolated from Csikai for 100keV
 C thick target
 C -----

DS5 2.1806 2.1806 2.1808 2.181 2.1813 &
 2.1816 2.1821 2.1826 2.1833 2.184 &
 2.1847 2.1856 2.1866 2.1876 2.1887 &
 2.1899 2.1912 2.1926 2.194 2.1955 &
 2.1971 2.1988 2.2006 2.2024 2.2043 &
 2.2063 2.2084 2.2106 2.2128 2.2151 &
 2.2175 2.2199 2.2225 2.2251 2.2277 &
 2.2305 2.2333 2.2362 2.2392 2.2422 &
 2.2453 2.2485 2.2517 2.255 2.2584 &
 2.2619 2.2654 2.2689 2.2726 2.2763 &
 2.28 2.2838 2.2877 2.2917 2.2956 &
 2.2997 2.3038 2.308 2.3122 2.3164 &
 2.3207 2.3251 2.3295 2.334 2.3385 &
 2.343 2.3476 2.3523 2.357 2.3617 &
 2.3665 2.3712 2.3761 2.381 2.3859 &
 2.3908 2.3958 2.4008 2.4058 2.4108 &
 2.4159 2.421 2.4261 2.4313 2.4364 &
 2.4416 2.4468 2.452 2.4573 2.4625 &
 2.4677 2.473 2.4783 2.4835 2.4888 &
 2.4941 2.4993 2.5046 2.5099 2.5151 &
 2.5204 2.5256 2.5309 2.5361 2.5413 &
 2.5465 2.5517 2.5569 2.562 2.5671 &
 2.5722 2.5773 2.5824 2.5874 2.5924 &
 2.5973 2.6022 2.6071 2.612 2.6168 &
 2.6216 2.6263 2.631 2.6356 2.6402 &
 2.6448 2.6493 2.6537 2.6581 2.6625 &
 2.6668 2.671 2.6752 2.6793 2.6833 &

2.6873 2.6912 2.6951 2.6989 2.7026 &
2.7062 2.7098 2.7133 2.7167 2.7201 &
2.7233 2.7265 2.7297 2.7327 2.7357 &
2.7385 2.7413 2.744 2.7466 2.7492 &
2.7516 2.754 2.7562 2.7584 2.7605 &
2.7625 2.7644 2.7662 2.7679 2.7696 &
2.7711 2.7725 2.7738 2.7751 2.7762 &
2.7773 2.7782 2.7791 2.7798 2.7805 &
2.781 2.7815 2.7818 2.7821 2.7822 &
2.7822

C

C FCL:n 1 1 0 24i 0

NPS 1e9

C CUT:n j 2.0

MODE n p

C PTRAC file=asc write=all event=src

C VOID

PRINT

Appendix D

CR39 and Predicted Neutron Flux Outputs

Below are outputs given for the HFNG flux calculator provided in Appendix C.

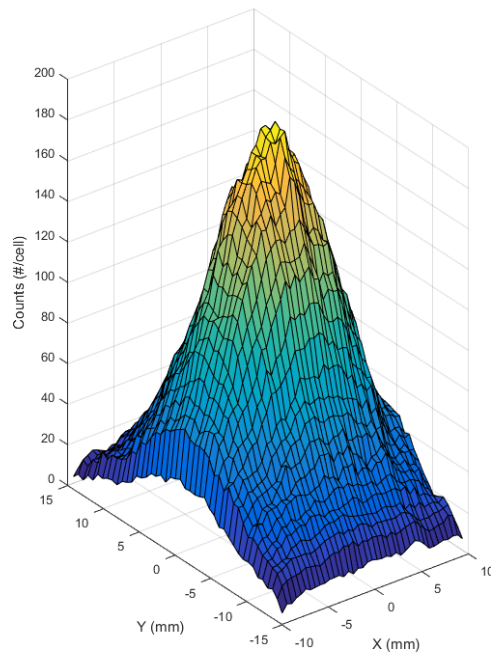


Figure D.1: Smoothed interpolated CR-39 detector count distribution

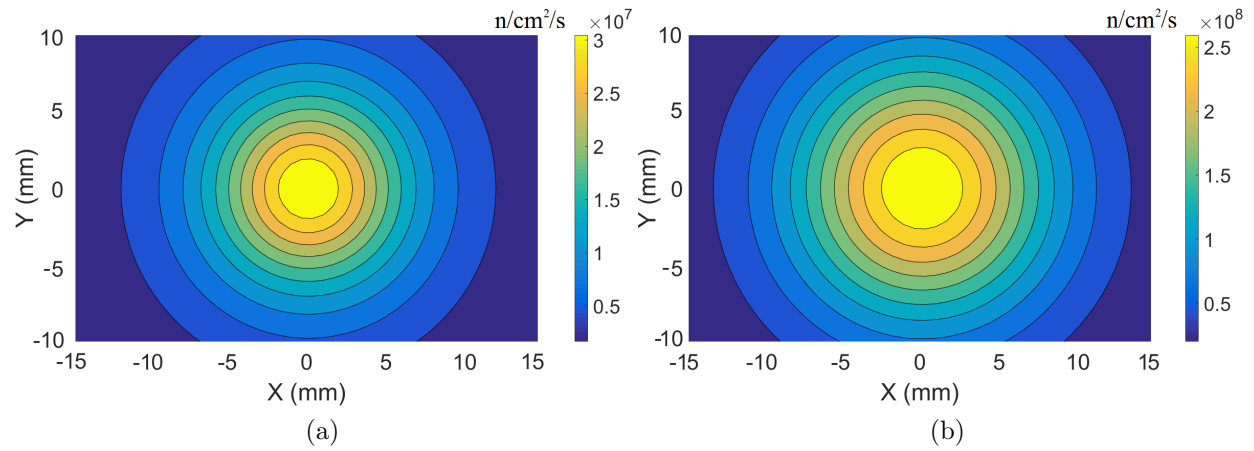


Figure D.2: (a) 100 kV, 1.43 mA and (b) 125 kV, 10 mA predicted flux maps in HFNG target slot

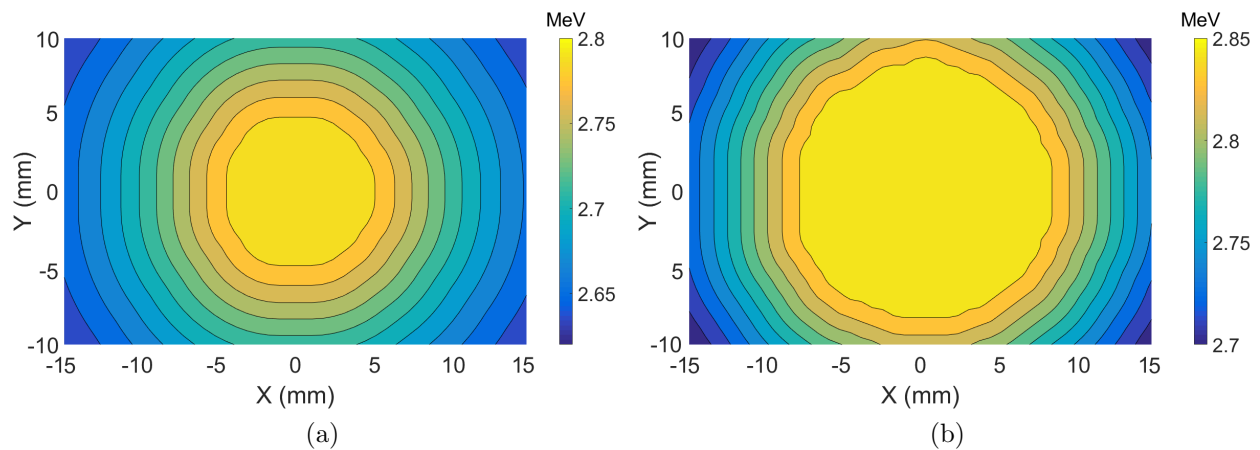


Figure D.3: Neutron energy spread in target sample slot for deuterium beams of (a) 100 keV, 1.43 mA and (b) 125 keV, 10 mA

Altering the code for 1.43 mA, 100 kV and 10 mA, 125 kV beams gives the following flux and maximum energy maps. Maps do not include target attenuation.

Appendix E

Indium Foil Experimental Data

Table E.1 displays the indium properties and gamma counting results using a high purity germanium detector. Other important experimental and counting characteristics are:

Irradiation start time = 0 s

Irradiation end time = 13216 s

336 keV Branching ratio = 45.8%

Detector absolute efficiency at 336 keV = 0.971%

MCNP energy distribution results for each foil are shown in Tables E.2 - E.10. Cross sections are determined by a polynomial fit to the experimental data shown in Fig. 5.9.

Table E.1: Indium Foil Properties

Foil Location	Foil Mass (g)	Count Start Time (s)	Count End Time (s)	Number of Counts in 336 keV Peak	Flux from Equation 5.5 ($\cdot 10^6$ n/cm ² /s)
1	0.1572	26394	28015	1890	4.57
2	0.1795	24788	26349	2318	4.70
3	0.1417	31875	33975	876	2.40
4	0.1154	34041	36477	2857	8.40
5	0.1175	39117	41937	3499.5	10.4
6	0.1417	23294	24735	1274.5	3.39
7	0.1571	29870	31791	2024.5	4.79
8	0.1235	36537	39057	1602	4.90
9	0.1227	28092	29833	696.5	2.24

Table E.2: Indium Foil Location 1 Properties

Energy Range (keV)	Fraction of Neutrons in Range [F_i]	Cross Section [σ_i] (mb)	$F_i \cdot \sigma_i$ (mb)
0-0.5	0.0400	0	0
0.5-0.7	0.0168	9.2	0.155
0.7-0.9	0.0131	34.6	0.455
0.9-1.1	0.0165	67.9	1.12
1.1-1.3	0.0169	106.7	1.81
1.3-1.5	0.0119	148.4	1.77
1.5-1.7	0.0122	190.0	2.34
1.7-1.9	0.0092	231.9	2.14
1.9-2.1	0.0073	269.6	1.98
2.1-2.3	0.0070	302.1	2.12
2.3-2.5	0.0289	327.7	9.48
2.5-2.7	0.7672	345.0	264.6
2.7-2.9	0.0525	352.4	18.51
			$\sum F_i \sigma_i = 306.5$

Table E.3: Indium Foil Location 2 Properties

Energy Range (keV)	Fraction of Neutrons in Range [F_i]	Cross Section [σ_i] (mb)	$F_i \cdot \sigma_i$ (mb)
0-0.5	0.0371	0	0
0.5-0.7	0.0157	9.2	0.144
0.7-0.9	0.0121	34.6	0.420
0.9-1.1	0.0152	67.9	1.03
1.1-1.3	0.0158	106.7	1.69
1.3-1.5	0.0112	148.4	1.67
1.5-1.7	0.0116	190.0	2.21
1.7-1.9	0.0088	231.9	2.05
1.9-2.1	0.0073	269.6	1.95
2.1-2.3	0.0068	302.1	2.07
2.3-2.5	0.0266	327.7	8.71
2.5-2.7	0.7061	345.0	243.6
2.7-2.9	0.1255	352.4	44.23
			$\sum F_i \sigma_i = 309.8$

Table E.4: Indium Foil Location 3 Properties

Energy Range (keV)	Fraction of Neutrons in Range [F_i]	Cross Section [σ_i] (mb)	$F_i \cdot \sigma_i$ (mb)
0-0.5	0.0530	0	0
0.5-0.7	0.0201	9.2	0.184
0.7-0.9	0.0166	34.6	0.576
0.9-1.1	0.0212	67.9	1.44
1.1-1.3	0.0207	106.7	2.21
1.3-1.5	0.0149	148.4	2.21
1.5-1.7	0.0151	190.0	2.88
1.7-1.9	0.0113	231.9	2.62
1.9-2.1	0.0091	269.6	2.45
2.1-2.3	0.0088	302.1	2.67
2.3-2.5	0.0409	327.7	13.4
2.5-2.7	0.7627	345.0	263.1
2.7-2.9	0.0054	352.4	1.91
			$\sum F_i \sigma_i = 295.7$

Table E.5: Indium Foil Location 4 Properties

Energy Range (keV)	Fraction of Neutrons in Range [F_i]	Cross Section [σ_i] (mb)	$F_i \cdot \sigma_i$ (mb)
0-0.5	0.0267	0	0
0.5-0.7	0.0126	9.2	0.116
0.7-0.9	0.0094	34.6	0.324
0.9-1.1	0.0112	67.9	0.762
1.1-1.3	0.0121	106.7	1.30
1.3-1.5	0.0088	148.4	1.31
1.5-1.7	0.0087	190.0	1.66
1.7-1.9	0.0070	231.9	1.61
1.9-2.1	0.0056	269.6	1.50
2.1-2.3	0.0049	302.1	1.47
2.3-2.5	0.0177	327.7	5.81
2.5-2.7	0.2211	345.0	76.3
2.7-2.9	0.6549	352.4	230.6
			$\sum F_i \sigma_i = 322.7$

Table E.6: Indium Foil Location 5 Properties

Energy Range (keV)	Fraction of Neutrons in Range [F_i]	Cross Section [σ_i] (mb)	$F_i \cdot \sigma_i$ (mb)
0-0.5	0.0228	0	0
0.5-0.7	0.0112	9.2	0.103
0.7-0.9	0.0082	34.6	0.285
0.9-1.1	0.0098	67.9	0.667
1.1-1.3	0.0108	106.7	1.15
1.3-1.5	0.0081	148.4	1.20
1.5-1.7	0.0079	190.0	1.51
1.7-1.9	0.0066	231.9	1.52
1.9-2.1	0.0053	269.6	1.44
2.1-2.3	0.0046	302.1	1.39
2.3-2.5	0.0154	327.7	5.03
2.5-2.7	0.0641	345.0	22.1
2.7-2.9	0.8252	352.4	290.8
			$\sum F_i \sigma_i = 327.3$

Table E.7: Indium Foil Location 6 Properties

Energy Range (keV)	Fraction of Neutrons in Range [F_i]	Cross Section [σ_i] (mb)	$F_i \cdot \sigma_i$ (mb)
0-0.5	0.0441	0	0
0.5-0.7	0.0179	9.2	0.165
0.7-0.9	0.0142	34.6	0.492
0.9-1.1	0.0179	67.9	1.21
1.1-1.3	0.0181	106.7	1.93
1.3-1.5	0.0129	148.4	1.92
1.5-1.7	0.0131	190.0	2.50
1.7-1.9	0.0099	231.9	2.29
1.9-2.1	0.0079	269.6	2.14
2.1-2.3	0.0077	302.1	2.31
2.3-2.5	0.0323	327.7	10.6
2.5-2.7	0.7923	345.0	273.3
2.7-2.9	0.0118	352.4	4.15
			$\sum F_i \sigma_i = 303.0$

Table E.8: Indium Foil Location 7 Properties

Energy Range (keV)	Fraction of Neutrons in Range [F_i]	Cross Section [σ_i] (mb)	$F_i \cdot \sigma_i$ (mb)
0-0.5	0.0380	0	0
0.5-0.7	0.0161	9.2	0.148
0.7-0.9	0.0126	34.6	0.435
0.9-1.1	0.0157	67.9	1.06
1.1-1.3	0.0162	106.7	1.73
1.3-1.5	0.0115	148.4	1.71
1.5-1.7	0.0117	190.0	2.23
1.7-1.9	0.0089	231.9	2.07
1.9-2.1	0.0071	269.6	1.92
2.1-2.3	0.0067	302.1	2.02
2.3-2.5	0.0270	327.7	8.86
2.5-2.7	0.7234	345.0	249.5
2.7-2.9	0.1051	352.4	37.1
			$\sum F_i \sigma_i = 308.8$

Table E.9: Indium Foil Location 8 Properties

Energy Range (keV)	Fraction of Neutrons in Range [F_i]	Cross Section [σ_i] (mb)	$F_i \cdot \sigma_i$ (mb)
0-0.5	0.0348	0	0
0.5-0.7	0.0150	9.2	0.138
0.7-0.9	0.0115	34.6	0.397
0.9-1.1	0.0142	67.9	0.968
1.1-1.3	0.0151	106.7	1.61
1.3-1.5	0.0107	148.4	1.59
1.5-1.7	0.0110	190.0	2.10
1.7-1.9	0.0085	231.9	1.97
1.9-2.1	0.0070	269.6	1.88
2.1-2.3	0.0065	302.1	1.97
2.3-2.5	0.0247	327.7	8.10
2.5-2.7	0.6252	345.0	215.7
2.7-2.9	0.2158	352.4	76.1
			$\sum F_i \sigma_i = 312.5$

Table E.10: Indium Foil Location 9 Properties

Energy Range (keV)	Fraction of Neutrons in Range [F_i]	Cross Section [σ_i] (mb)	$F_i \cdot \sigma_i$ (mb)
0-0.5	0.0515	0	0
0.5-0.7	0.0197	9.2	0.182
0.7-0.9	0.0161	34.6	0.557
0.9-1.1	0.0207	67.9	1.40
1.1-1.3	0.0204	106.7	2.18
1.3-1.5	0.0145	148.4	2.16
1.5-1.7	0.0149	190.0	2.84
1.7-1.9	0.0111	231.9	2.56
1.9-2.1	0.0088	269.6	2.38
2.1-2.3	0.0087	302.1	2.64
2.3-2.5	0.0394	327.7	12.93
2.5-2.7	0.7680	345.0	264.9
2.7-2.9	0.0059	352.4	2.09
			$\sum F_i \sigma_i = 296.9$